

PL-TR-97-2113

**AIRBORNE REMOTE SOUNDING OF CIRRUS CLOUD
PARAMETERS USING ARES CHANNEL DATA**

**S. C. Ou
K. N. Liou
P. Yang
P. Rolland**

**Center for Atmospheric and Remote Sounding Studies (CARSS)
Department of Meteorology
University of Utah
Salt Lake City, Utah 84112-0110**

30 June 1997

**Final Report
17 May 1996 - 17 May 1997**

19980227 047

Approved for public release; distribution unlimited

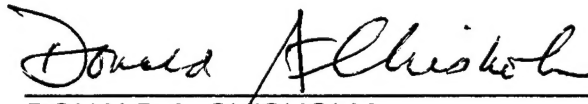


**PHILLIPS LABORATORY
DIRECTORATE OF GEOPHYSICS
AIR FORCE MATERIEL COMMAND
HANSCOM AFB, MA 01731-3010**

"This technical report has been reviewed and is approved for publication."



THOMAS R. CAUDILL
Contract Manager



DONALD A. CHISHOLM
Chief, Remote Sensing Applications Branch
Optical Effects Division



WILLIAM A. M. BLUMBERG, Director
Optical Effects Division

This report has been reviewed by the ESC Public Affairs Office (PA) and is releasable to the National Technical Information Service (NTIS).

Qualified requestors may obtain additional copies from the Defense Technical Information Center (DTIC). All others should apply to the National Technical Information Service (NTIS).

If your address has changed, or if you wish to be removed from the mailing list, or if the addressee is no longer employed by your organization, please notify PL/IM, 29 Randolph Road, Hanscom AFB, MA 01731-3010. This will assist us in maintaining a current mailing list.

Do not return copies of this report unless contractual obligations or notices on a specific document requires that it be returned.

REPORT DOCUMENTATION PAGE

Form Approved
OMB No. 0704-0188

Public reporting burden for this collection of information is estimated to average 1 hour per response, including the time for reviewing instructions, searching existing data sources, gathering and maintaining the data needed, and completing and reviewing the collection of information. Send comments regarding this burden estimate or any other aspect of this collection of information, including suggestions for reducing the burden, to Washington Headquarters Services, Directorate for Information Operations and Reports, 1215 Jefferson Davis Highway, Suite 1204, Arlington, VA 22202-4302, and to the Office of Management and Budget, Paperwork Reduction Project (0704-0188), Washington, DC 20503.

1. AGENCY USE ONLY (Leave blank)		2. REPORT DATE 30 June 1997		3. REPORT TYPE AND DATES COVERED Final Report, 17 May 1996 - 17 May 1997	
4. TITLE AND SUBTITLE Airborne Remote Sounding of Cirrus Cloud Parameters Using ARES Channel Data				5. FUNDING NUMBERS F19628-96-C-0052 PE 64441F PR SMCP TA 96 WU AA	
6. AUTHOR(S) S.C. Ou, K.N. Liou, P. Yang, and P. Rolland					
7. PERFORMING ORGANIZATION NAME(S) AND ADDRESS(ES) Center for Atmospheric and Remote Sounding Studies (CARSS) Department of Meteorology, University of Utah Salt Lake City, Utah 84112-0110				8. PERFORMING ORGANIZATION REPORT NUMBERS	
9. SPONSORING / MONITORING AGENCY NAME(S) AND ADDRESS(ES) Phillips Laboratory 29 Randolph Road Hanscom AFB, MA 01731-3010 Contract Manager: Tom Caudill/GP OR				10. SPONSORING / MONITORING AGENCY REPORT NUMBER PL-TR-97- 2113	
11. SUPPLEMENTARY NOTES					
12a. DISTRIBUTION / AVAILABILITY STATEMENT Approved for public release; distribution unlimited				12b. DISTRIBUTION CODE	
13 ABSTRACT (Maximum 200 words) Results of the phase functions, single-scattering albedos, and extinction coefficients for three representative cirrus cloud ice crystal size distributions are presented for the Airborne Remote Earth Sensing (ARES) System 2-6.4 μm wavelengths. The ice crystal sizes range from 5 to 800 μm with shapes spanning from bullet rosettes, hollow and solid columns, plates, to aggregates. The computations are carried out on the basis of a unified theory for light scattering by ice crystals recently developed by our research group. Effects of incorporating small ice crystals on the scattering and absorption calculations are assessed. An airborne retrieval algorithm to infer cirrus cloud temperature, optical depth and mean effective sizes is subsequently presented using the ARES 5.1-5.3 and 3.7 μm channels data. This scheme has been applied to the ARES data collected on September 16, 1995, over the Hanscom AFB area. Validation of the retrieved cloud temperature, optical depth, and mean effective size is carried out using the collocated and coincident ground-based 8.6-mm radar data and in-situ size distributions from the 2D probe on board HARP.					
14. SUBJECT TERMS cirrus cloud, light scattering and absorption, ARES, HARP, remote sensing, cloud temperatures, optical depth				15. NUMBER OF PAGES 70	
				16. PRICE CODE	
17. SECURITY CLASSIFICATION OF REPORT Unclassified	18. SECURITY CLASSIFICATION OF THIS PAGE Unclassified	19. SECURITY CLASSIFICATION OF ABSTRACT Unclassified	20. LIMITATION OF ABSTRACT Unlimited		

TABLE OF CONTENTS

	<u>Page</u>
1. INTRODUCTION AND BACKGROUND.....	1
2. LIGHT SCATTERING BY ICE CRYSTALS.....	2
2.1 Index of Refraction for Ice.....	2
2.2 Ice Crystal Size Distributions.....	4
2.3 Scattering and Absorption Properties of Ice Crystals.....	6
2.4 Effects of Small Ice Crystals on the Single-Scattering Properties.....	8
3. RETRIEVAL OF CIRRUS CLOUD PARAMETERS USING ARES CHANNEL DATA.....	30
3.1 Principle of Retrieving Cirrus Temperature, Emissivity, and Ice Crystal Size Using ARES Channels.....	33
3.2 Application of the Retrieval Scheme to ARES Data.....	37
3.2.1 ARES Channel Spectral Properties.....	37
3.2.2 Selection of Retrieval Channels.....	40
3.2.3 Determination of Mean Clear Radiances.....	47
3.2.4 Application of the Retrieval Scheme to ARES Channel Data.....	50
3.2.5 Validation of Retrieval Results.....	59
4. SUMMARY.....	63
REFERENCES.....	64

1. INTRODUCTION AND BACKGROUND

The Spaced Based Infrared Systems (SBIRS) Program is a multi-satellite constellation designed to conduct global and regional surveillance using passive infrared detection techniques. To facilitate the smooth operation of instruments on board satellites, the impacts of clouds as a clutter source and as obscurants must be quantified. One of the primary goals for the cloud related efforts is to assess the spatial variability of background radiances in spectral bands between 2 and 5 μm at geometries relevant to the SBIRS constellation. Clouds are important contributors to the overall background radiance structure, particularly in spectral bands with weighting functions in the troposphere and lower stratosphere. In particular, the high-altitude cirrus clouds often pose a serious problem in the satellite surveillance using the passive infrared detection technique. In this project, we have carried out a program designed to understand the effects of cirrus clouds between 2 and 5 μm on the upwelling radiances measured by infrared sensors on board satellites, and to develop a cirrus cloud remote sensing algorithm based on their physical properties within this spectral range for application to the development of infrared sensors.

The principal objectives of the present project are: (a) to compute the ice crystal phase function, single-scattering albedo, and extinction coefficient for the spectral range 2-6.4 μm using a unified theory for light scattering by ice crystals developed by our research group; (b) to collect and analyze available ice crystal size distributions to support the radiance measurements from satellite and aircraft; (c) to develop a remote sensing algorithm and computational code for the retrieval of cirrus temperature (height), optical depth, and ice crystal size based on the radiative properties of cirrus clouds; and (d) to collaborate with the SBIRS scientists to analyze the available aircraft and microphysic data. To meet the preceding research goals, we have acquired the radiance data collected by the 75-channel Airborne Remote Earth Sensing (ARES) System and the microphysical data collected by the cloud probes on board the High Altitude Reconnaissance Platform (HARP) during the Hanscom AFB mission flight on September 16, 1995.

This report is organized as follows. In Section 2, we discuss the range of ice crystal bounding

parameters, including the refractive indices for ice in the ARES spectral interval and the ice crystal size and shape for midlatitude cirrus cloud systems. Analyses of the available ice crystal size distribution measurements were made to obtain representative values for radiative transfer and remote sensing applications. Computational results for the extinction coefficient, single-scattering albedo, asymmetry factor, and phase function for the ARES 75-channel spectral wavelengths and for ice crystals of various sizes and shapes are also presented. Effects of incorporation of small ice crystals on scattering and absorption calculations are further investigated. Section 3 describes the development of a remote sensing algorithm for the retrieval of cirrus temperature (height), optical depth, and ice crystal size using the ARES 5.1-5.3 and 3.7 μm channels. Validation of the retrieval scheme is further made by using the ground-based 8.6-mm radar and aircraft 2D-C probe ice crystal data. Finally, summary is presented in Section 4.

2. LIGHT SCATTERING BY ICE CRYSTALS

2.1 Index of Refraction for Ice

For interpretation of the observed ARES bidirectional reflectances (BRDFs) and development of a remote sensing algorithm based on ARES channels to retrieve cirrus cloud temperature, optical depth, and ice crystal sizes, we must understand the spectral variation of the refractive indices for ice, the ice crystal size distribution, and the variability of ice crystal shape.

Figure 1 shows the real and imaginary refractive indices for ice and water from 2 to 6.5 μm (Liou 1992). The real part of the refractive index is a measure of the phase speed of the electromagnetic wave, while the imaginary component of the refractive index is related to the absorption coefficient. The drastic increase of the real part from about 2.9 to 3.2 μm for both ice and water is referred to as the anomalous dispersion. The imaginary part varies by about three orders of magnitude from 2 to 3.5 μm . For $\lambda > 3.5 \mu\text{m}$, the variation is smaller. Both water and ice show similar patterns of the spectral variation. To resolve the aforementioned spectral variation of the refractive indices of ice, we have selected the optimal number of wavelengths for light scattering calculations that are required for applications to the ARES channels. More wavelengths are chosen

Index of Refraction

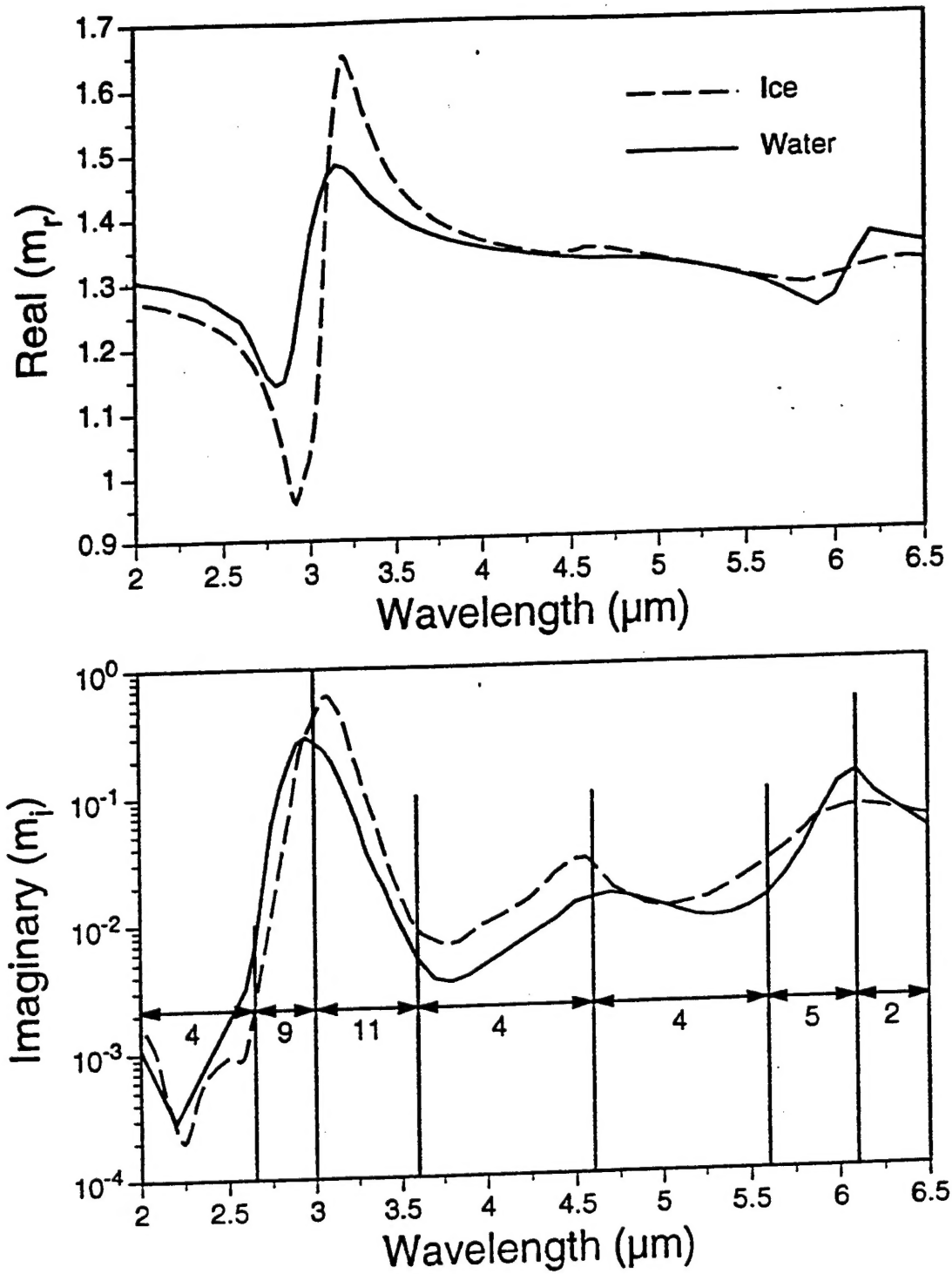


Figure 1 The real and imaginary refractive indices for ice and water from $\lambda=2$ to $\lambda=6.5 \mu\text{m}$ (Liou, 1992).

for the spectral region where the refractive index varies drastically. Appropriate interpolations can be performed to obtain the scattering and absorption values corresponding exactly to the ARES channel wavelengths.

2.2 Ice Crystal Size Distributions

The interpretation of radiometric measurements and the development of remote sensing algorithms for detecting ubiquitous cirrus clouds requires comprehensive knowledge of the two fundamental ice microphysics parameters: ice crystal size distribution and ice crystal shape. Both parameters vary significantly in space and in time and their variabilities are subject to a number of ice microphysical processes spanning from homogeneous and heterogeneous nucleations to diffusional growth, collision and coalescence, and gravitational settling processes. Because aircraft and sounding measurements are restricted in their spatial and temporal coverages, only limited databases are available. In the following, we present three representative ice crystal size distributions which are chosen from various ice crystal size distributions collected by replicators and cloud probes during a number of field experiments over midlatitude regions.

In conjunction with our radiative transfer and remote sensing studies involving cirrus clouds, we have analyzed 11 ice crystal size distributions from aircraft observations for use in the parameterization of their radiative properties (Fu and Liou 1993). We have also acquired aircraft optical probe data and balloon-borne replicator sonde data collected during FIRE-II-IFO, Kansas, 1991, and during April 1994 over the ARM-CART site. From these ice crystal size distributions, we have selected three representative cases: the balloon-sounding data collected during FIRE-II-IFO on December 5, 1991 and two ice crystal size distributions corresponding to the cold and warm cirrus clouds, as shown in Figure 2. The December 5 curve is the composite ice crystal size distribution obtained from averaging over the ice crystal size distributions at selected vertical levels normalized by the observed number density at each level (Ou et al. 1995). On that date, a layer of well-defined cirrus cloud was present over the observation site. Near the cloud top at 13 km, the cirrus cloud was composed of small ice particles with sizes between 5 and 100 μm . Note that the smallest ice crystals that

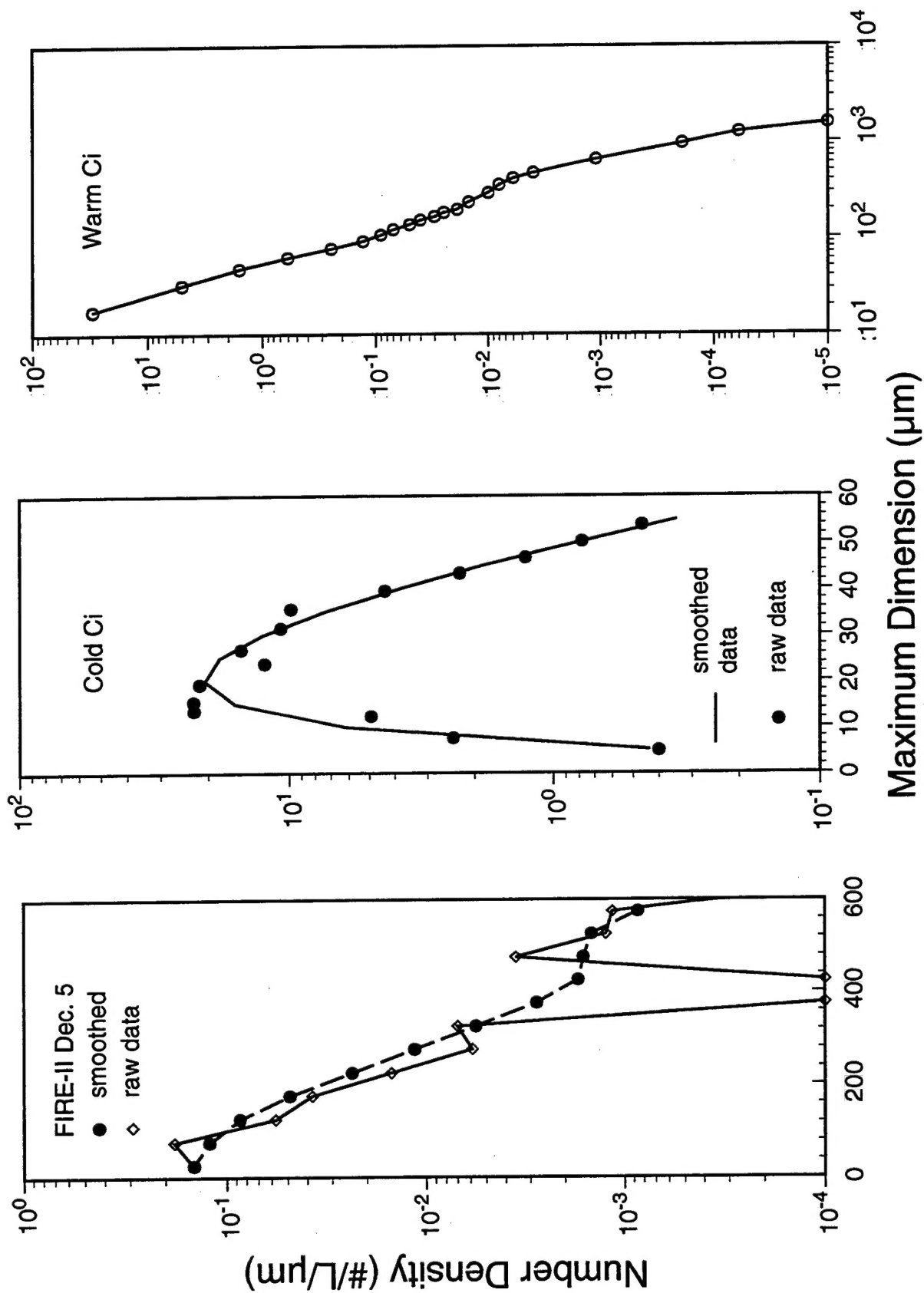


Figure 2 Three representative ice crystal size distributions for typical midlatitude cirrus cloud systems.

the replicator could resolve are on the order of 5 μm . In the middle part of the cloud between 10 and 12 km, ice crystals were columns, bullet rosettes, plates, and aggregates. The size distributions become broadened and show a bimodal shape toward the lower part of the cloud. Near the cloud base at 9.6 km, the size distribution is dominated by partially sublimated irregularly shaped ice crystals. The composite ice crystal size distribution spans from about 5 to 800 μm , which is the typical range of ice crystal size distributions observed in cirrus clouds. Because of the typical size range and the presence of the frequently observed ice crystal shapes, the December 5 case is selected as the representative ice crystal size distribution for midlatitudes.

The ice crystal distributions associated with cold cirrus were obtained from the FSSP measurements over the ARM-CART site at about 0236 UTC, April 19, 1994. The image of the collocated polarization lidar return signals (K. Sassen, private communication) indicated that a layer of cirrus cloud was located between 12 and 13.5 km. The University of North Dakota's Citation aircraft was flying at 13 km, where the measured temperature was -70°C . The cold cirrus size distribution extends from about 5 to 55 μm and fits well to a Gamma distribution. The ice crystal size distribution associated with warm cirrus clouds is taken from Heymsfield and Platt (1984) which was derived from the measurements of FSSP, 1D-C, and 1D-P probes with temperatures in the range between -25 and -20°C . The size ranges from about 20 to 1800 μm . The preceding three ice crystal size distributions are used for the computations of the single-scattering properties of cirrus clouds associated with the ARES channels.

2.3 Scattering and Absorption Properties of Ice Crystals

An exact solution for the scattering of light by hexagonal ice crystals covering all shapes and sizes does not exist in practical terms. Several numerical methods that have been developed to solve the problem of light scattering by nonspherical particles are usually applicable to size parameters smaller than approximately 20, as discussed by Liou and Takano (1994) and Yang and Liou (1995a), and the references cited therein. Significant research on solving light scattering by large hexagonal ice crystals has been carried out in the past two decades by means of the geometric ray-tracing technique, commonly employed to identify the optical

phenomena occurring in the atmosphere. However, the laws of geometric optics are applicable to the scattering of light by an ice crystal if its size is much larger than the incident wavelength.

In recent years, we have developed a Monte Carlo/geometric ray-tracing method for the computation of the scattering, absorption, and polarization properties of ice crystals with various regular and irregular structures, including solid and hollow columns, single and double plates, dendrites, bullet rosettes, and aggregates (Takano and Liou 1995). The shapes of these ice crystals are defined by appropriate geometric models and incident coordinate systems. The incident photons are traced with a hit-and-miss Monte Carlo method and followed by geometric reflection and refraction on the crystal boundaries in which absorption can be accounted for by means of stochastic procedures. Phase functions for shapes covering all possible ice crystal structures can be computed using this method. Thus, at this point, we can compute the single-scattering properties for large ice crystals of any shape that can be defined mathematically or numerically.

The geometric ray-tracing requires the principle of localization in which the particle size must be larger than the incident wavelength. In addition, it is assumed that the energy attenuated by the scatterer may be decomposed into equal extinction from diffraction and Fresnelian rays so that the extinction efficiency is equal to 2 regardless of the particle size parameter. To circumvent a number of shortcomings in the geometric ray-tracing approach, we have developed a novel improvement by mapping the equivalent tangential electric and magnetic currents on the particle surface that are determined from geometric reflection and refraction to far-field by means of the fundamental electromagnetic wave theory (Yang and Liou 1996a).

For verification of the limitation of the improved geometric ray-tracing method, referred to as the geometric-optics/integral-equation method (GOM2), we have also developed a finite-difference time domain (FDTD) technique, pioneered by the electrical engineers for the identification of irregular objects. It is a numerical technique for the solution of the Maxwell equations using appropriate absorbing boundary conditions and is considered to be the "exact" numerical solution for light scattering by particles, as verified by the exact Mie-type results for long circular cylinders and spheres (Yang and Liou 1996b). Because of solution

convergence and required computer time, the FDTD method is applicable to size parameters smaller than about 20. The conventional geometric optics method breaks down when the size parameters of ice crystals are smaller than about 40-100, depending on whether the computations are for the cross sections or phase matrix. Based on comparison with the results computed from the FDTD method, the GOM2 technique is shown to be applicable to ice crystal size parameters on the order of 15-20. By combining the GOM2 and FDTD methods, referred to as the unified theory for light scattering, calculations for the scattering and absorption properties of ice crystals for all sizes and shapes can be carried out.

Figures 3-5 show the computed phase functions for the three representative size distributions described in Section 2.2 and for the 75 ARES channels. Their associated single-scattering parameters are given in Tables 1-3. In the calculations, it is assumed that the ice crystal size distributions are composed of 50% bullet rosettes, 30% hollow columns and 20% plates. It is noted that between 2 to 2.5 μm , the 22° and 46° halos, and the backscattering peak are prominent for the December 5 case, but are less distinct for the other two cases. For the cold cirrus, significant side scattering is evident. In addition, for the cold cirrus, the forward scattering peaks are one to two orders of magnitude smaller than those for the other two size distributions.

2.4 Effects of Small Ice Crystals on the Single-Scattering Properties

Recent observations reveal that there may be a large amount of small ice crystals on the order of 10 μm in cirrus clouds (Platt et al. 1989). Small ice crystals were also observed in abundant amount in tropical convective anvils (McFarquhar and Heymsfield 1996; Heymsfield and McFarquhar 1996) as well as in contrail cirrus (Gayet et al. 1996) and in orographic wave clouds (Heymsfield and Miloshevich 1993). The presence of small ice crystals has been a subject of constant debate in the study of cirrus microphysical and radiative properties. Due to the high scattering efficiency of small ice crystal, the reflectance of cirrus clouds is very sensitive to them. To accurately quantify the effect of small ice crystals on the cirrus cloud radiative properties, reliable ice crystal size distributions for the size range between ~5 and 100 μm are needed. Until recently, it was extremely difficult to measure the sizes of small ice crystals with confidence. The FSSP that

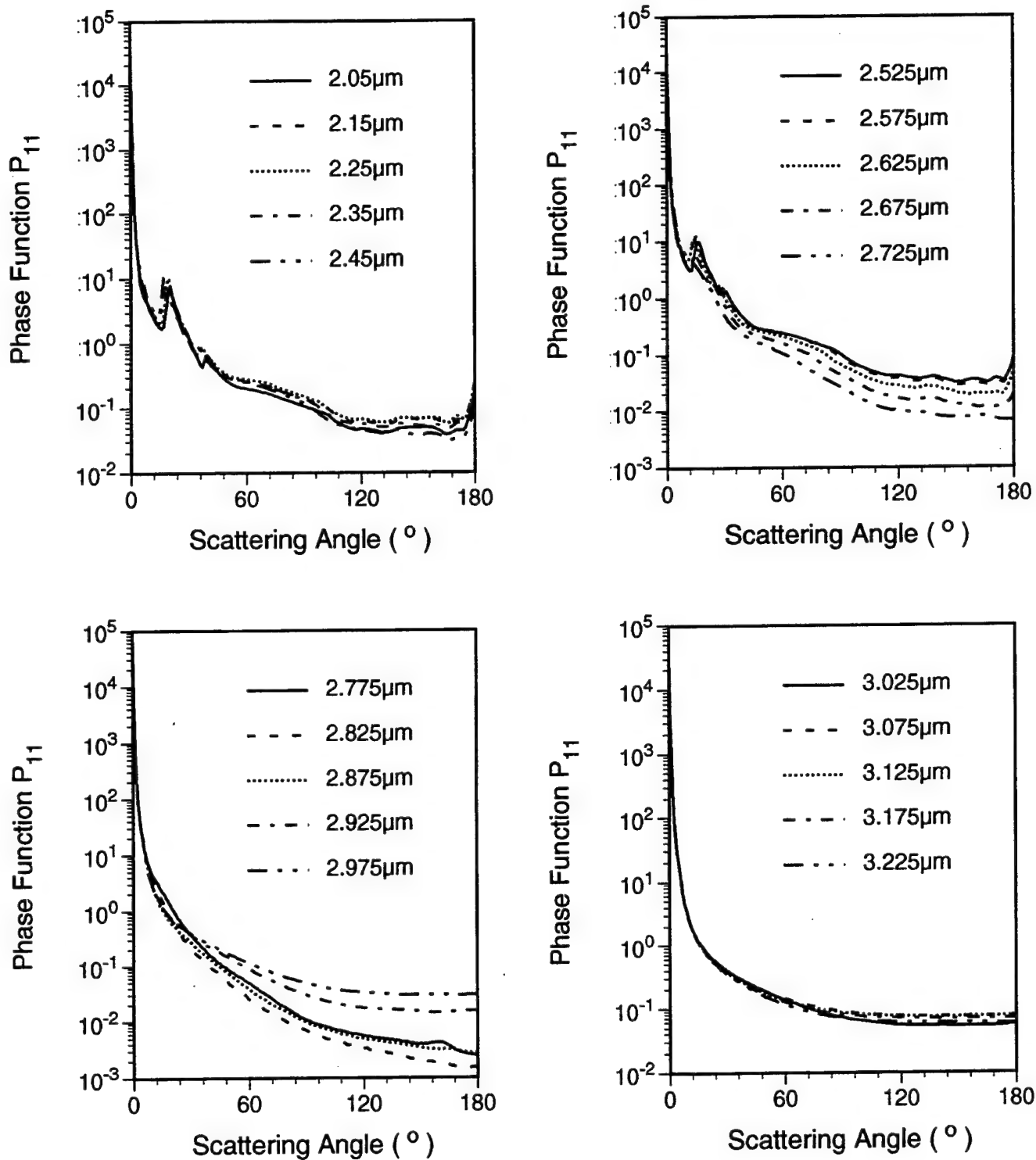


Figure 3 Phase functions for the December 5 ice crystal size distribution and for the ARES 75-channel spectral wavelengths.

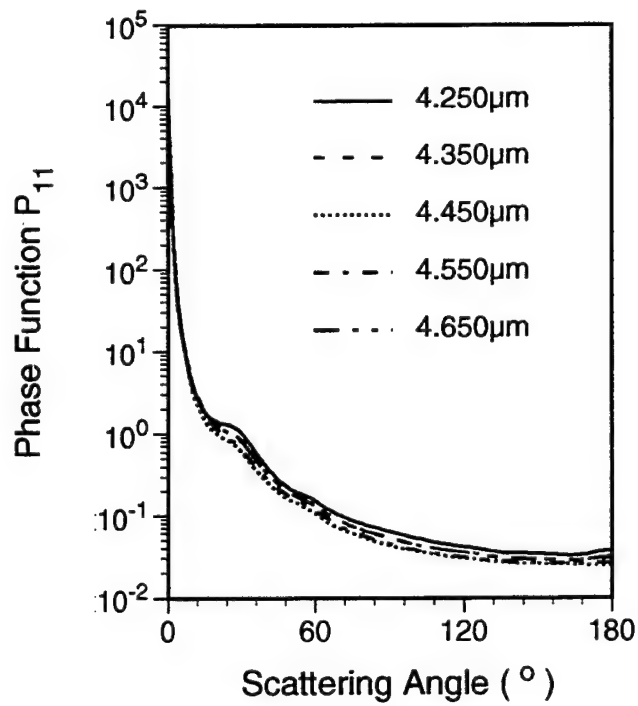
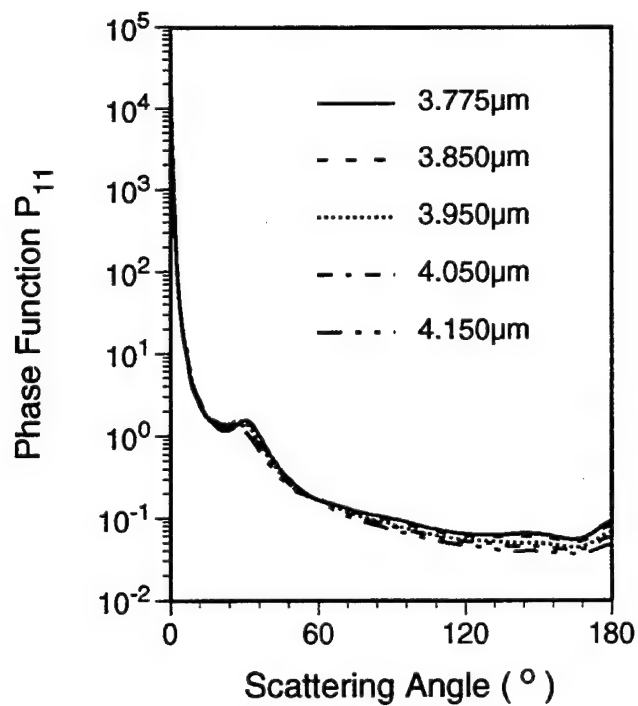
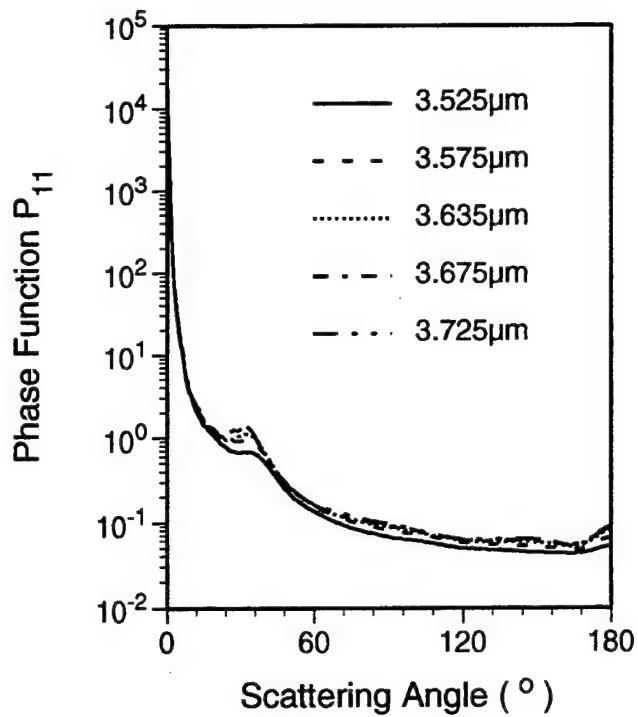
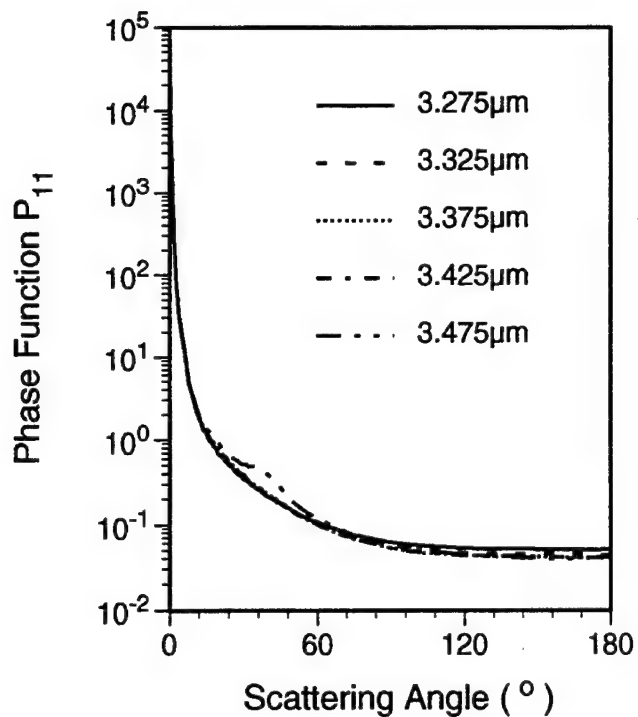


Figure 3 Continued.

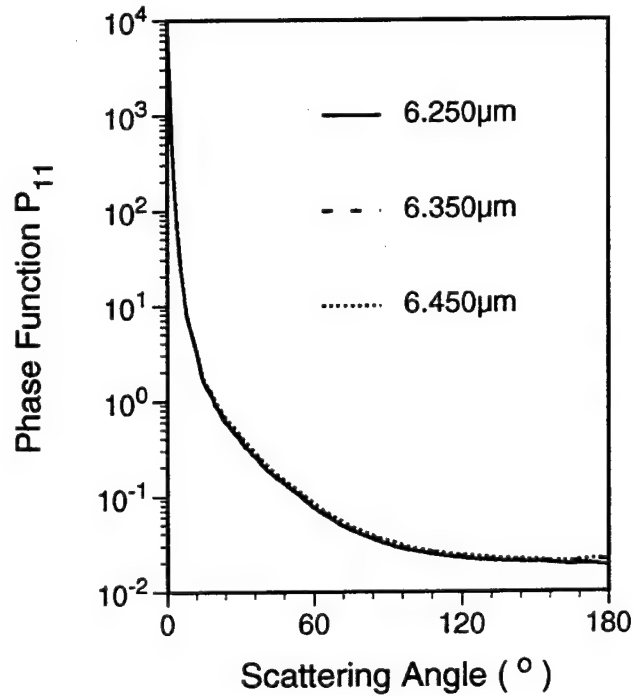
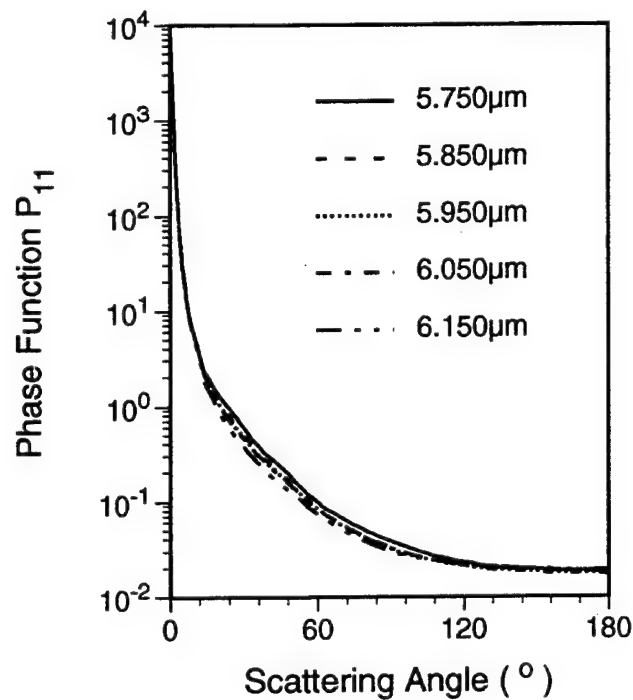
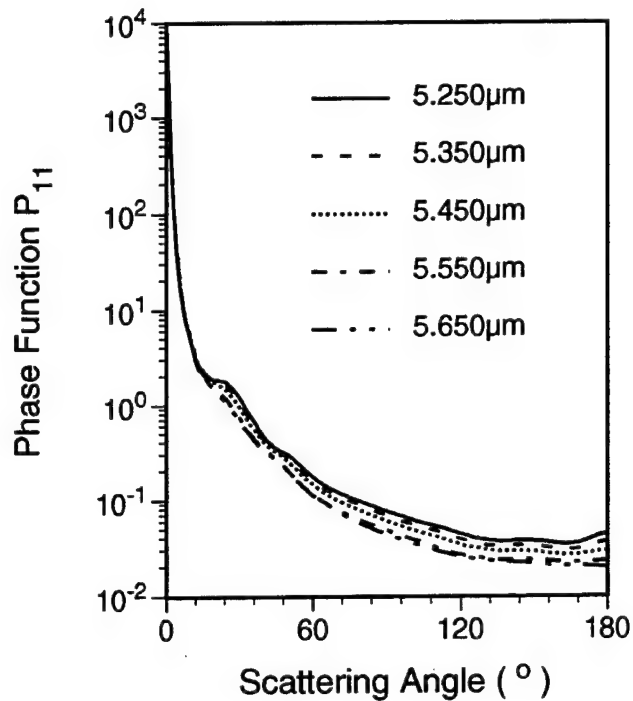
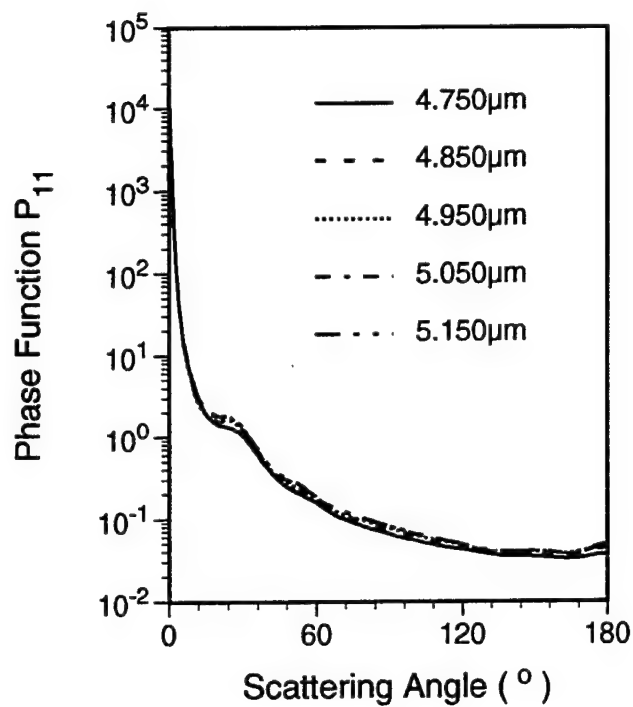


Figure 3 Continued.

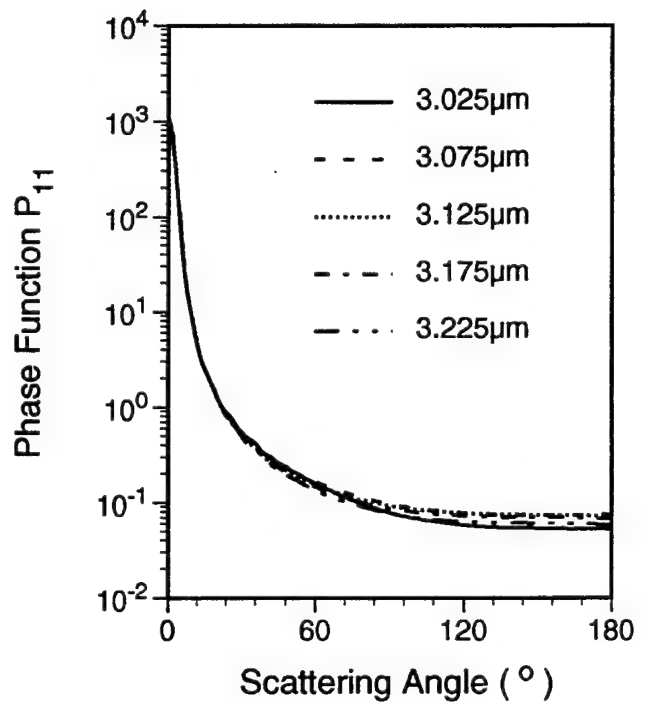
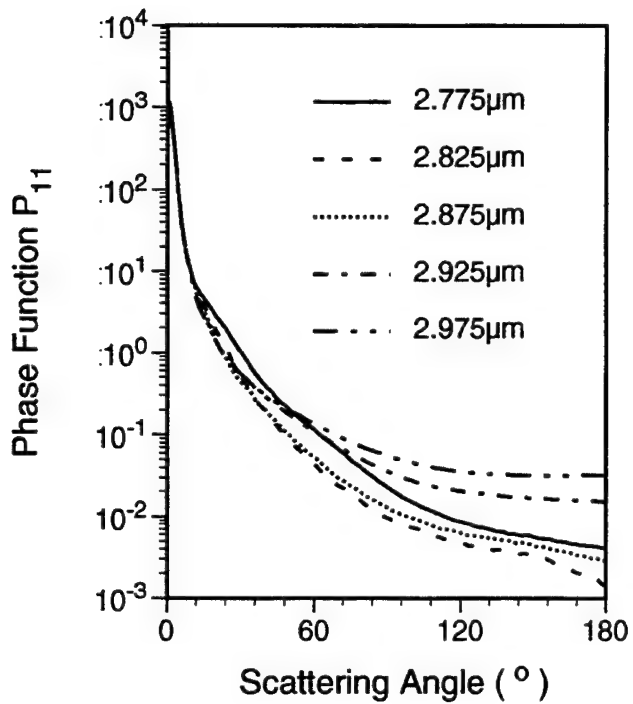
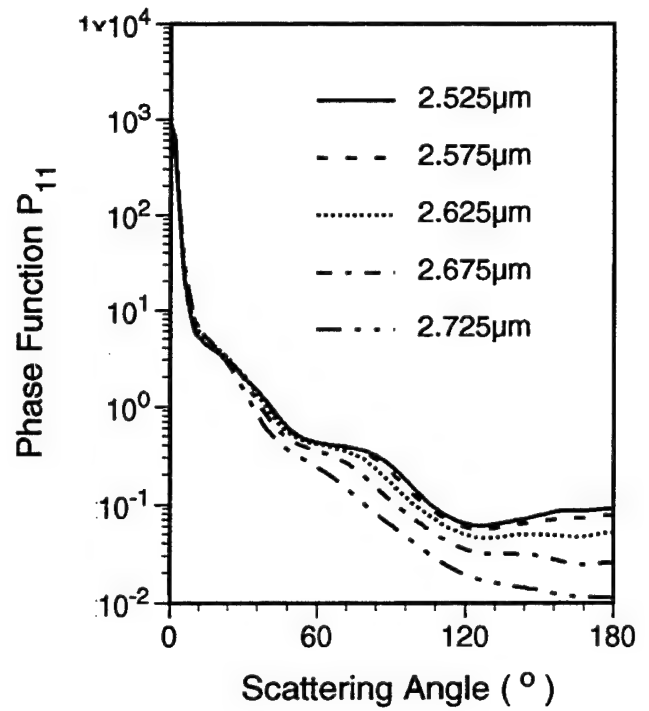
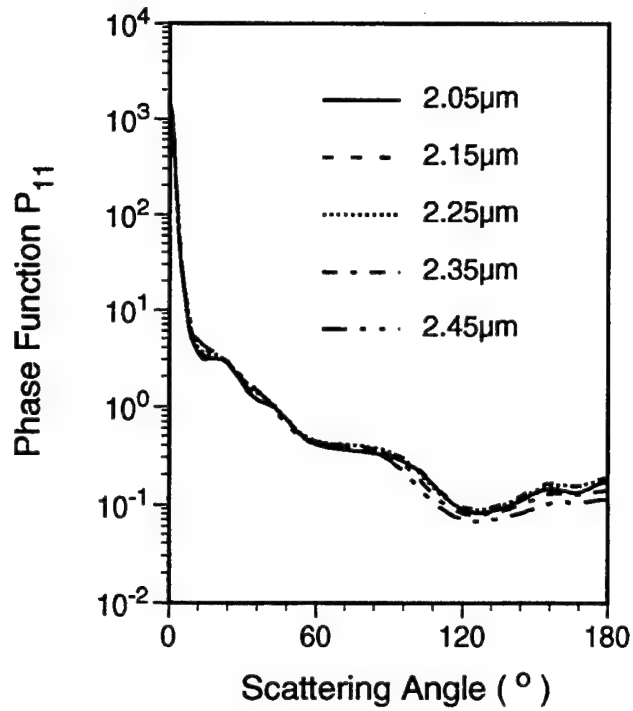


Figure 4 Same as Figure 3, except for cold cirrus.

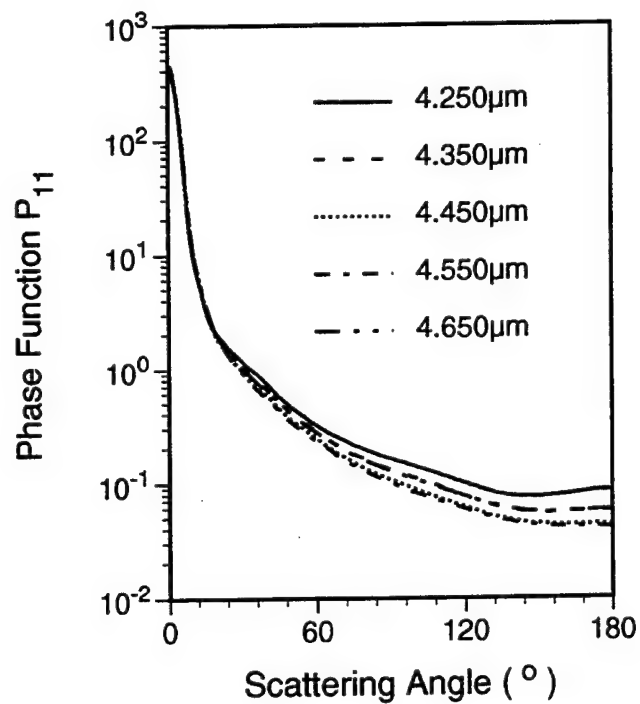
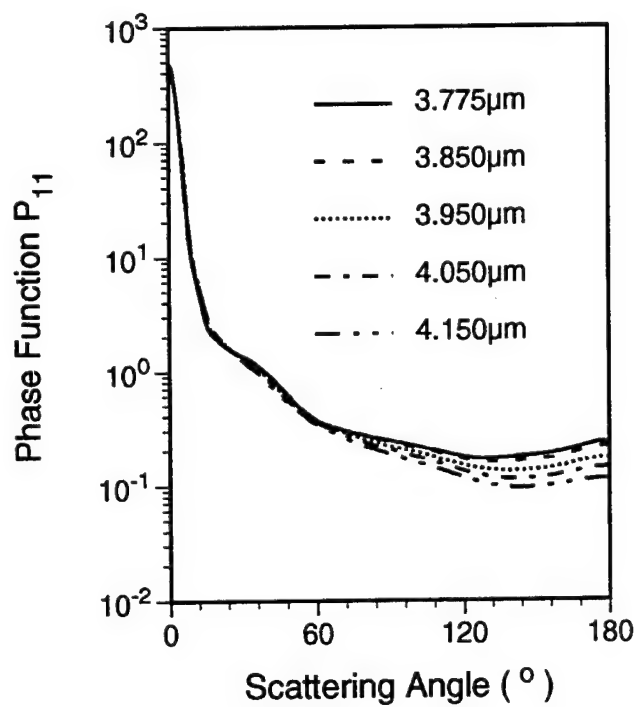
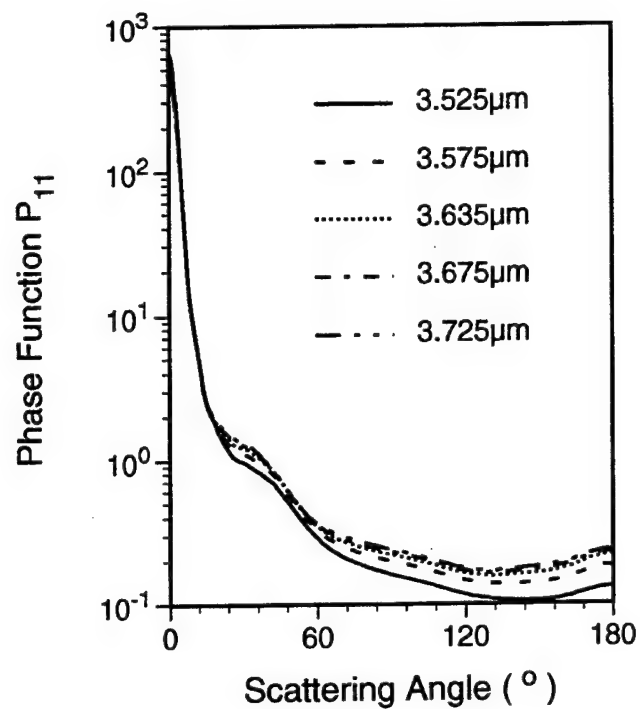
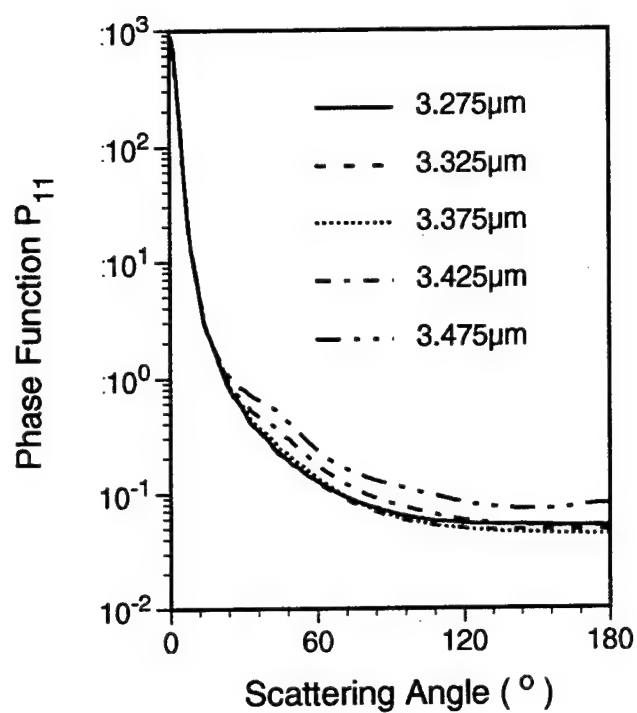


Figure 4 Continued.

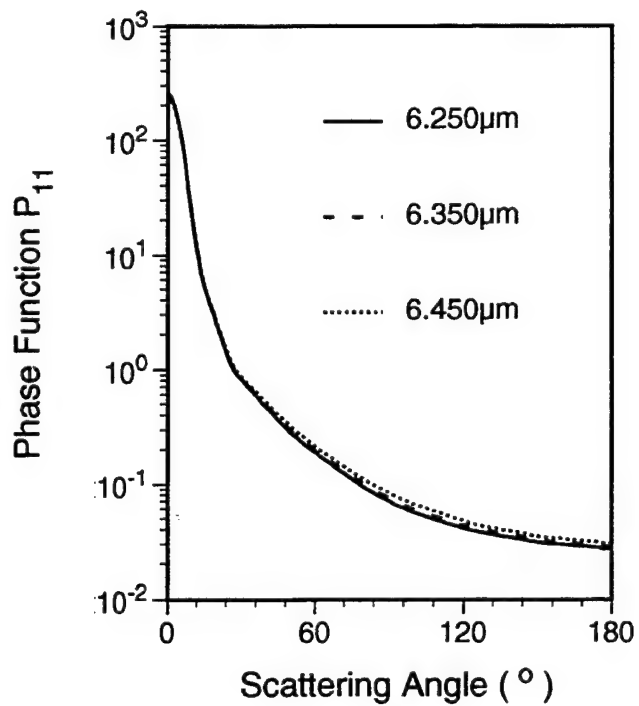
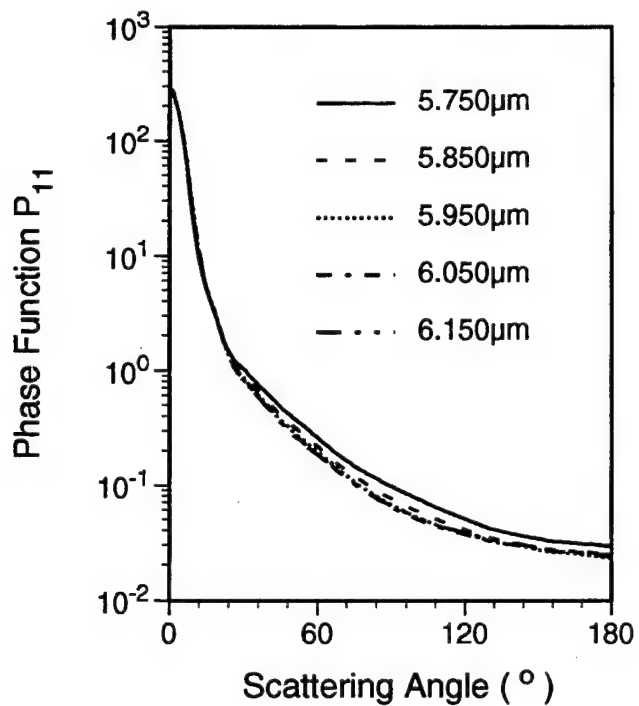
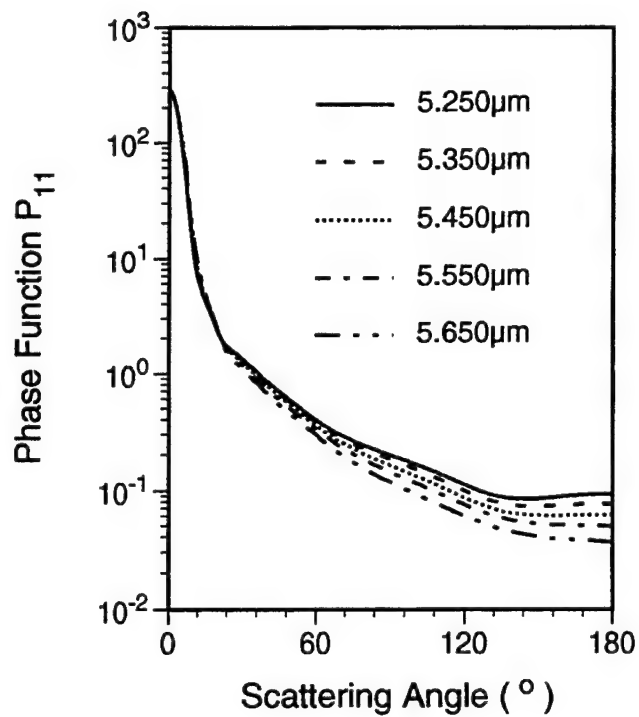
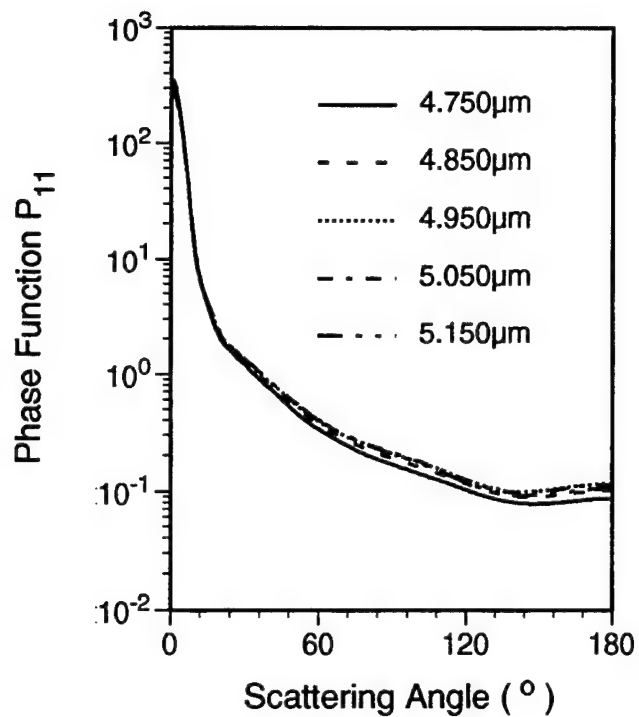


Figure 4 Continued.

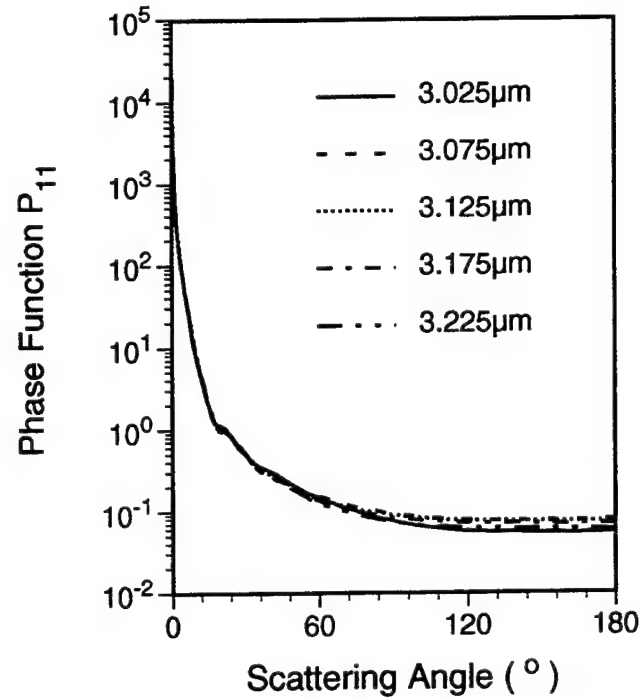
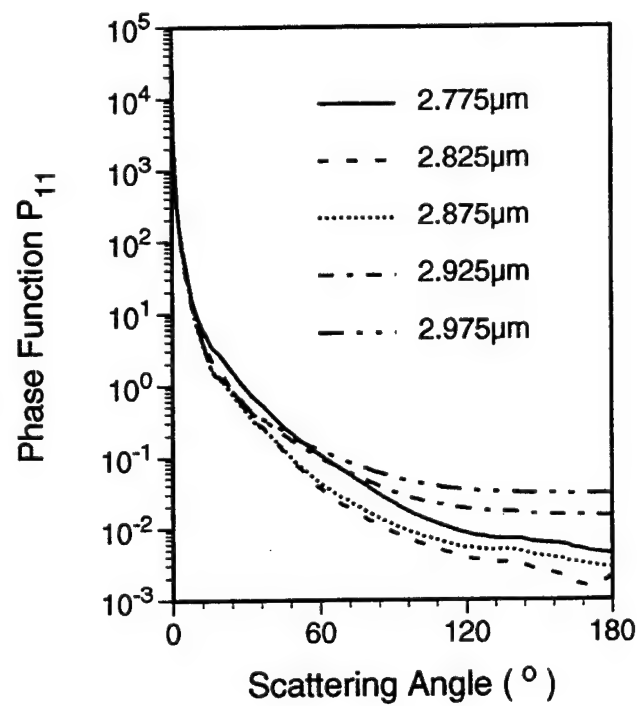
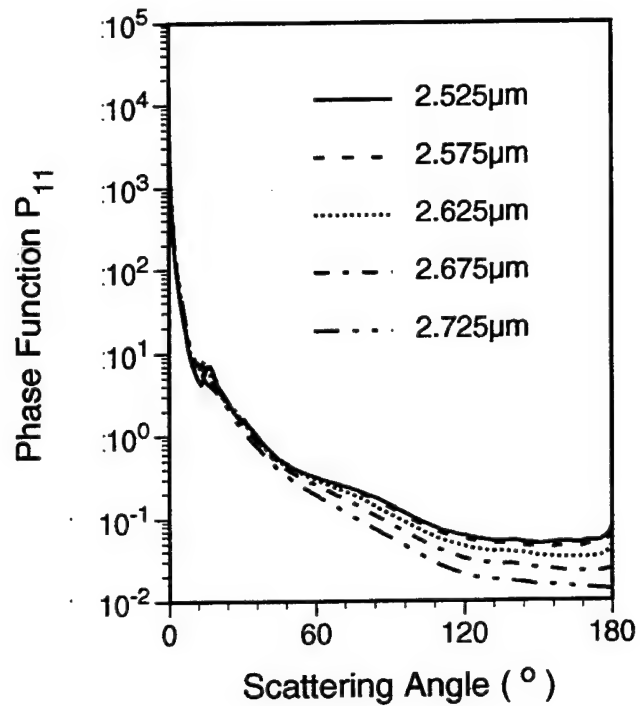
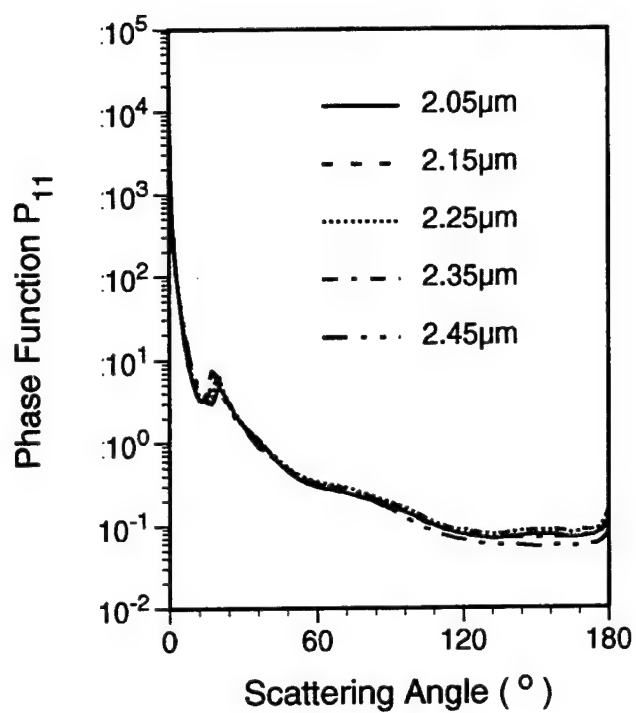


Figure 5 Same as Figure 3, except for warm cirrus clouds.

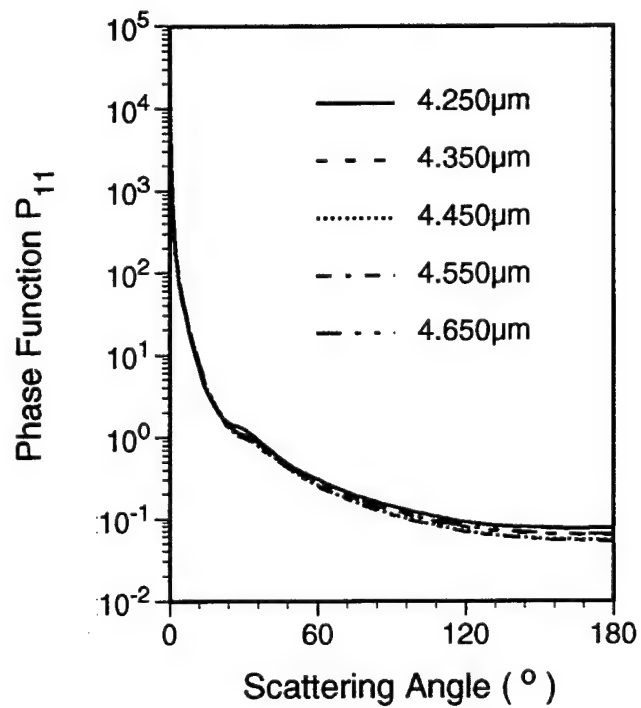
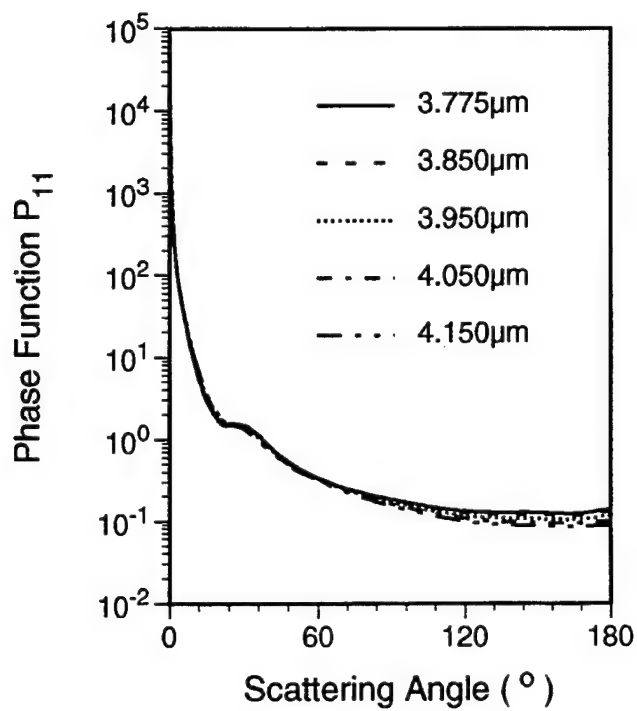
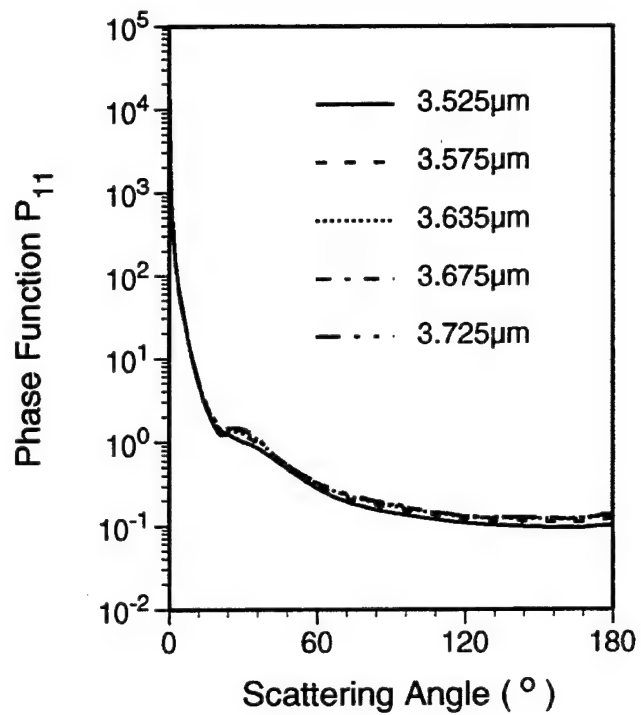
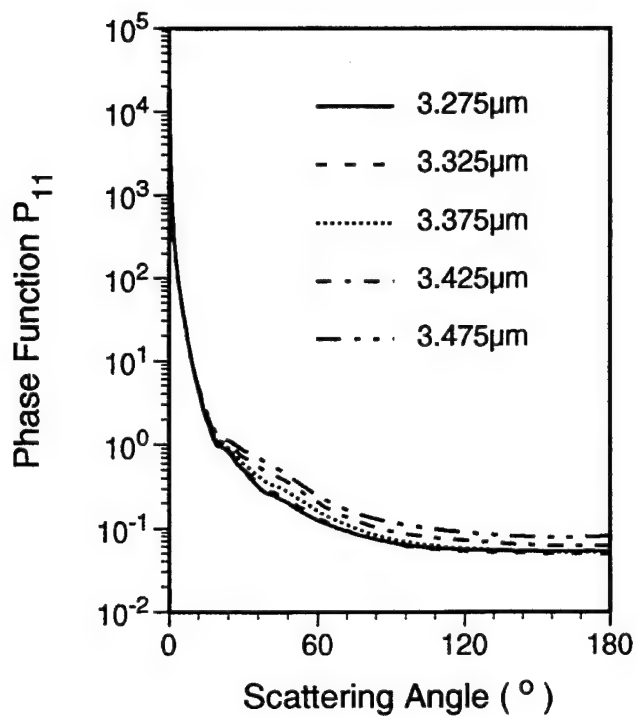


Figure 5 Continued.

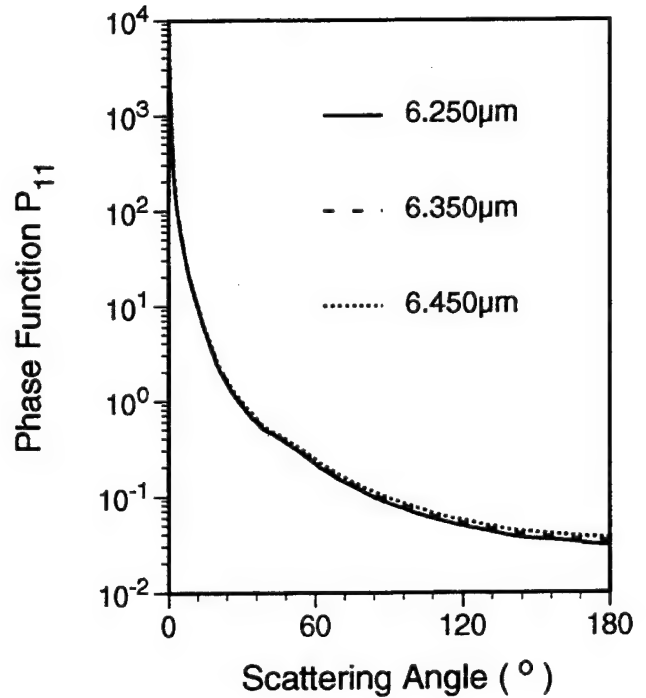
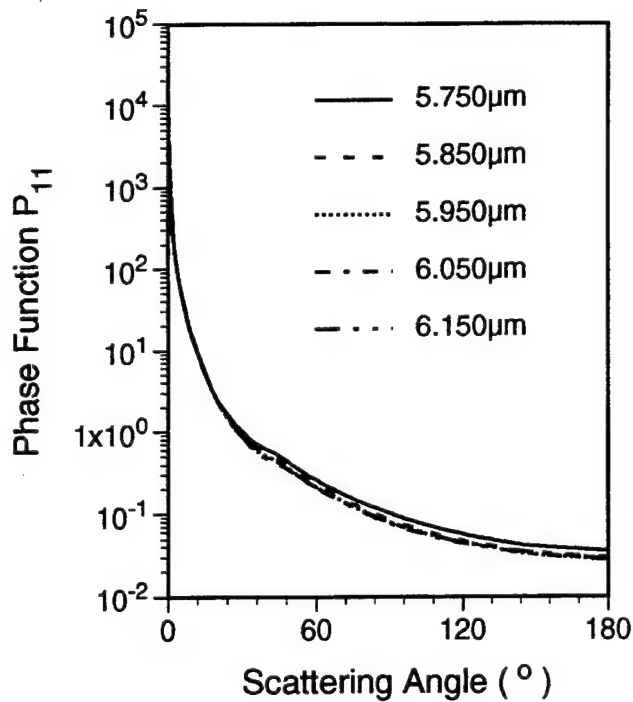
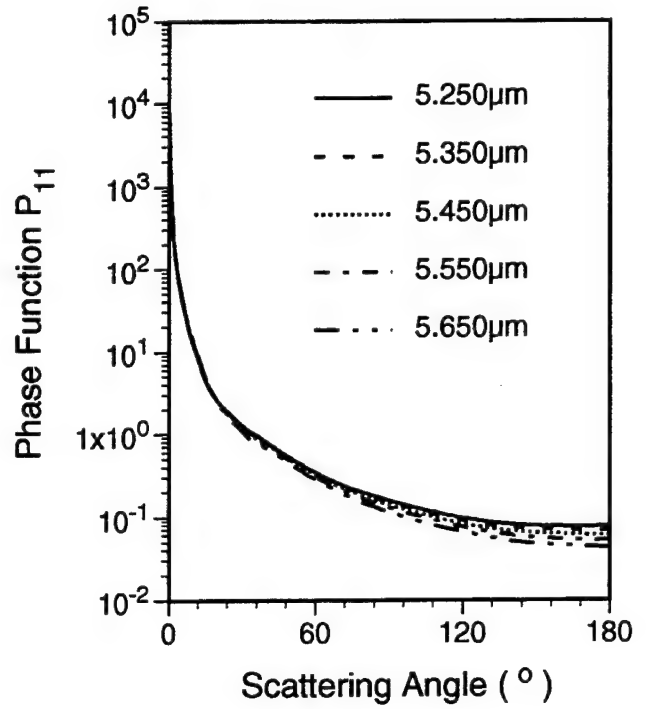
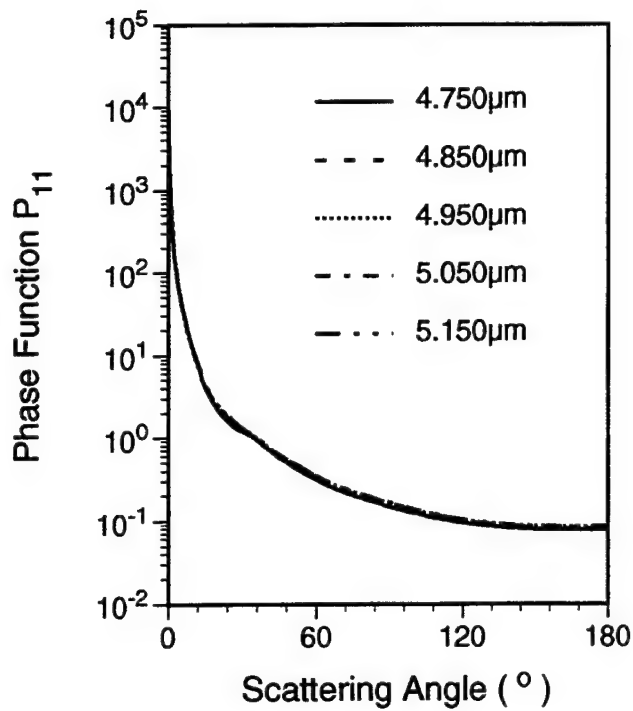


Figure 5 Continued.

Table 1. Refractive indices and single-scattering parameters for the December 5 ice crystal size distribution and for the ARES 75-channel spectral wavelengths.

$\langle \lambda \rangle$ (μm)	$\Delta \lambda$ (μm)	$\langle m_r \rangle$	$\langle m_i \rangle$	$\langle \beta_e \rangle$ (1/km)	$\langle \omega \rangle$	$\langle g \rangle$	file-name
2.05	0.1	1.272	.1311E-2	.32867	.82771	.90952	phase-01
2.15	0.1	1.266	.4884E-2	.32892	.92135	.88833	phase-02
2.25	0.1	1.258	.2377E-3	.32832	.96001	.88031	phase-03
2.35	0.1	1.247	.5368E-3	.32949	.92271	.89173	phase-04
2.45	0.1	1.234	.8220E-3	.33215	.89749	.90363	phase-05
2.525	0.05	1.221	.9126E-3	.32822	.89080	.91130	phase-06
2.575	0.05	1.209	.9043E-3	.32839	.89458	.91546	phase-07
2.625	0.05	1.193	.1621E-3	.32987	.84245	.93049	phase-08
2.675	0.05	1.173	.3747E-3	.33466	.74534	.94917	phase-09
2.725	0.05	1.146	.8782E-2	.33114	.63457	.96619	phase-10
2.775	0.05	1.109	.2045E-1	.32280	.55014	.98133	phase-11
2.825	0.05	1.057	.4656E-1	.32019	.51760	.98880	phase-12
2.875	0.05	.9921	.1153E0	.32255	.52110	.98526	phase-13
2.925	0.05	.9704	.2484E0	.35315	.57494	.96502	phase-14
2.975	0.05	1.014	.3670E0	.36581	.59737	.94746	phase-15
3.025	0.05	1.093	.5066E0	.37080	.61279	.92473	phase-16
3.075	0.05	1.311	.6093E0	.35713	.60443	.90683	phase-17
3.125	0.05	1.521	.5154E0	.34186	.58258	.90981	phase-18
3.175	0.05	1.629	.3701E0	.33449	.56897	.91553	phase-19
3.225	0.05	1.635	.2197E0	.33101	.55864	.92494	phase-20
3.275	0.05	1.596	.1314E0	.32985	.55303	.93263	phase-21
3.325	0.05	1.556	.8218E-1	.32950	.55033	.93818	phase-22
3.375	0.05	1.521	.5026E-1	.32963	.55137	.94100	phase-23
3.425	0.05	1.491	.3088E0	.32865	.55802	.94008	phase-24
3.475	0.05	1.465	.1997E-1	.32864	.57650	.93478	phase-25
3.525	0.05	1.446	.1362E-1	.32883	.60449	.92512	phase-26
3.575	0.05	1.429	.9998E-2	.32831	.63390	.91194	phase-27
3.625	0.1	1.416	.8175E-2	.32794	.65764	.90677	phase-28
3.675	0.1	1.405	.7467E-2	.32788	.67002	.90411	phase-29

Table 1--continued.

$\langle \lambda \rangle$ (μm)	$\Delta \lambda$ (μm)	$\langle m_i \rangle$	$\langle \beta_e \rangle$ (1/km)	$\langle \omega \rangle$	$\langle g \rangle$	file-name
3.725	0.1	1.396	.32905	.68197	.90138	phase-30
3.775	0.1	1.387	.33020	.69004	.90021	phase-31
3.850	0.1	1.377	.33099	.68522	.90401	phase-32
3.950	0.1	1.367	.33157	.66491	.91159	phase-33
4.050	0.1	1.358	.32937	.64729	.91478	phase-34
4.150	0.1	1.351	.32831	.63011	.92206	phase-35
4.250	0.1	1.344	.32879	.61182	.93000	phase-36
4.350	0.1	1.339	.32926	.58889	.93978	phase-37
4.450	0.1	1.339	.32956	.57272	.95024	phase-38
4.550	0.1	1.344	.32965	.56885	.94756	phase-39
4.650	0.1	1.345	.32986	.58612	.93990	phase-40
4.750	0.1	1.342	.33054	.61607	.92803	phase-41
4.850	0.1	1.337	.33174	.63628	.92057	phase-42
4.950	0.1	1.332	.33327	.65461	.91316	phase-43
5.050	0.1	1.326	.33409	.66025	.91450	phase-44
5.150	0.1	1.321	.33400	.65637	.91367	phase-45
5.250	0.1	1.315	.33375	.64988	.91736	phase-46
5.350	0.1	1.309	.33316	.63531	.92443	phase-47
5.450	0.1	1.303	.33234	.61721	.93234	phase-48
5.550	0.1	1.2976	.33049	.59775	.94538	phase-49
5.650	0.1	1.292	.32989	.57941	.94817	phase-50
5.750	0.1	1.287	.32850	.56344	.95449	phase-51
5.850	0.1	1.286	.32763	.54922	.95961	phase-52
5.950	0.1	1.293	.32783	.54451	.96067	phase-53
6.050	0.1	1.301	.32800	.54292	.96035	phase-54
6.150	0.1	1.310	.32828	.54324	.96312	phase-55
6.250	0.1	1.317	.32853	.54521	.96173	phase-56
6.350	0.1	1.321	.32837	.54744	.96022	phase-57
6.450	0.1	1.321	.32808	.55053	.95867	phase-58

Table 2. Same as Table 1, except for the cold cirrus ice crystal size distribution.

$\langle \lambda \rangle$ (μm)	$\Delta \lambda$ (μm)	$\langle m_r \rangle$	$\langle m_i \rangle$	$\langle \beta_e \rangle$ (1/km)	$\langle \omega \rangle$	$\langle g \rangle$	file-name
2.05	0.1	1.272	.1311E-2	.530702	.910204	.775518	pcold-01
2.15	0.1	1.266	.4884E-2	.530140	.965398	.757818	pcold-02
2.25	0.1	1.258	.2377E-3	.528807	.983621	.759290	pcold-03
2.35	0.1	1.247	.5368E-3	.533832	.966385	.776286	pcold-04
2.45	0.1	1.234	.8220E-3	.537950	.952987	.795145	pcold-05
2.525	0.05	1.221	.9126E-3	.531130	.949965	.809074	pcold-06
2.575	0.05	1.209	.9043E-3	.520972	.951167	.820148	pcold-07
2.625	0.05	1.193	.1621E-3	.516250	.919289	.843176	pcold-08
2.675	0.05	1.173	.3747E-3	.530286	.847334	.878910	pcold-09
2.725	0.05	1.146	.8782E-2	.533080	.736312	.921280	pcold-10
2.775	0.05	1.109	.2045E-1	.518707	.615811	.957305	pcold-11
2.825	0.05	1.057	.4656E-1	.486224	.527054	.977910	pcold-12
2.875	0.05	.9921	.1153E0	.477822	.503038	.976493	pcold-13
2.925	0.05	.9704	.2484E0	.547116	.571004	.954689	pcold-14
2.975	0.05	1.014	.3670E0	.575556	.597385	.937186	pcold-15
3.025	0.05	1.093	.5066E0	.588629	.614516	.914800	pcold-16
3.075	0.05	1.311	.6093E0	.570400	.607396	.897824	pcold-17
3.125	0.05	1.521	.5154E0	.547013	.586022	.900297	pcold-18
3.175	0.05	1.629	.3701E0	.535532	.572615	.905407	pcold-19
3.225	0.05	1.635	.2197E0	.530469	.562166	.914923	pcold-20
3.275	0.05	1.596	.1314E0	.529007	.555946	.923030	pcold-21
3.325	0.05	1.556	.8218E-1	.528186	.552685	.927638	pcold-22
3.375	0.05	1.521	.5026E-1	.528174	.556656	.926486	pcold-23
3.425	0.05	1.491	.3088E0	.528317	.576484	.910145	pcold-24
3.475	0.05	1.465	.1997E-1	.529106	.615468	.876553	pcold-25
3.525	0.05	1.446	.1362E-1	.529913	.665556	.834863	pcold-26
3.575	0.05	1.429	.9998E-2	.529462	.712459	.797506	pcold-27
3.625	0.1	1.416	.8175E-2	.529681	.744516	.774894	pcold-28
3.675	0.1	1.405	.7467E-2	.530509	.760609	.765498	pcold-29

Table 2--continued.

$\langle \lambda \rangle$ (μm)	$\Delta \lambda$ (μm)	$\langle m_r \rangle$	$\langle m_i \rangle$	$\langle \beta_e \rangle$ (1/km)	$\langle \omega \rangle$	$\langle g \rangle$	file-name
3.725	0.1	1.396	.6941E-2	.532974	.774704	.758153	pcold-30
3.775	0.1	1.387	.6668E-2	.534633	.783571	.755203	pcold-31
3.850	0.1	1.377	.7158E-2	.537017	.778249	.763720	pcold-32
3.950	0.1	1.367	.8802E-2	.536152	.752623	.786317	pcold-33
4.050	0.1	1.358	.1037E-1	.532086	.731028	.803654	pcold-34
4.150	0.1	1.351	.1234E-1	.527141	.706643	.821914	pcold-35
4.250	0.1	1.344	.1525E-1	.522797	.676554	.843231	pcold-36
4.350	0.1	1.339	.2044E-1	.521384	.637346	.871243	pcold-37
4.450	0.1	1.339	.2626E-1	.521608	.608291	.891561	pcold-38
4.550	0.1	1.344	.2893E-1	.521603	.599518	.896390	pcold-39
4.650	0.1	1.345	.2286E-1	.520144	.629814	.872495	pcold-40
4.750	0.1	1.342	.1667E-1	.519355	.678040	.837618	pcold-41
4.850	0.1	1.337	.1418E-1	.520946	.707615	.819394	pcold-42
4.950	0.1	1.332	.1247E-1	.524525	.733287	.804843	pcold-43
5.050	0.1	1.326	.1225E-1	.529063	.742291	.802660	pcold-44
5.150	0.1	1.321	.1295E-1	.533224	.739840	.807586	pcold-45
5.250	0.1	1.315	.1399E-1	.536741	.733726	.814740	pcold-46
5.350	0.1	1.309	.1622E-1	.537479	.715693	.828347	pcold-47
5.450	0.1	1.303	.1958E-1	.536710	.690635	.844996	pcold-48
5.550	0.1	1.2976	.2402E-1	.534071	.663834	.860158	pcold-49
5.650	0.1	1.292	.3054E-1	.530414	.631042	.880524	pcold-50
5.750	0.1	1.287	.3871E-1	.527084	.602958	.896493	pcold-51
5.850	0.1	1.286	.5188E-1	.525767	.575116	.913060	pcold-52
5.950	0.1	1.293	.6156E-1	.525780	.563319	.919821	pcold-53
6.050	0.1	1.301	.6786E-1	.526078	.558247	.921982	pcold-54
6.150	0.1	1.310	.6937E-1	.526337	.557999	.920986	pcold-55
6.250	0.1	1.317	.6670E-1	.526910	.561754	.916562	pcold-56
6.350	0.1	1.321	.6273E-1	.526879	.566058	.912735	pcold-57
6.450	0.1	1.321	.5738E-1	.526678	.573359	.906135	pcold-58

Table 3. Same as Table 1, except for the warm cirrus ice crystal size distribution.

$\langle \lambda \rangle$ (μm)	$\Delta \lambda$ (μm)	$\langle m_r \rangle$	$\langle m_i \rangle$	$\langle \beta_e \rangle$ (1/km)	$\langle \omega \rangle$	$\langle g \rangle$	file-name
2.05	0.1	1.272	.1311E-2	.853374	.873824	.851634	pwarm-01
2.15	0.1	1.266	.4884E-2	.857677	.942038	.838223	pwarm-02
2.25	0.1	1.258	.2377E-3	.865357	.970386	.836148	pwarm-03
2.35	0.1	1.247	.5368E-3	.861403	.943160	.847098	pwarm-04
2.45	0.1	1.234	.8220E-3	.860749	.925341	.860672	pwarm-05
2.525	0.05	1.221	.9126E-3	.863303	.920632	.867053	pwarm-06
2.575	0.05	1.209	.9043E-3	.866857	.923556	.872836	pwarm-07
2.625	0.05	1.193	.1621E-3	.865832	.885520	.886992	pwarm-08
2.675	0.05	1.173	.3747E-3	.869418	.811115	.906057	pwarm-09
2.725	0.05	1.146	.8782E-2	.867516	.721483	.928956	pwarm-10
2.775	0.05	1.109	.2045E-1	.823934	.623984	.960035	pwarm-11
2.825	0.05	1.057	.4656E-1	.717190	.503445	.981858	pwarm-12
2.875	0.05	.9921	.1153E0	.746233	.496099	.980158	pwarm-13
2.925	0.05	.9704	.2484E0	.860472	.564363	.958861	pwarm-14
2.975	0.05	1.014	.3670E0	.908283	.591565	.941170	pwarm-15
3.025	0.05	1.093	.5066E0	.929036	.608624	.918620	pwarm-16
3.075	0.05	1.311	.6093E0	.901165	.601861	.901054	pwarm-17
3.125	0.05	1.521	.5154E0	.864653	.580652	.903952	pwarm-18
3.175	0.05	1.629	.3701E0	.846916	.567492	.909291	pwarm-19
3.225	0.05	1.635	.2197E0	.836525	.557007	.918213	pwarm-20
3.275	0.05	1.596	.1314E0	.827928	.551078	.924237	pwarm-21
3.325	0.05	1.556	.8218E-1	.824126	.553299	.924783	pwarm-22
3.375	0.05	1.521	.5026E-1	.828059	.569628	.915866	pwarm-23
3.425	0.05	1.491	.3088E0	.836108	.599481	.896161	pwarm-24
3.475	0.05	1.465	.1997E-1	.845986	.637429	.871478	pwarm-25
3.525	0.05	1.446	.1362E-1	.853883	.677156	.846945	pwarm-26
3.575	0.05	1.429	.9998E-2	.860133	.712899	.828619	pwarm-27
3.625	0.1	1.416	.8175E-2	.864653	.737567	.818622	pwarm-28
3.675	0.1	1.405	.7467E-2	.864382	.749253	.814987	pwarm-29

Table 3--continued.

$\langle \lambda \rangle$ (μm)	$\Delta \lambda$ (μm)	$\langle m_r \rangle$	$\langle m_i \rangle$	$\langle \beta_e \rangle$ (1/km)	$\langle \omega \rangle$	$\langle g \rangle$	file-name
3.725	0.1	1.396	.6941E-2	.862724	.758668	.812457	pwarm-30
3.775	0.1	1.387	.6668E-2	.860387	.764313	.811327	pwarm-31
3.850	0.1	1.377	.7158E-2	.861378	.759808	.815675	pwarm-32
3.950	0.1	1.367	.8802E-2	.860953	.740898	.826397	pwarm-33
4.050	0.1	1.358	.1037E-1	.862760	.727105	.835117	pwarm-34
4.150	0.1	1.351	.1234E-1	.864368	.712293	.843776	pwarm-35
4.250	0.1	1.344	.1525E-1	.864666	.693274	.854192	pwarm-36
4.350	0.1	1.339	.2044E-1	.864102	.666881	.868914	pwarm-37
4.450	0.1	1.339	.2626E-1	.863382	.645914	.880544	pwarm-38
4.550	0.1	1.344	.2893E-1	.863275	.639262	.882837	pwarm-39
4.650	0.1	1.345	.2286E-1	.865203	.662680	.867584	pwarm-40
4.750	0.1	1.342	.1667E-1	.867638	.696783	.849207	pwarm-41
4.850	0.1	1.337	.1418E-1	.869402	.716707	.840644	pwarm-42
4.950	0.1	1.332	.1247E-1	.871361	.734663	.835960	pwarm-43
5.050	0.1	1.326	.1225E-1	.872347	.738441	.833215	pwarm-44
5.150	0.1	1.321	.1295E-1	.873059	.735262	.835837	pwarm-45
5.250	0.1	1.315	.1399E-1	.874128	.729915	.839665	pwarm-46
5.350	0.1	1.309	.1622E-1	.874958	.717012	.846579	pwarm-47
5.450	0.1	1.303	.1958E-1	.874478	.699679	.856069	pwarm-48
5.550	0.1	1.2976	.2402E-1	.871820	.681989	.865979	pwarm-49
5.650	0.1	1.292	.3054E-1	.867902	.658296	.879146	pwarm-50
5.750	0.1	1.287	.3871E-1	.862226	.636949	.891773	pwarm-51
5.850	0.1	1.286	.5188E-1	.855598	.612431	.905847	pwarm-52
5.950	0.1	1.293	.6156E-1	.852949	.600295	.911329	pwarm-53
6.050	0.1	1.301	.6786E-1	.851752	.594357	.913173	pwarm-54
6.150	0.1	1.310	.6937E-1	.852746	.594488	.911879	pwarm-55
6.250	0.1	1.317	.6670E-1	.855094	.599531	.907683	pwarm-56
6.350	0.1	1.321	.6273E-1	.856480	.604946	.902319	pwarm-57
6.450	0.1	1.321	.5738E-1	.858259	.612190	.896992	pwarm-58

has been used for quantifying the spherical droplet size distribution has not been calibrated for deriving the nonspherical ice crystal size distributions between ~ 5 and $100\text{ }\mu\text{m}$. On the other hand, a conservative estimate of the lower limit of ice crystal size distributions from 2D-C probes is around $75\text{ }\mu\text{m}$. Given that there are uncertainties in the ice crystal size distributions obtained from either FSSP or 2D-C probe, two fundamental aspects need to be explored. First, do we need to incorporate ice crystal size distribution for sizes less than $75\text{ }\mu\text{m}$ in the light scattering calculations? If the answer is yes, then what would be the optimal cut-off size for the small ice crystal size distribution? Second, what is the sensitivity of the single-scattering parameters to the uncertainties in the small ice crystal size distribution?

To address the preceding two questions, we have used the size distributions obtained by FSSP, 1D-C and 2D-C probes on board the HARP during the Hanscom AFB mission flight on September 16, 1995, for light scattering calculations. The FSSP sizes the ice crystals from 1 to $96\text{ }\mu\text{m}$; the 1D-C probe samples ice crystals from 20 to $300\text{ }\mu\text{m}$; and the 2D-C probe measures the maximum dimensions of the projection of ice crystals from 25 to $800\text{ }\mu\text{m}$. Examination of these ice crystal size distributions reveals that the size distributions derived from the 1D-C and 2D-C probes basically agree with each other in terms of the functional shapes and size ranges for the size distribution, although the differences in some size bin concentrations can be as large as one order of magnitude. Thus, we decided to use the 2D-C derived ice crystal size distribution for our purpose because its size range covers typical ice crystal size ranges. Moreover, we note that the FSSP derived size distributions appear to be unreliable, because the size bin concentrations are unrealistically high for sizes less than $20\text{ }\mu\text{m}$. Thus, to obtain the ice crystal size distribution for sizes less than $75\text{ }\mu\text{m}$, we use the Gamma function to extrapolate the 2D-C size distribution to $1\text{ }\mu\text{m}$.

In this study, three composite ice crystal size distributions obtained by the 2D-C probe are constructed. They are named as cases 1 to 3, and are plotted in Figure 6. The portion of the ice crystal size distribution larger than $75\text{ }\mu\text{m}$ was derived from the 2D-C probe measurements. The size distributions between 1 and $75\text{ }\mu\text{m}$ were obtained from the extrapolation. The upper bound of the maximum dimension is about $600\text{ }\mu\text{m}$.

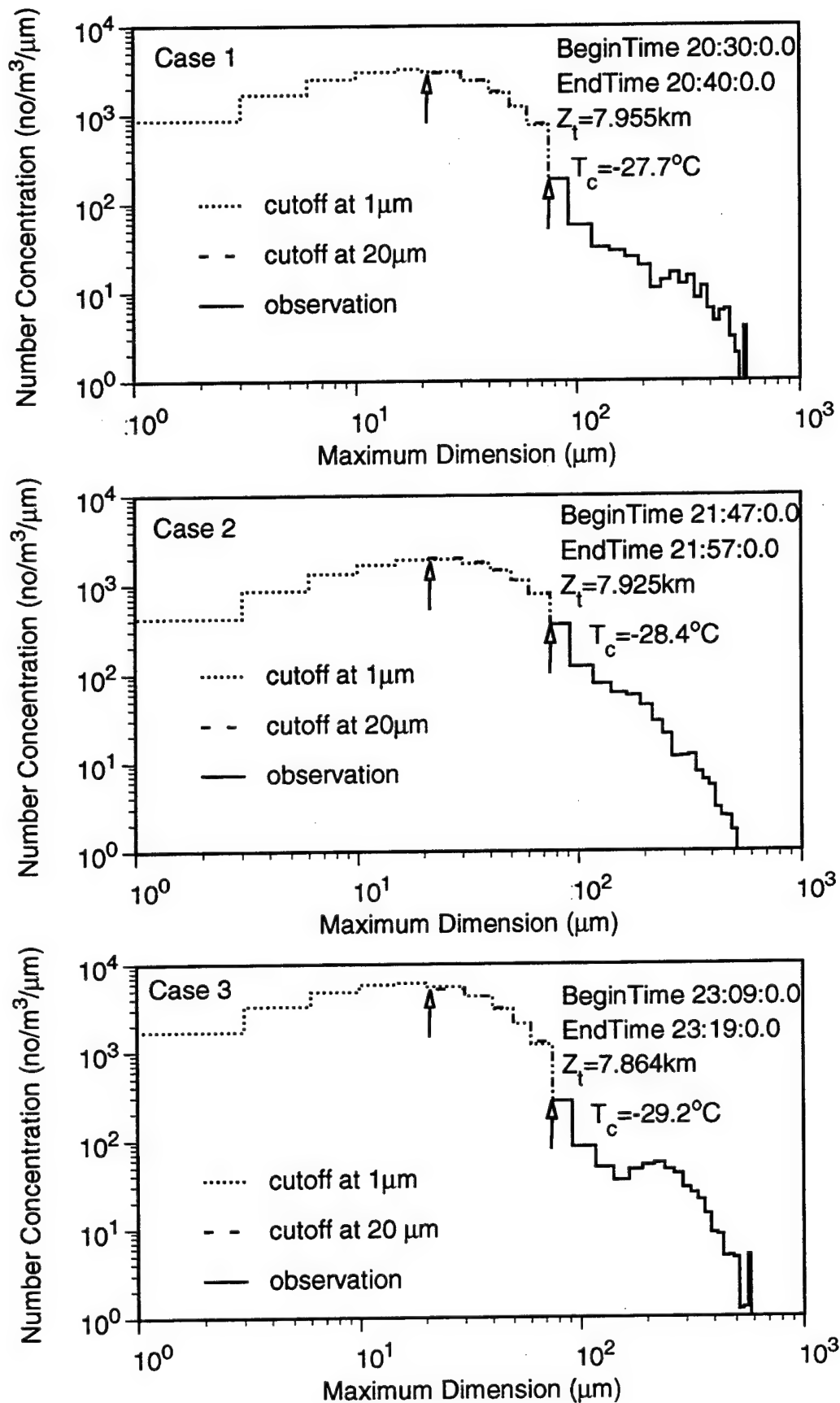


Figure 6 The ice crystal size distributions based on HARP data (09/16/95) with the lower limit of $75\mu\text{m}$ and extrapolations to $20\mu\text{m}$ and $1\mu\text{m}$ based on the Gamma function and an optimization search method.

There was no specific information on the fractional distribution of particular ice crystal shapes.

To study the radiative effects of small ice crystals, we use the unified theory for light scattering by ice crystals to compute the single-scattering properties of the aforementioned three ice crystal size distributions, including the phase function (asymmetry factor), single-scattering albedo, and extinction coefficient. To investigate the effects of different cut-off sizes on the single-scattering properties, three cut-off sizes are prescribed: 1 μm , 20 μm , and 75 μm . The cut-off size at 75 μm corresponds to no extrapolation at all. Table 4 lists the single-scattering parameters at 2.8 μm for the three cut-off sizes for each of the ice crystal size distributions. Figure 7 shows the associated normalized phase function for these three cases. It is assumed that ice crystals are composed of randomly oriented ice columns and plates. The extinction coefficient is significantly affected by the variation of cut-off sizes. The value for cut-off at 1 μm is virtually the same as that for cut-off at 20 μm for all three cases, but the extinction coefficient for cut-off at 75 μm is much smaller than that for cut-off at 20 μm . Similar patterns are displayed for the associated normalized phase functions. The normalized phase functions for cut-off at 1 μm is virtually the same as those for cut-off at 20 μm for all three cases, but the normalized phase functions for cut-off at 75 μm is much smaller than those for cut-off at 20 μm . Thus, it is important to take into account the small crystal size distribution between 20 and 75 μm in the light scattering calculations.

We also examined the effects of variation in the small ice crystal number concentration on the single-scattering properties. We use the case 1 size distribution for this purpose. Figure 8 shows the log-log linearly extrapolated ice crystal size distribution. A log-log linear extrapolation was applied to the distribution based on the FSSP data. The symbol x denotes the number concentration corresponding to the mean ice crystal size (15 μm) determined from the FSSP data. The symbols y and z are the number concentrations at twice and half the value of x , respectively. The symbol s represents the number concentration for the particle size of 75 μm . Three extrapolation curves are subsequently obtained as the straight line segments linking s and x (mean), s and y (mean*2), and s and z (mean/2).

Table 4. The single-scattering parameters for the ice crystal size distributions depicted in Fig.6 at $\lambda=2.8\mu\text{m}$.

	case 1			case 2			case 3		
	cutoff at 1 μm	cutoff at 20 μm	HARP data	cutoff at 1 μm	cutoff at 20 μm	HARP data	cutoff at 1 μm	cutoff at 20 μm	HARP data
Extinction coefficient (km^{-1})	.54786	.53634	.28000	.57398	.56813	.35125	.97442	.95068	.51043
single- scattering albedo	.537072	.533364	.520451	.532743	.530831	.522517	.537135	.532992	.520385
asymmetry factor	.984868	.986460	.992222	.986606	.987450	.991421	.984932	.986683	.992289

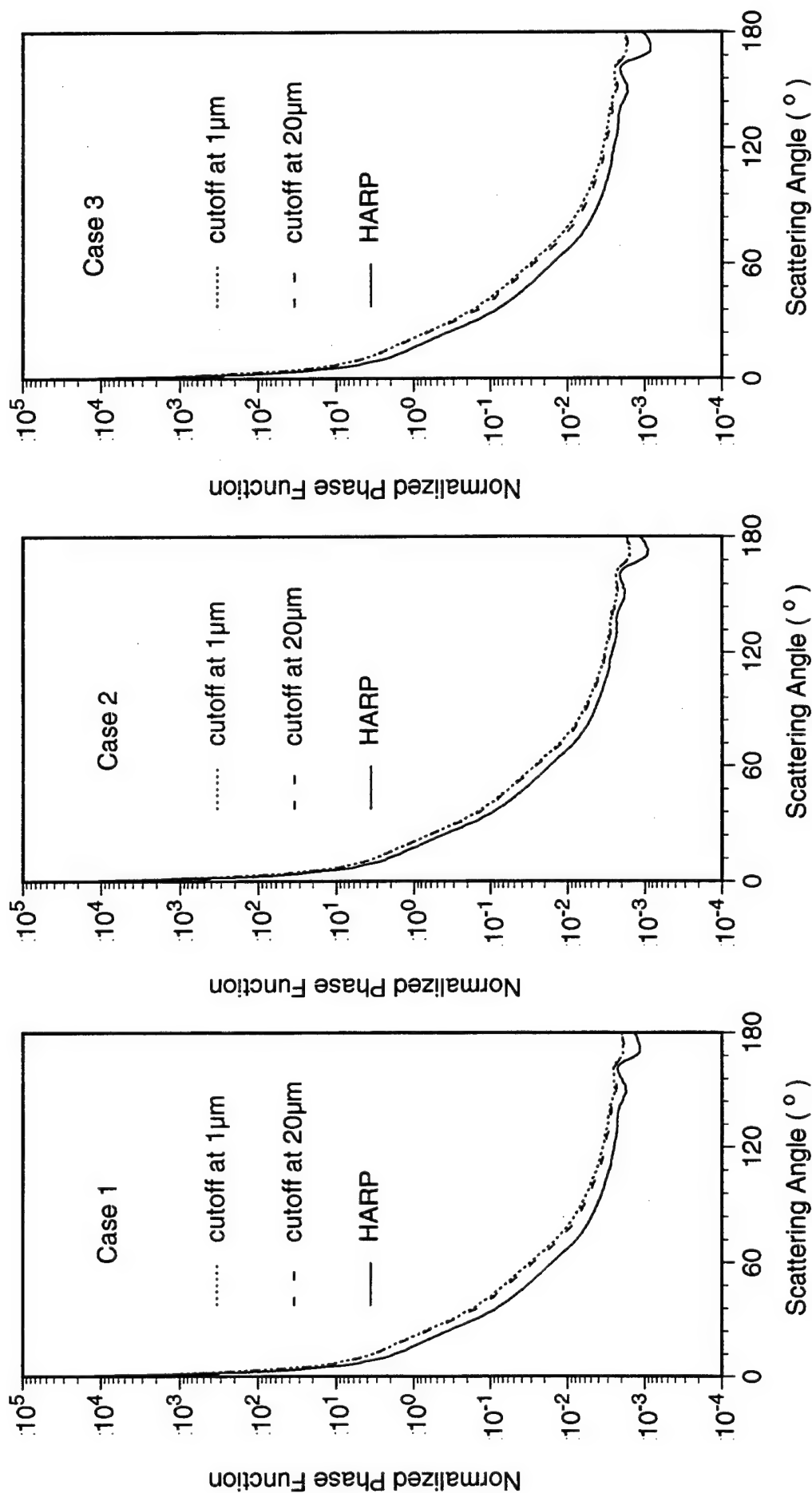


Figure 7 The normalized phase functions for the ice crystal size distributions given in Figure 6 at $\lambda=2.8\mu\text{m}$, computed from a modified ray-tracing method for randomly oriented hexagonal columns and plates.

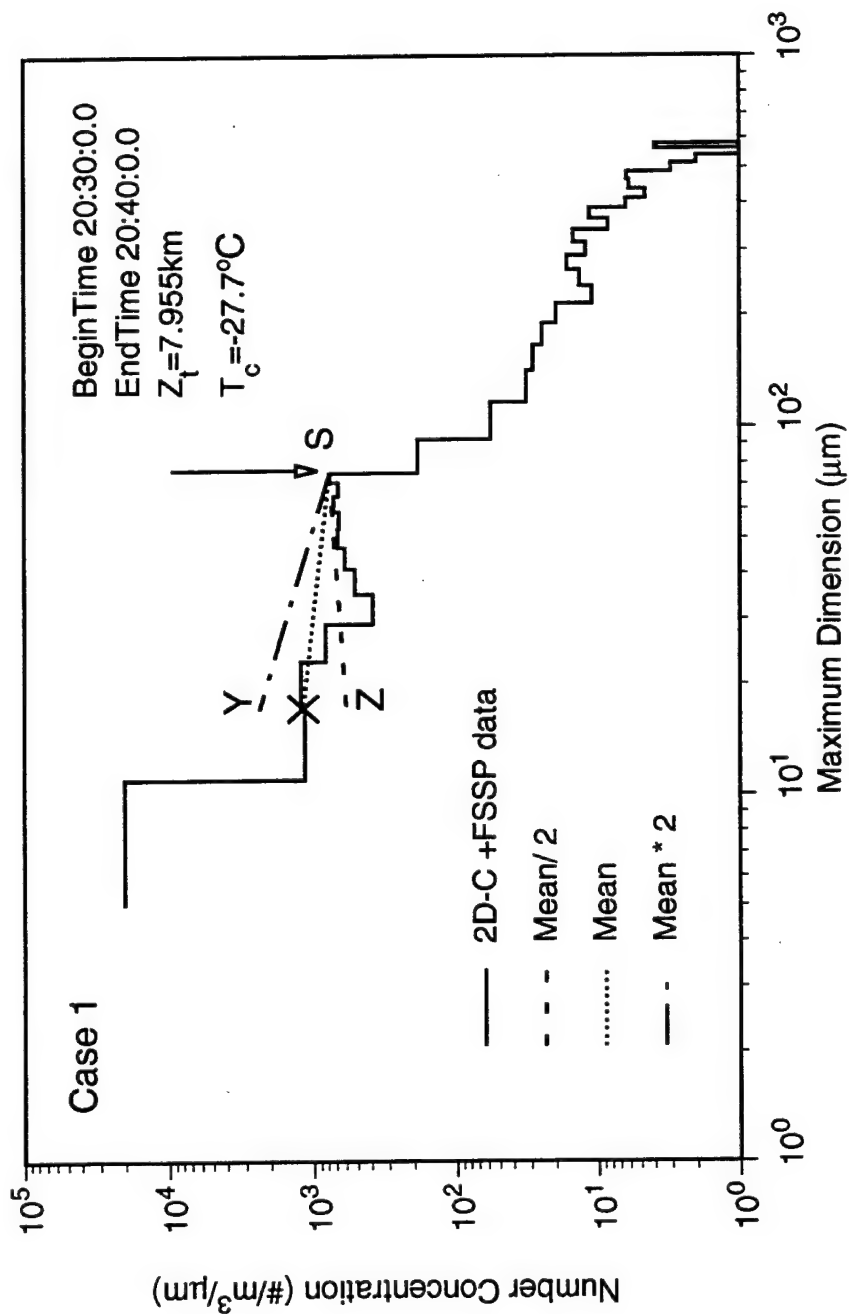


Figure 8 The ice crystal size distributions based on 2D-C and FSSP measurements during HARP mission flight on September 16, 1995 (Case 1). The lower limit of the 2D-C size distribution is $75 \mu\text{m}$. Three log-log linear extrapolations from $75 \mu\text{m}$ to $20 \mu\text{m}$ are displayed (see text).

Table 5 lists the single-scattering parameters at $2.8\ \mu\text{m}$ for the ice crystal size distributions obtained from the extrapolated values. Figure 9 shows the associated normalized phase function for the three extrapolated curves. Similar to the study of cut-off sizes, only the extinction coefficient is affected by the variation of small ice crystals. The single-scattering albedo, asymmetry factor, and the phase function do not vary significantly, however. From the preceding studies, we conclude that, to obtain a correct value for the extinction coefficient, it is necessary to include a reliable extrapolated ice crystal size distribution between 20 and $75\ \mu\text{m}$ in the light scattering calculations.

3. RETRIEVAL OF CIRRUS CLOUD PARAMETERS USING ARES 5.1-5.3 AND $3.7\ \mu\text{m}$ CHANNEL DATA

In this section, we present an airborne retrieval algorithm to infer cirrus cloud temperature, optical depth, and ice crystal mean effective size using the ARES IR spectrometer data. The retrieval method utilizes the $5.1\text{-}5.3\ \mu\text{m}$ water vapor band-wing radiances to compute cirrus cloud temperatures and IR emissivities, from which the associated optical depth is derived based on radiative transfer parameterizations. The ice crystal mean effective size is obtained by matching the computed sum of the $3.7\ \mu\text{m}$ solar reflected and IR emitted radiances with those from the ARES Ch. 42 ($3.755\ \mu\text{m}$) radiances. The selection of these channels is based on the examination of the computed weighting functions of a midlatitude summer atmosphere and the inspection of images of ARES channel radiances over the WB-57F flight tracks. We applied the retrieval algorithm to the ARES data collected during a mission flight, which was carried out on board the WB-57F on September 16, 1995 over the western Boston area. The retrieved cloud parameters are compared with the in-situ 2D-probe measurements made from the Aeromet's Learjet as well as cloud heights derived from ground-based 8.6-mm radar returns.

Cloudy radiances have been measured by the IR imaging spectrometer/radiometer on board the ARES Programs' WB-57F high-altitude research aircraft operated by the NASA Johnson Space Flight Center. The WB-57F is capable of reaching altitudes in excess of $60,000\ \text{ft}$, and carries a crew of two, permitting

Table 5. The single-scattering parameters for the ice crystal size distributions depicted in Figure 8 at $\lambda = 2.8 \mu\text{m}$.

	mean FSSP/2	mean FSSP	mean FSSP * 2
Extinction Coefficient (1/km)	0.407890	0.446238	0.522934
Single- scattering Albedo	0.526002	0.528148	0.531495
Asymmetry factor	0.985027	0.984543	0.983796

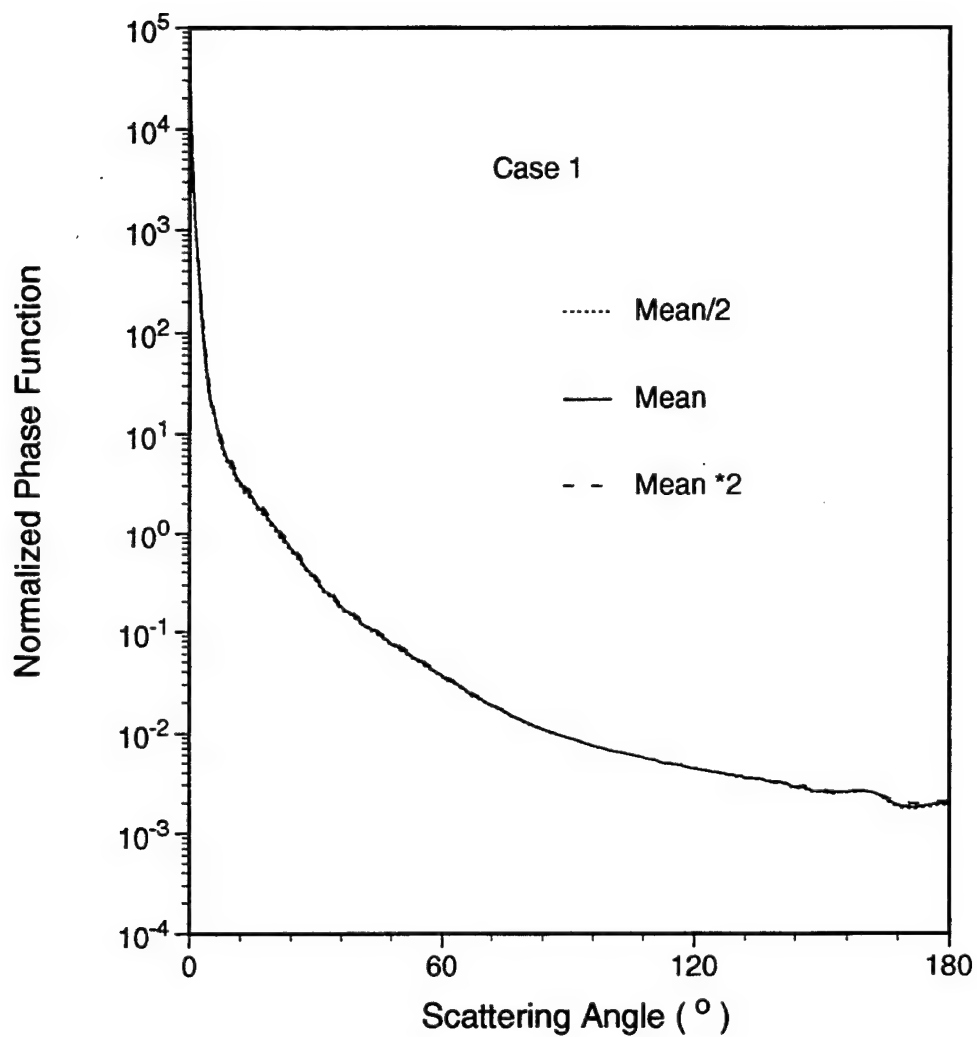


Figure 9 The normalized phase function for the randomly oriented ice columns and plates at $\lambda=2.8\mu\text{m}$. The ice crystal size distributions of ice crystals are depicted in Figure 8.

instrument operation by a dedicated flight crew. The sensor was mounted on the lower fuselage surface, with downward viewing while in level flight. The ARES sensor for the present study has been operated as a 75-channel imaging spectrometer. It is operated in a pushbroom mode with 45-pixel array pointing in the nadir direction taking data at the standard rates of 10, 20, 40, or 80 scans/sec. The optical elements of ARES provide a pixel IFOV of slightly more than 1 mrad, which corresponds to about 15 m ground resolution for a flight altitude of 15 km. The spacing of the ARES spectral wavelengths appears to depend on the optical arrangement with the channel band widths that vary between 0.02 and 0.07 μm .

For validation of the retrieved cloud temperature/height, we have obtained the cloud boundary height data from the collocated and coincident ground-based 8.6-mm TPQ-11 radar measurements. For comparison of the retrieved cloud optical depth and mean effective sizes with in-situ measurements, we have also acquired the meteorological and ice microphysical data collected from the High Altitude Reconnaissance Platform (HARP), which is a Learjet 36A, flying in conjunction with the ground-based radar and ARES measurements. The HARP carried instruments for taking both in-situ and remote atmospheric measurements. The in-situ instruments included FSSP, 1D-C and 2D-C probes for particle size distribution measurements. Ambient temperatures were measured by the Rosemount Total Temperature Sensor with an uncertainty of ± 1 K.

3.1 Principle of Retrieving Cirrus Temperature, Emissivity, and Ice Crystal Size Using ARES Channels

The present retrieval method for inferring cirrus temperature and emissivity is based on the numerical solution of the following set of algebraic equations (Liou et al. 1990; Ou et al. 1993, 1995) as follows:

$$R_i = (1 - \epsilon_i) R_{ai} + \epsilon_i B_i(T_c), \quad (1)$$

$$\epsilon_i = 1 - \exp(-k_i \tau), \quad (2)$$

where R_i is the upwelling radiances at the top of the cirrus cloudy atmosphere for the i th selected ARES channel; R_{ai} is the corresponding radiances reaching the cloud base for the i th channel; ϵ_i is the cloud IR emissivities, T_c is the mean cirrus temperature; $B_i(T_c)$ is the Planck intensities at T_c , τ is the visible optical depth and k_i is the effective extinction coefficient that has been determined from the calculated single-scattering

properties based on a number of measured ice crystal size distributions. The behavior of the cloud emissivity in terms of its dependence on wavelength and cloud parameters has been examined previously (Liou et al. 1990).

By straightforward algebraic manipulations, Eqs. (1) and (2) for a pair of channels ($i=1$ and 2) can be combined into a single equation in the form

$$\left[\frac{R_2 - B_2(T_c)}{R_{a2} - B_2(T_c)} \right] = \left[\frac{R_1 - B_1(T_c)}{R_{a1} - B_1(T_c)} \right]^{k_2/k_1} \quad (3)$$

If R_{a1} and R_{a2} are known, $B_2(T_c)$ and $B_1(T_c)$ are linearly correlated, and $k_2/k_1 \sim 1.0$, Eq. (3) becomes a linear equation. Numerical solution of linear equations is relatively straightforward and easy to program, as compared to the solution of nonlinear Eqs. (1)-(2).

The effective extinction coefficients for the retrieval channels have been computed using the adding/doubling program in conjunction with the development of this remote sensing algorithm. Eleven ice crystal size distributions from aircraft in-situ measurements have been chosen (Fu and Liou 1993). Their mean effective ice crystal sizes range between 23.9 and 123.6 μm . The single-scattering properties including phase functions, single scattering albedos, and extinction coefficients have been computed for each size distribution and for each of the selected ARES channels using the unified theory for light scattering by ice crystals. To optimize the computational effort, the forward-scattering peak of each phase function was truncated following the procedure developed by Takano and Liou (1989). Radiances for each channel and for a range of optical depths and ice crystal sizes were computed using the aforementioned adding/doubling program. The cirrus cloud emissivity, which is defined as the ratio of the the upwelling radiance to the cloud Planck function, was obtained as functions of the optical depth, mean effective size, and channel wavelengths. Finally, the effective extinction coefficients for each channel and for each size distribution was obtained as the slope of the linear fitting of $-\ln(1-\epsilon_i)$ vs. τ . Figure 10 shows the effective extinction coefficient (k -value) as a function of the mean effective size for eight wavelengths. For all wavelengths, the k -values increase with the mean effective

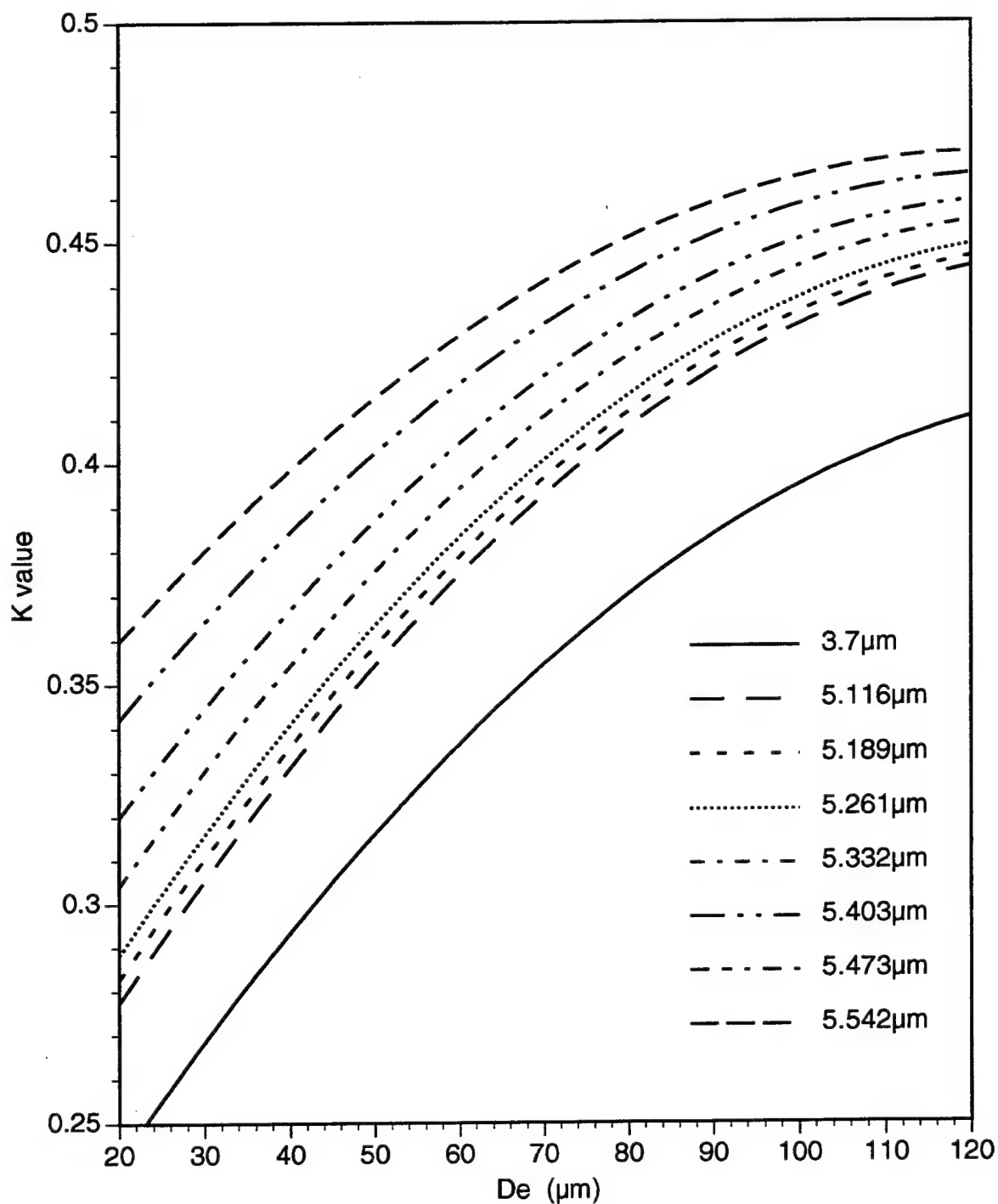


Figure 10 The k-value as a function of De for the retrieval channels. Eleven size distributions have been used for single-scattering computations. The single-scattering properties are used in an adding/doubling code to obtain the cloud emissivity.

size. This functional dependence of the k -values has been incorporated into the retrieval program. More importantly, the diagram shows that the values of the three pairs of k -ratios -- $k(5.189 \mu\text{m})/k(5.116 \mu\text{m})$, $k(5.261 \mu\text{m})/k(5.116 \mu\text{m})$, and $k(5.332 \mu\text{m})/k(5.116 \mu\text{m})$ --are all close to 1.0 for the range of the mean effective size considered here. This is one of the requirements for the linear correlation of pairs of ARES channel radiances.

In order to infer the cirrus emissivity, ϵ_i , and temperature, T_c , from multiple radiance measurements in cloudy conditions, the upwelling radiances at the cloud base, R_{ai} , must be known. In principle, it can be generated from forward radiation transfer calculations if the surface temperature, temperature and humidity profiles, and cloud base height are given. However, a more direct and reliable method to determine R_{ai} would be to find clear column radiances from the available data.

Assuming that the water vapor absorption/emission effects are negligible above cirrus clouds, we may approximate the cloud-base upwelling radiance using the measured clear radiance at the ARES flight level. This approximation has been applied to the retrieval of cirrus cloud parameters using AVHRR 3.7 and 10.9 μm window bands (Ou et al. 1993) and to the airborne cirrus retrieval using 6.5 and 10.5 μm radiometer data (Liou et al. 1990). Once R_{ai} is determined, Eqs. (1)-(2) can be solved by a numerical iteration method. Since there are two independent parameters, $N-1$ pairs of the N (> 1) channel data are used in the retrieval program. $N-1$ sets of the retrieved temperature and emissivity are then averaged to obtain their respective mean values.

Upon retrieval of the visible optical depth and the cloud temperature using thermal IR channels, we can obtain the mean effective size using the observed 3.7 μm channel radiances. We first assume a trial ice crystal size. The 3.7 μm thermal IR radiance can be calculated according to Eq. (1). The cloud-base upwelling 3.7 μm IR radiance can be obtained by converting the 4.75 μm clear-pixel radiance into its equivalent Planck function at 3.7 μm , since both channels are in the window spectral region. The 3.7 μm solar reflectance is determined from look-up tables, which are generated for the same six size distributions as described in Rao et al. (1995) and for appropriate solar-viewing geometries, using the adding/doubling method developed by

Takano and Liou (1989). Finally, the total $3.7\ \mu\text{m}$ radiance is calculated as the sum of the thermal IR and solar radiances. The radiance values thus obtained are subsequently compared with the observed $3.7\ \mu\text{m}$ radiances. The effective mean ice crystal size can then be obtained iteratively by adjusting the trial value based on the difference between the computed and observed radiances. Pixels having a retrieved mean effective size greater than $123.6\ \mu\text{m}$ or less than $23.9\ \mu\text{m}$ are discarded. Figure 11 gives a schematic flow diagram for the retrieval of cirrus cloud temperature, emissivity (optical depth) and mean ice crystal size.

3.2 Application of the Retrieval Scheme to ARES Data

The preceding cirrus cloud retrieval scheme is applied to the ARES spectrometer data obtained during a WB-57F flight that was launched on September 16, 1995. Data collected for Tracks 1, 3, 5, and 8 of that mission were analyzed. For Track 1, the WB-57F flew between 2055 and 2100 at a cruising altitude of 15 km along the southeast-northwest direction (Figure 12). The WB-57 flew directly over Hanscom Air Force Base (represented by the symbol "x"), where the ground-based 8.6-mm radar was located. During the period of Tracks 1 and 3, HARP was also flying below the WB-57F, although the two aircraft were not exactly collocated.

3.2.1 ARES Channel Spectral Properties

Adequate implementation of the retrieval scheme requires knowledge of the ARES channel spectral properties and the adequate selection of useful ARES channel data. Figure 13 presents the upwelling radiances associated with solar reflection and thermal emission in the $2\text{--}6.4\ \mu\text{m}$ region to assess the relative importance of the two radiation sources. For the solar reflection, we have used the updated solar irradiance data provided for our use by G. Anderson. The results are shown for the cosine of two solar zenith angles and for a surface reflection of 0.1. For the latter, Planck function curves for three temperatures covering the range of relevant earth's atmospheres are shown. It is clear that for $3\ \mu\text{m}$, the solar reflection is the primary contributor to radiation, while for $4.5\ \mu\text{m}$, the thermal IR emission is the predominant radiation source. Between these two wavelengths, the relative importance of the solar reflection and thermal IR emission is

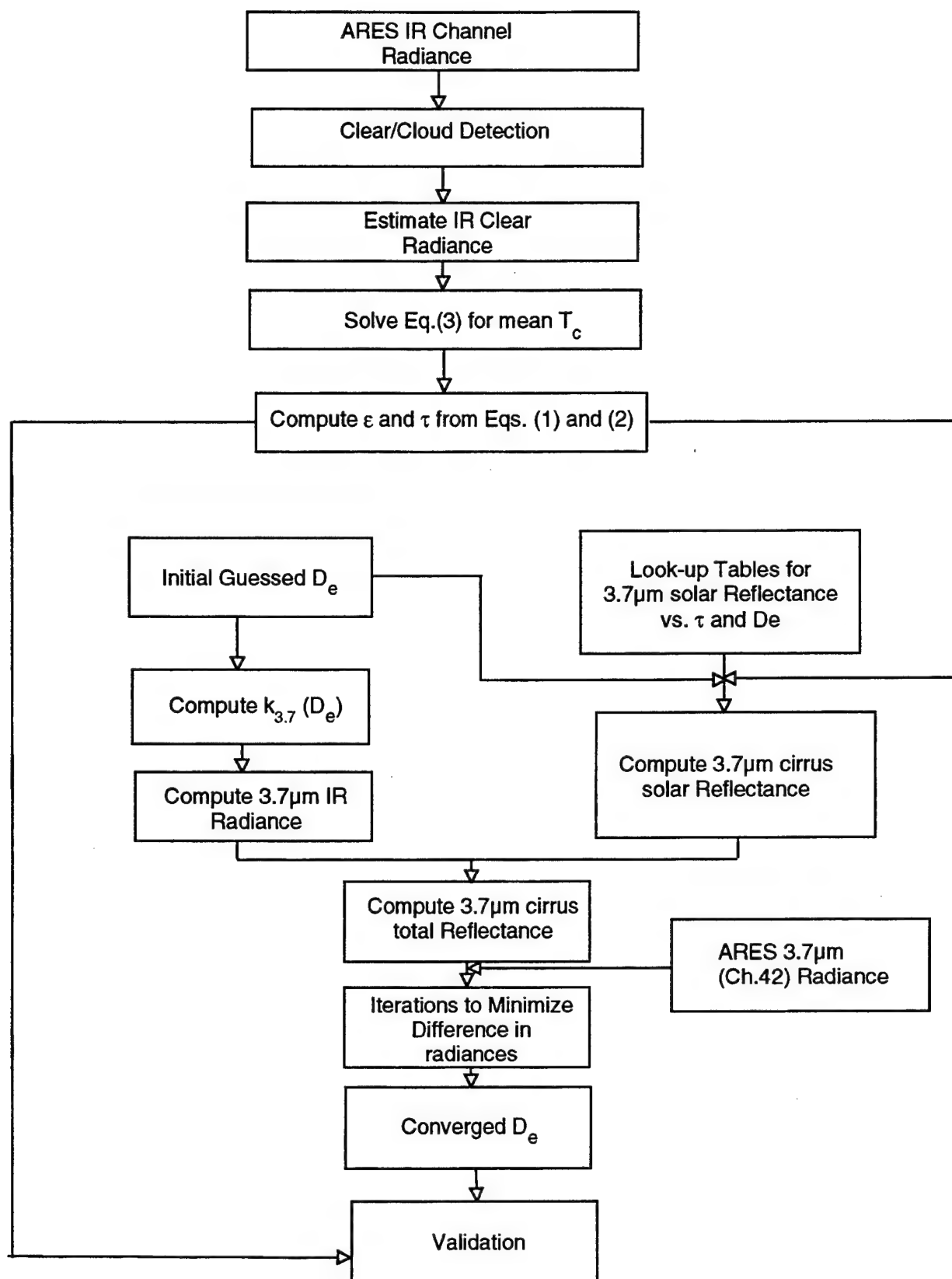


Figure 11 A schematic flow chart for the cirrus retrieval algorithm using ARES channel data.

TRACK1

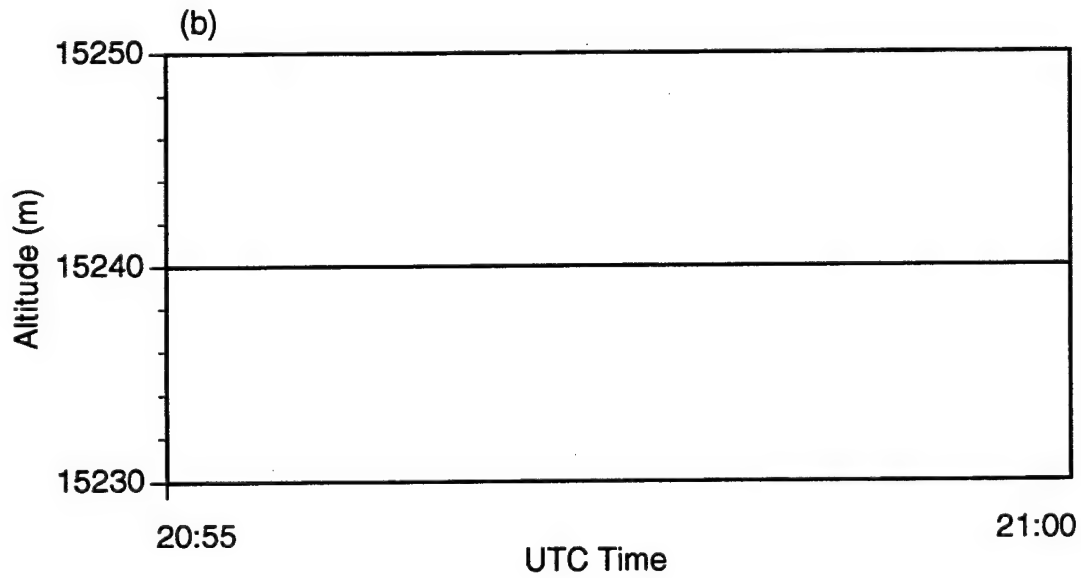
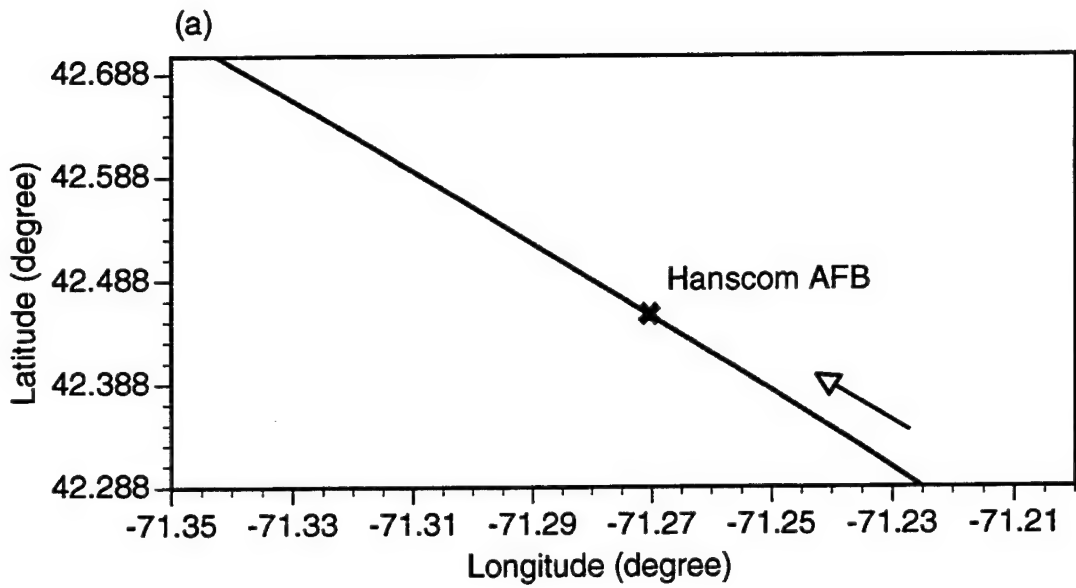


Figure 12 ARES flight track and altitude for Track 1 on September 16, 1995.

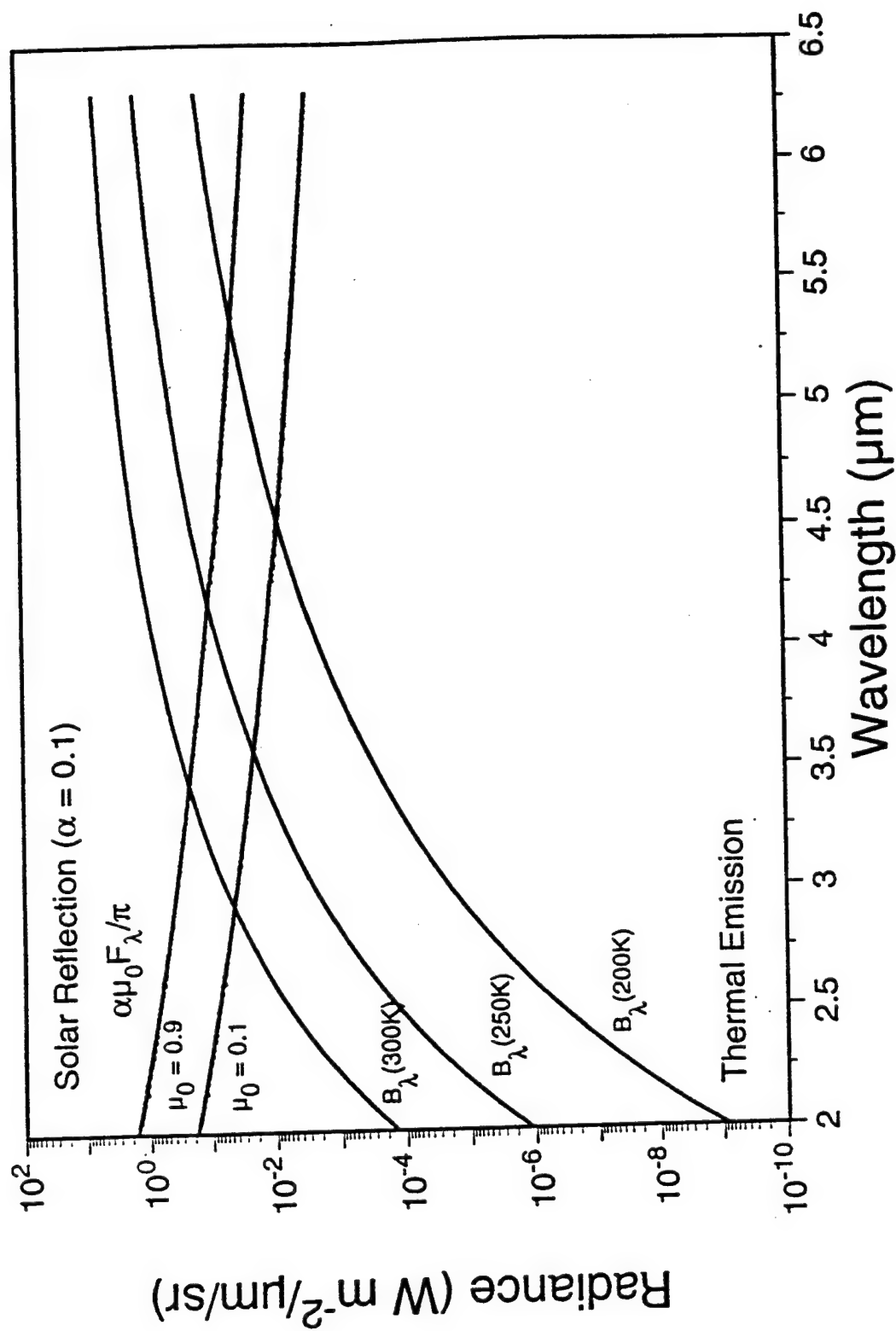


Figure 13 Upwelling radiances for solar reflection and thermal emission in the 2-6.5 μm region. F_λ denotes the solar irradiances, μ_0 is the cosine of solar zenith angle, α is the surface albedo, and B_λ is the Planck function.

dependent on the sun's position, the surface albedo, and the atmospheric thermodynamic state. For the radiative transfer simulation and the remote sensing algorithm development, both components must be accounted for in this intermediate spectral range.

In the 2-6.4 μm spectral region, several absorption bands exist. These include the 2.7 μm H_2O band produced by ν_1 and ν_2 fundamentals, the 3.2 μm H_2O band associated with $2\nu_2$, the 4.3 μm CO_2 due to ν_3 fundamental and P and R branches, and the H_2O 6.3 μm vibrational-rotational band. There are three windows located at the 2.2, 3.7, and 4.7 μm regions. The spacing of the ARES spectral wavelengths (wavenumbers) appears to depend on the optical arrangement, but 75 channels are available for cloud detection. Moreover, solar reflection contributes significantly to radiances for wavelengths shorter than 5 μm . Figure 14 shows a typical example of the ARES 75-channel spectra for clear and cloudy areas. Respective spectral regions for the absorption bands are noted in the diagram. Large measurement noises exist for Chs. 1-25 (1.9-2.7 μm), so that radiances for these channels are not useful. For Chs. 26-75, the aforementioned four absorption bands and two window bands are clearly displayed as local minima and maxima.

3.2.2 Selection of Retrieval Channels

To select a number of appropriate channels for the cirrus cloud retrieval, we have examined all the ARES channel weighting functions and images. Typical weighting functions were generated using the vertical transmittance profiles obtained from MODTRAN calculations employing a midlatitude summer temperature and humidity profiles. Figure 15 shows the weighting functions for all the 75 ARES channels. There are features that correspond to the distribution of absorption bands. Over the window band regions (2.2 μm , 3.75 μm , and 4.7 μm), the weighting function peaks at or near the surface. Over the band center of the 2.7 μm H_2O , 4.3 μm CO_2 , and 6.3 μm H_2O absorption bands, the weighting function peaks in the upper atmosphere. Over the band wing regions, the weighting function peaks at intermediate levels. These physical properties are the basis for the selection of retrieval channels. In principle, it is most ideal to choose channels with the weighting functions peaking in the lower atmosphere. For channels with the weighting functions peaking in the upper

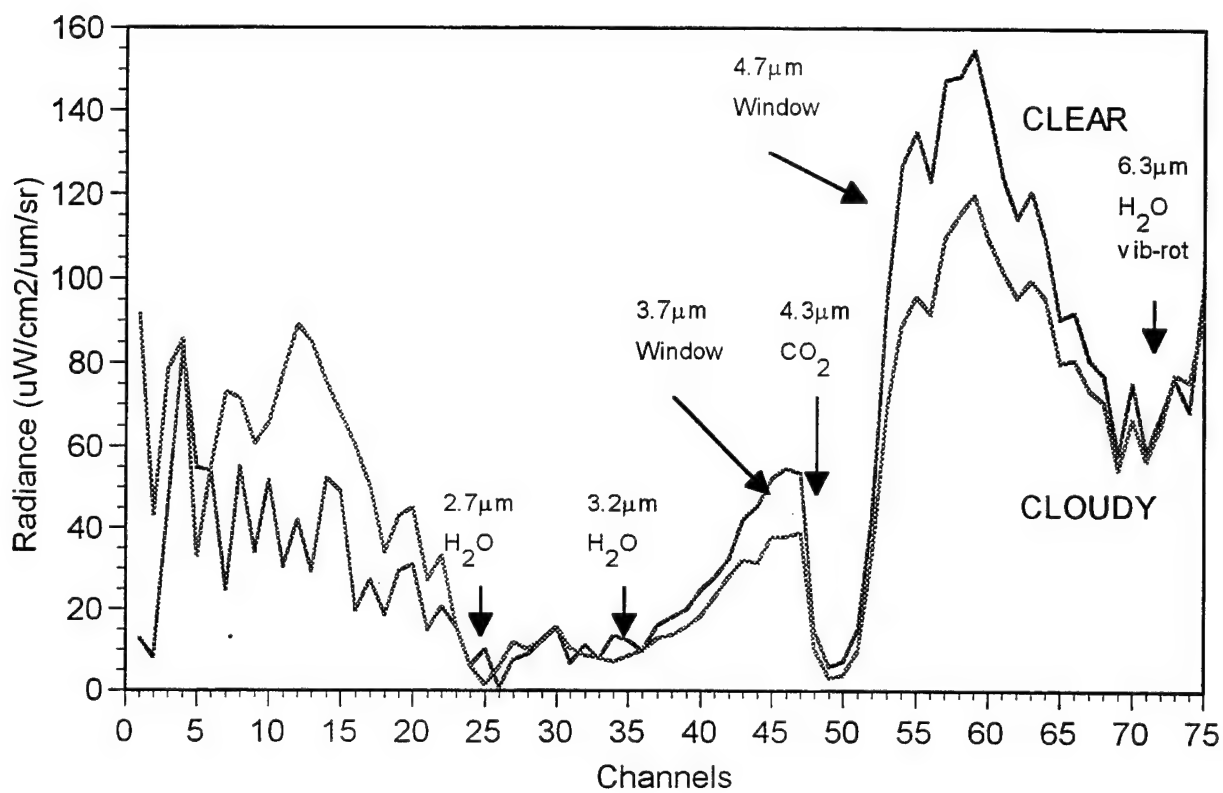


Figure 14 Typical example of the ARES 75-channel spectra for clear and cloudy areas.

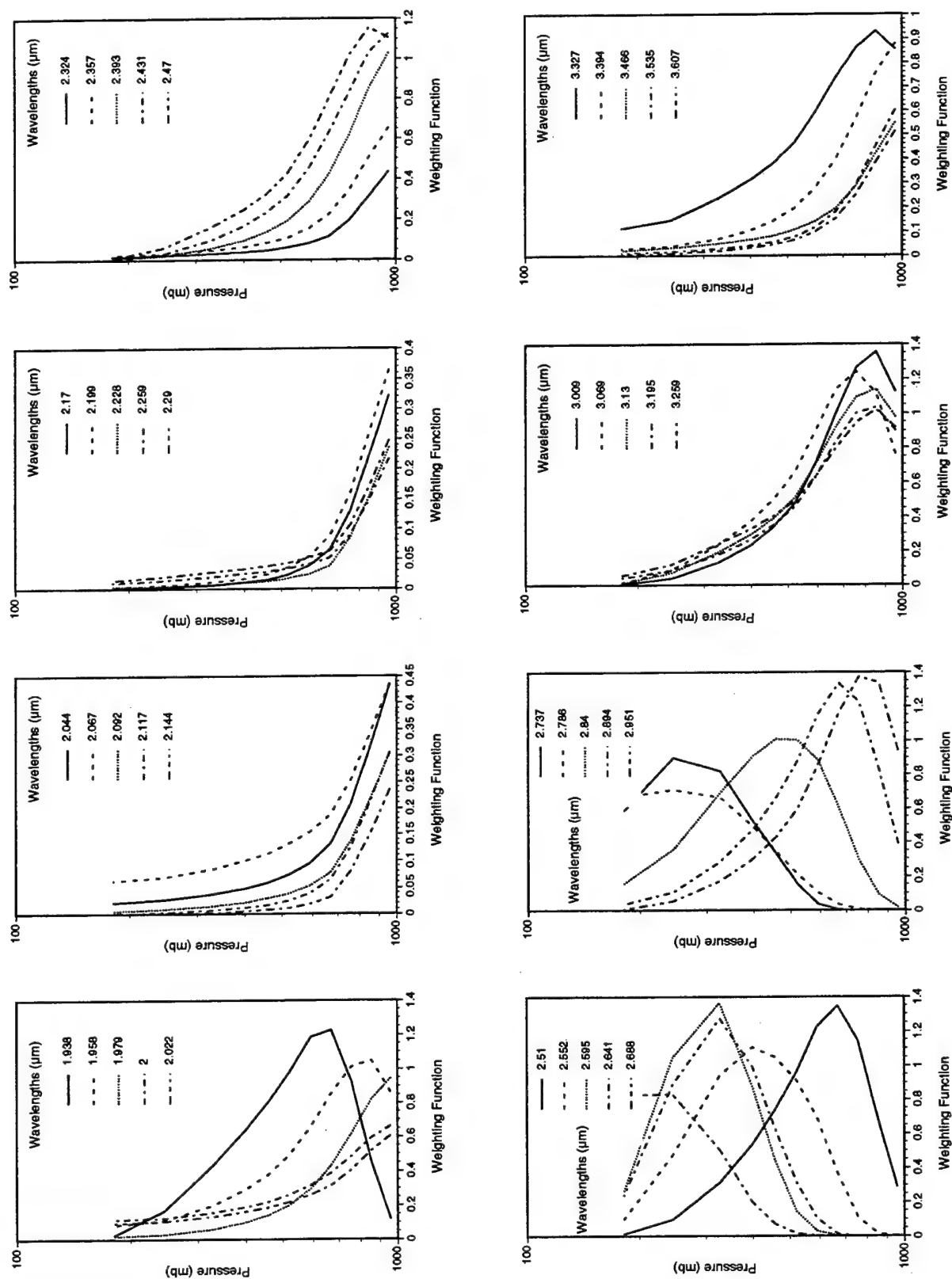


Figure 15 Weighting functions for the mid-latitude summer atmosphere and for the ARES 75-channel spectral wavelengths.

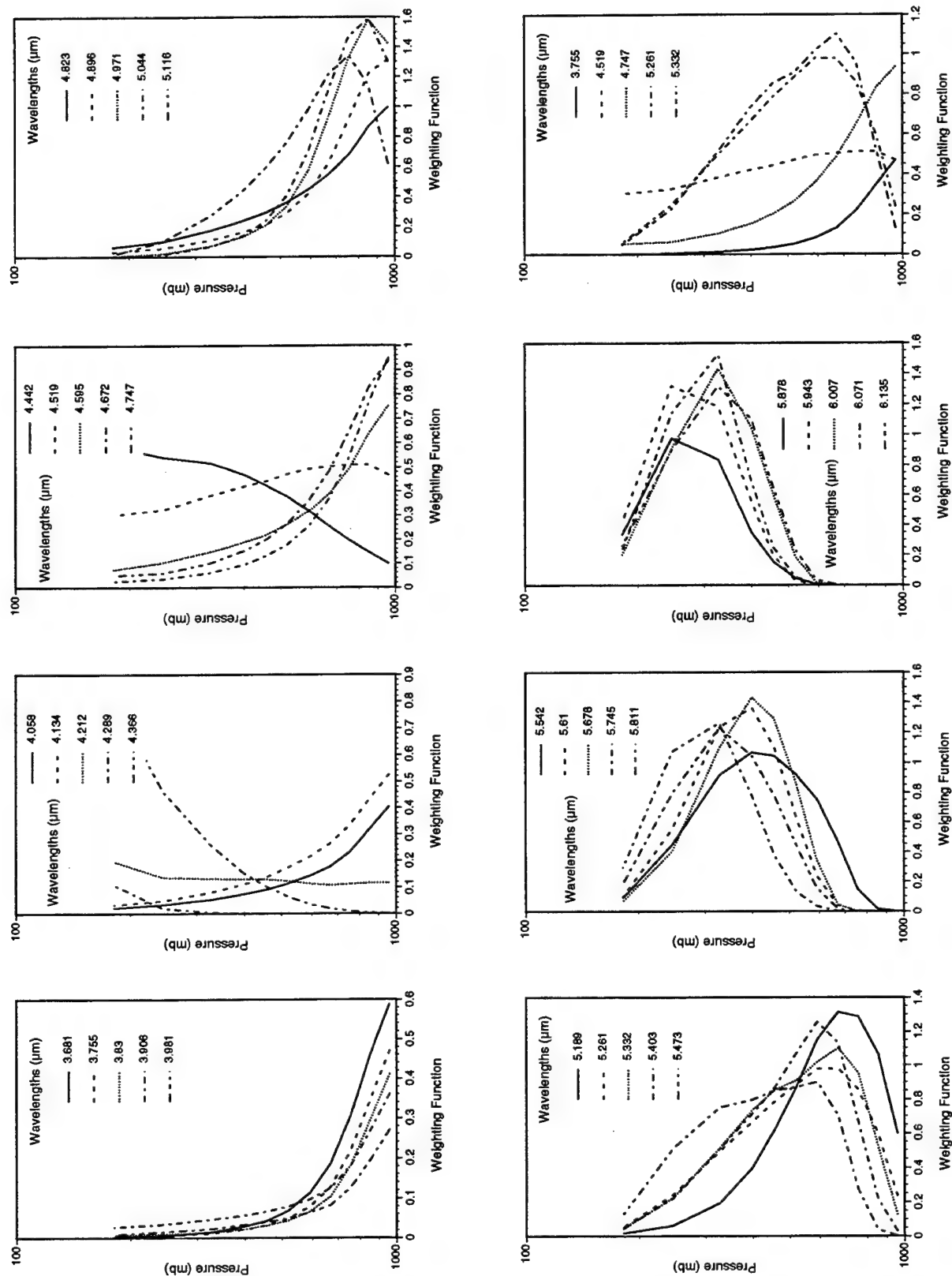


Figure 15 Continued.

atmosphere, the radiances tend to be dominated by gaseous emission from the upper atmosphere, thus suppressing the cloud signals. On the other hand, for channels with the weighting functions peaking at the surface, inhomogeneity can cause a large spread in clear radiances and thus lead to inaccurate cloud retrieval results.

Moreover, we can also use radiance images to facilitate the selection of channels. We have acquired from SCITEC two CDROMs containing the ARES data 16-9-95-1A, the quick-look software ADAPT from SCITEC which allows us to display graphically the large volume of the ARES-SSDS dataset on SGI, and the decoding software "hdc2bip" which enables us to decode the compressed data set. Using ADAPT, we were able to scan the image of the entire flight track for each ARES channel, and to select a scene which displays a distinct contrast between high (clear) and low (cloudy) radiance areas. Figure 16 shows the radiance images for Chs. 41(3.681 μm), 42(3.755 μm), 55(4.747 μm), 60(5.116 μm), and 63(5.332 μm) over the selected scene. The first three channels are within the 3.75 μm and 4.7 μm window regions, while the last two channels are in the 6.3 μm water vapor band-wing region. For each image, the horizontal and vertical scales are ~ 500 m and ~ 2.5 km, respectively.

From these images, it is noted that the upper 1/3 of the domain is clear, while the rest of the domain is cloudy. Over the clear area, the images for the three window channels show significant variations of the emitted/ reflected radiances due to the inhomogeneity of the surface temperature and emissivity. However, for the two band-wing channels, radiances over the clear area appear to be relatively uniform, as compared to the clear radiances for the window channels, because the significant water vapor absorption/emission effect in the lower troposphere blocks the horizontally inhomogeneous surface emission. The narrow distribution of the clear radiances is a desirable feature for application of the remote sensing algorithm. A smaller spread in clear radiances would lead to less errors in prescribing the mean clear radiances, thus increasing the retrieval accuracy (Rao et al. 1995).

Over the cloudy area, it is evident that the image for the 4.7 μm channel, as well as the images for the

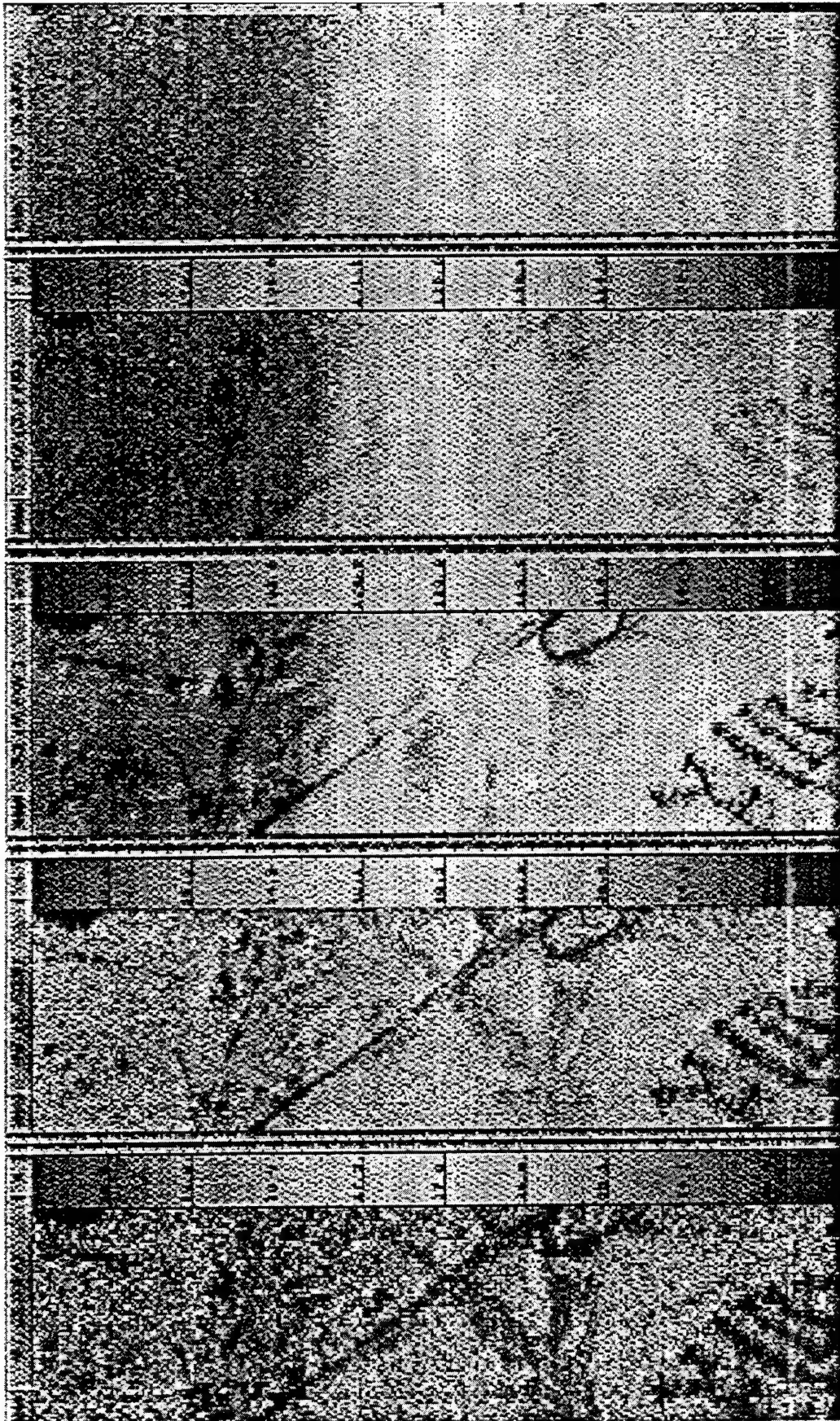


Figure 16 Radiance images for ARES channels 41, 42, 55, 60, and 63 over a selected scene with strong cloud/clear contrast within the Track 1 of September 16 flight.

two band-wing channels, contain distinct cloud signatures. For the two $3.7\ \mu\text{m}$ window channels, there is no distinguishable cloud signature due to the compensating effects of strong reflection and weak emission by cloud particles. Radiance images for channels at the absorption band center (not shown here) exhibit no cloud signature. Based on the images shown in Figure 16, together with the weighting function profiles shown in Figure 15, we select Ch. 60, 61 ($5.189\ \mu\text{m}$), 62 ($5.261\ \mu\text{m}$) and 63 for the development of a cirrus cloud retrieval algorithm. Images for these channels contain definitive cloud signatures and display narrow data spread of clear radiances.

3.2.3 Determination of Mean Clear Radiances

To retrieve the cloud temperature and emissivity, the mean clear radiance for each channel within the selected domain must be known. Thus, a clear/cloud detection scheme was developed to identify clear data points. It is based on the physical properties of the ARES equivalent brightness temperatures for selected channels. In this scheme, clear pixels are separated from the cloudy pixels by applying the threshold tests to the equivalent brightness temperature data for all selected channels. If the equivalent brightness temperatures for given pixels are greater than the prescribed threshold values for all selected channels, then those pixels are categorized as clear. Otherwise, the pixel is flagged as cloudy. A schematic flow diagram depicting the clear/cloudy detection scheme is given in Figure 17. The number of cloudy pixels may be overestimated in this scheme. However, by doing so, we can ensure that the detected clear pixels are truly clear pixels, and that any cloudy pixels will not be missed when the retrieval is carried out.

The mean clear radiance for each channel is determined based on the average of radiances of all detected clear pixels within the selected scene ($\sim 10\ \text{km}$ strip). To determine the appropriate threshold values for all selected channels, we perform statistical analyses on the radiance data over the domain of Figure 16 that has distinct clear-cloud contrast. Figures 18(a)-(d) show the histograms of the brightness temperatures for Chs. 60-63 within the domain of Figure 16. Each histogram displays a distinct bi-modal shape. The high- and low-radiance modes represent the mean radiances for the clear and cloudy conditions, respectively. Because these

Clear/Cloud Detection Scheme

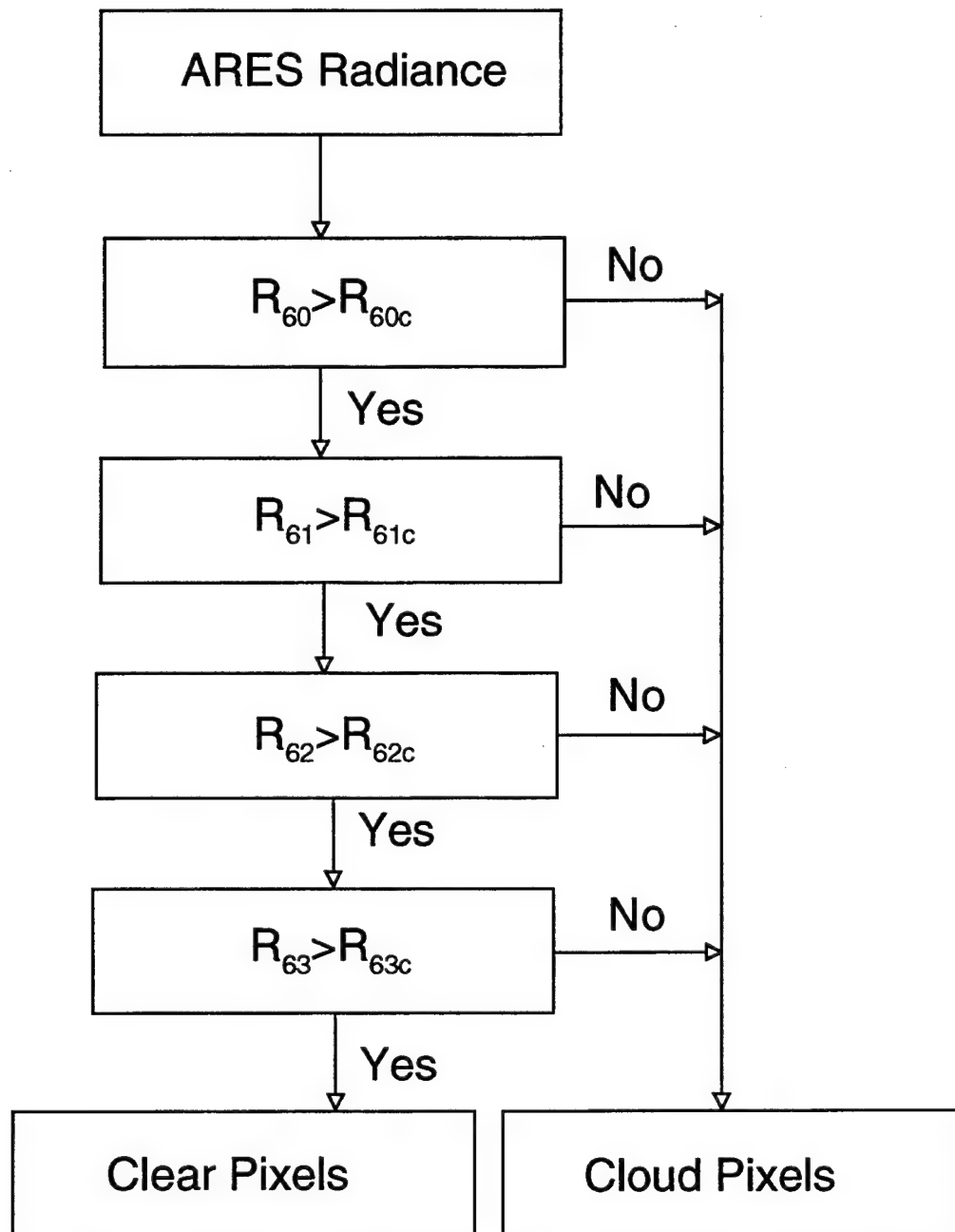


Figure 17 Schematic flow diagram depicting the clear/cloud detection scheme.

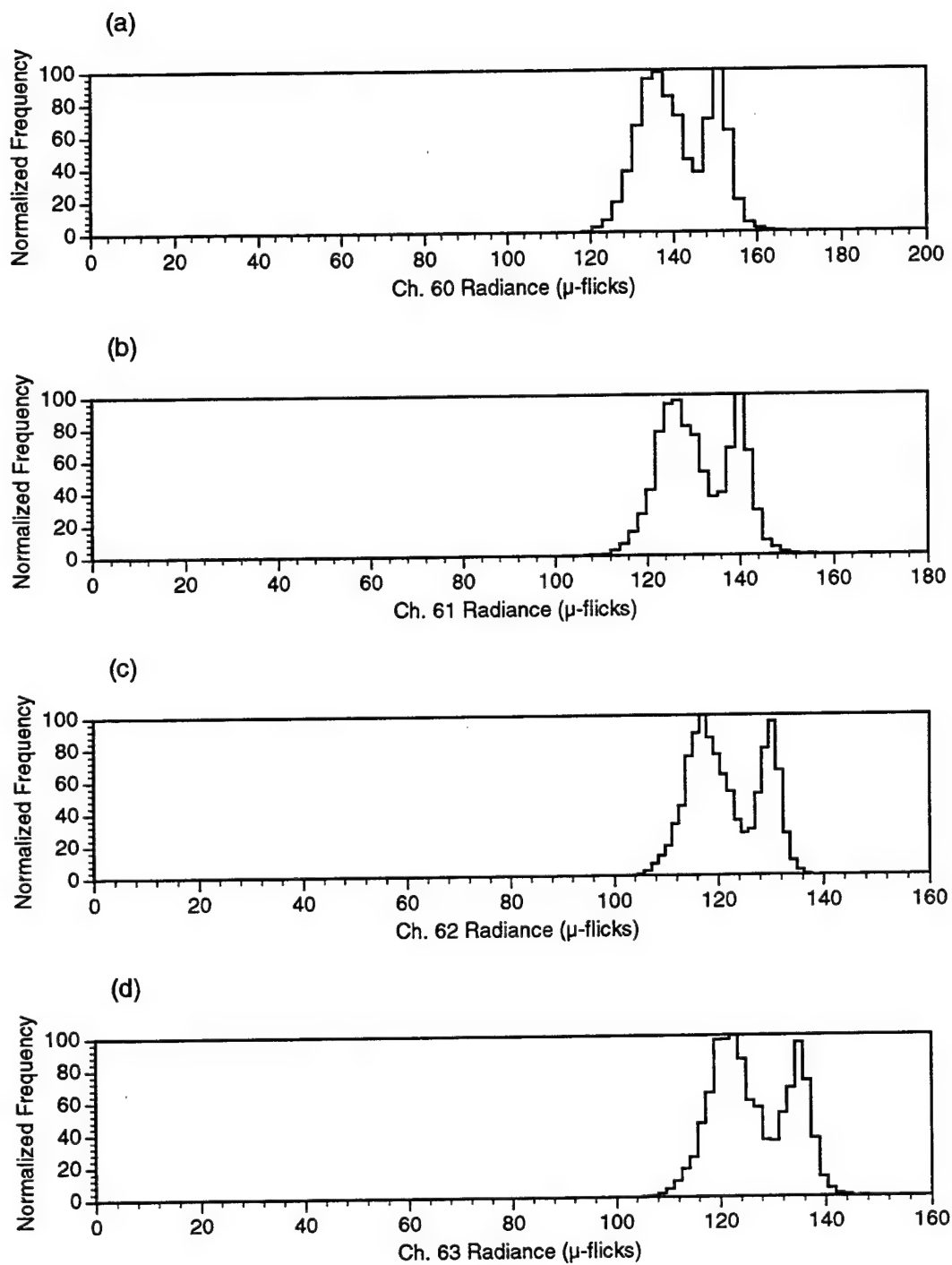


Figure 18 Histograms of brightness temperatures for ARES Chs. 60-63 within the domain of Figure 16.

modes are so distinct, the threshold value for each channel can be easily determined as the radiance that is associated with the minimum frequency between the two modes. Figures 19(a)-(e) show the clear (black) and the cloudy (white) pixels detected by individual and combined threshold tests. For Chs. 60 and 61, because of their rather transparent nature, certain pixels with higher brightness temperatures are identified as "clear". However, these "clear" pixels are not detected by the other two channels. For this reason, the combined threshold tests detect more cloudy pixels than those determined from individual channels.

3.2.4 Application of the Retrieval Scheme to ARES Channel Data

Before application of the retrieval scheme to the ARES channel data, it would be interesting to examine whether the ARES IR channel data show characteristics of linearity in the two-channel radiance correlation [Eq. (3)], and to determine whether the ARES 3.7 μm channel data fall within the range of the computed values so that these data can be used for the retrieval of ice crystal mean effective sizes. Figure 20 shows examples of the scatter diagram for three pairs of ARES channels : 61-60, 62-60, and 63-60. In each frame, the straight line denotes the correlation of Planck functions for the two channels, and the dots are radiance data points chosen from the ARES data collected during the September 16, 1995, mission flight over the Hanscom Air Force Base area, where a strong contrast of clear and cloudy regions was present at the flight time (see Section 3.2.2). The clustering of radiance data points shows a distinctive straight-line pattern. Basically, there are two clusters in each frame. The upper cluster corresponds to clear data points, while the lower longer clusters are associated with cloudy radiances.

Figure 21 shows an example of the retrieval of ice crystal mean effective sizes using the ARES 3.7 μm channel data. In the upper panel, the computed 3.7 μm solar radiances are plotted as functions of optical depth and six mean sizes. For $\tau > 2$, these radiances are not sensitive to the optical depth, but are quite sensitive to the ice crystal size distribution. In the middle panel, the computed 3.7 μm IR radiances for different sizes are plotted against the optical depth. In this case, the cloud temperature is 250 K and the clear brightness temperature is 291 K. The 3.7 μm IR radiances decrease with increasing optical depth and mean effective size.

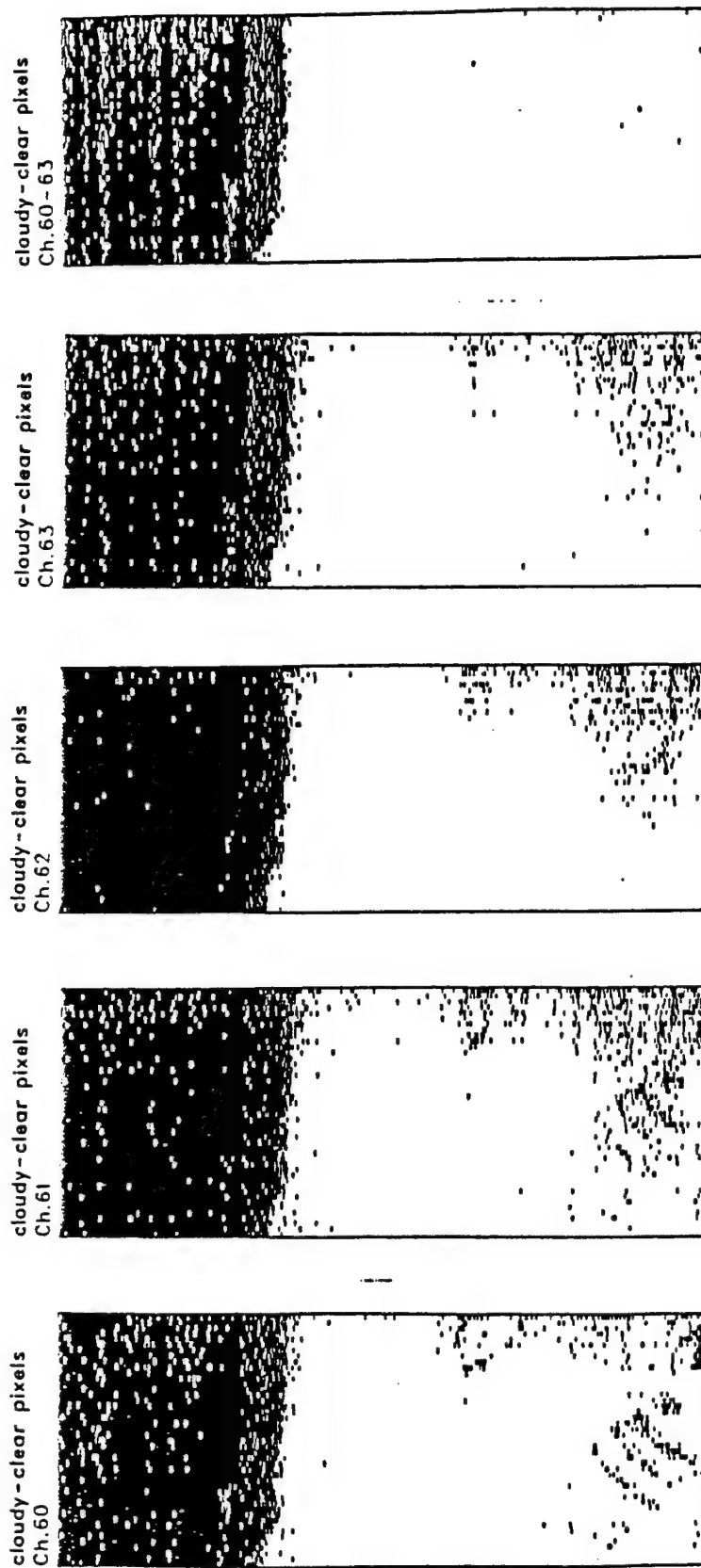


Figure 19 Clear (black) and cloudy (white) pixels detected by individual and combined threshold tests within the domain of Figure 16.

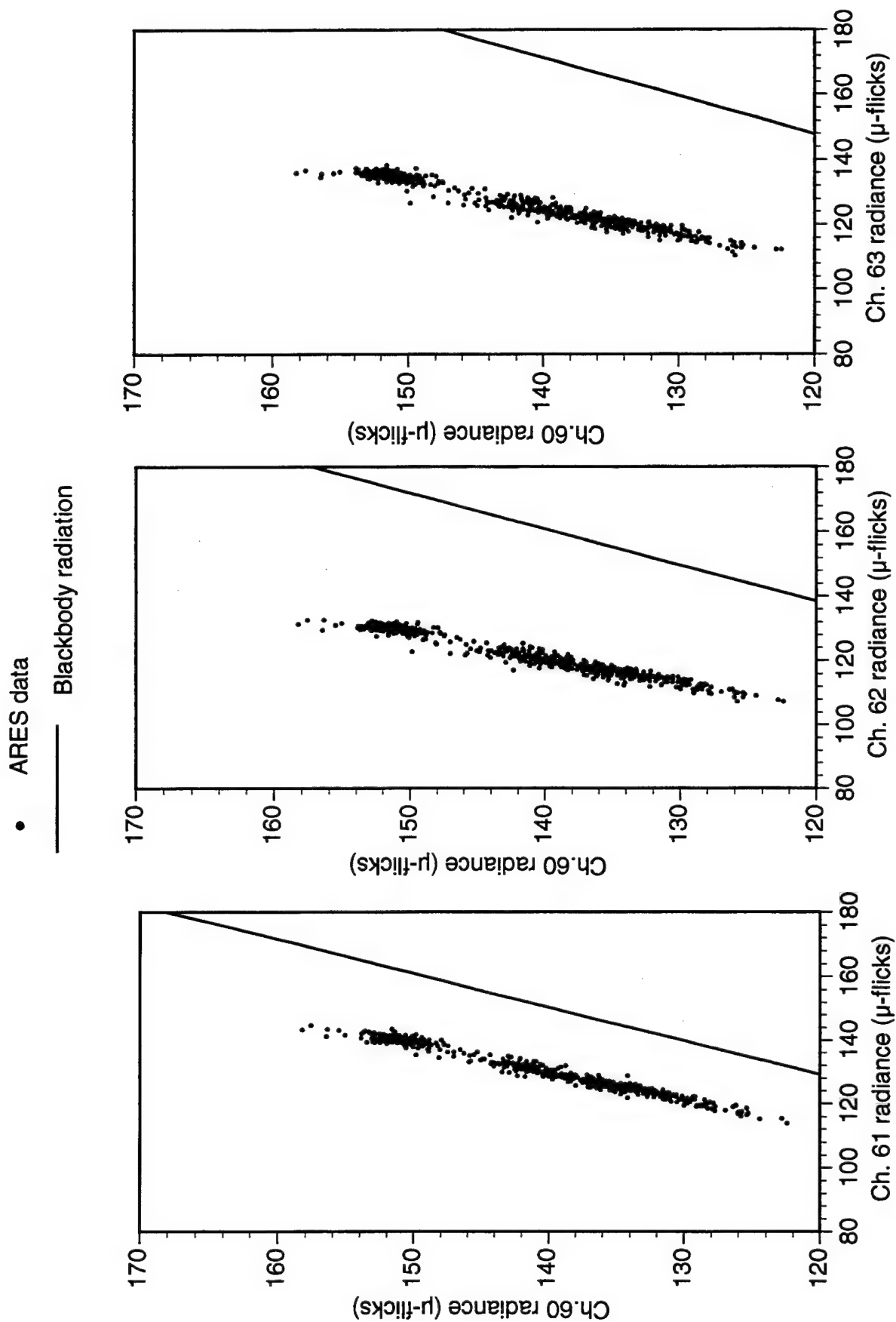


Figure 20 Examples of scatter diagram for three pairs of ARES channels: 60-61, 60-62, and 60-63.

COMPUTED SOLAR/IR/TOTAL RADIANCES FOR ARES CHANNEL 42

(a) Flt. 091695 TRACK3

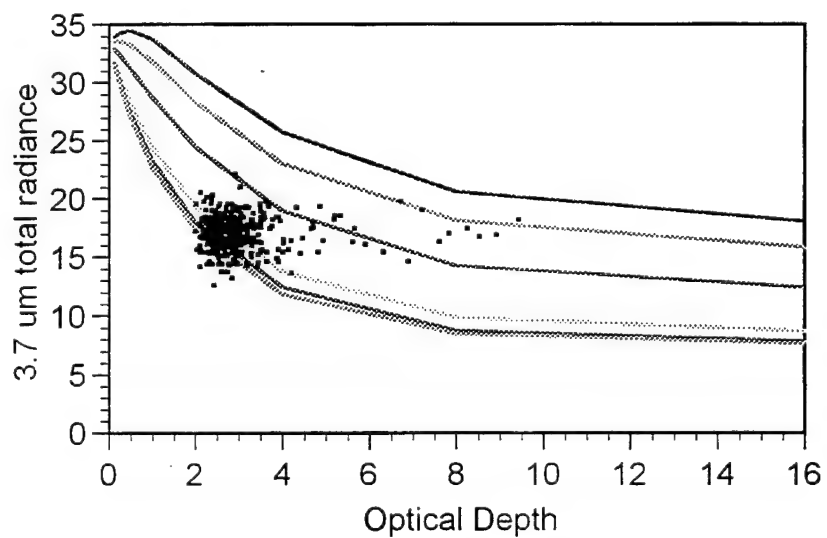
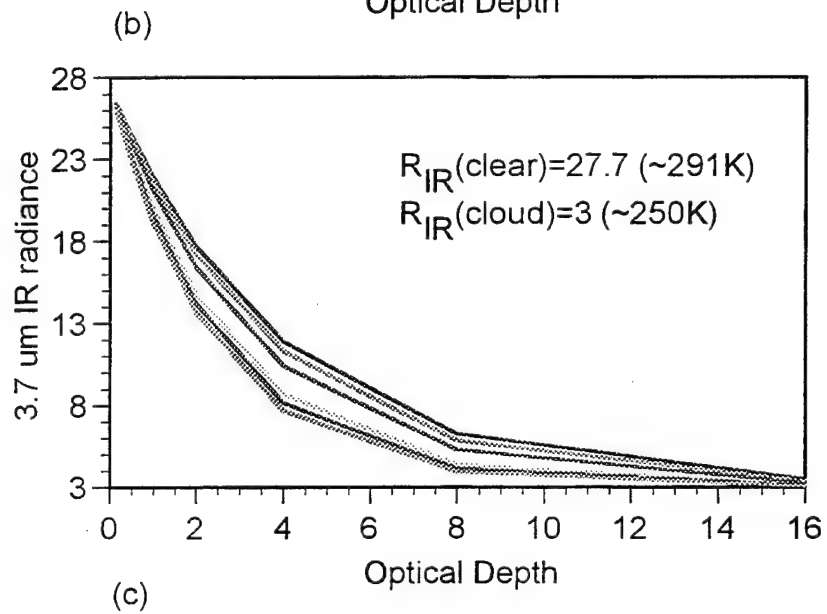
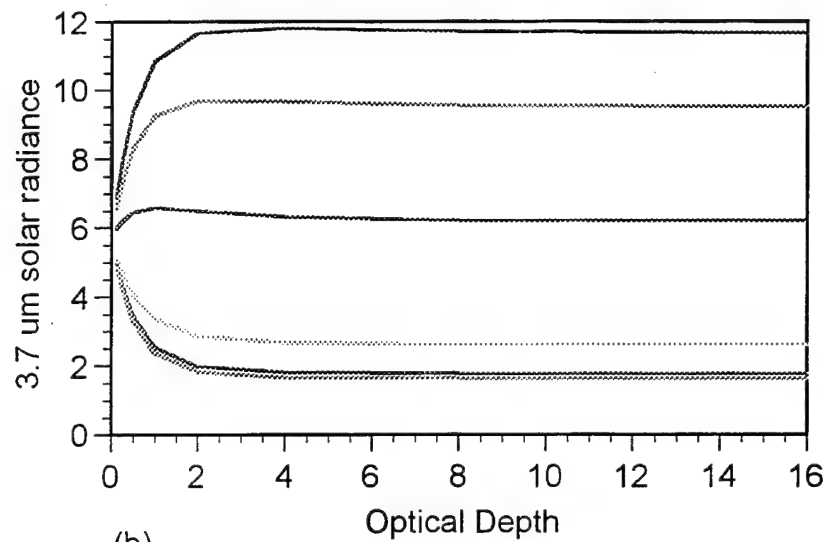


Figure 21 Computed 3.7 μm solar radiances (a), IR radiances (b), and total radiances (c) as functions of optical depth and ice crystal size.

Finally, in the lower panel, the $3.7\ \mu\text{m}$ total radiances are plotted against the optical depth. It is noted that these radiances are sensitive to both the optical depth and ice crystal size. We display the ARES measured data collected during Track 3 of the September 16 flight on the lower diagram and show that they lie within the bulk range of the computed curves, indicating that it is feasible to use the ARES measured data to retrieve ice mean effective sizes.

Applying the retrieval scheme to the detected cloudy-pixel radiance data of the selected ARES channels, we can determine the cirrus cloud temperatures, emissivities (optical depth), and ice crystal sizes for the four flight tracks of September 16, 1995. For the purpose of displaying data, we obtain the array-averaged channel equivalent brightness temperatures and the retrieved parameters for each scan within the flight track. Variation of the computed array-averaged Ch. 60 equivalent brightness temperatures, cloud temperatures, and optical depths for the four flight tracks, the mean effective sizes for Tracks 1 and 3, and the cloud emissivities for Tracks 5 and 8 along the flight path are shown in Figures 22-25. The results shown in these figures are based on the application of the retrieval scheme for 4 to ~ 10 scans of the 45-pixel array data. However, by using an efficient numerical scheme, the total run time on a powerful state-of-the-art SGI is less than 10 min for each track. Retrieval of the mean effective size was not performed for Tracks 5 and 8, because these tracks were flown after nightfall and the $3.7\ \mu\text{m}$ radiances are dominated by the thermal IR component, which is less sensitive to the ice crystal size than the solar component. For Track 1, there are three intervals which have been identified as clear (16-20 km, 25-28 km and 30-32 km). For Track 3, one clear period is identified between 16 and 20 km. Tracks 5 and 8 show no clear periods. The retrieved cloud temperatures vary between 230 and 255 K. The retrieved cloud optical depths are 0-2, 0-4, 1.6-7, and 1.2-7.2 for the four tracks. The retrieved mean effective ice crystal sizes for Tracks 1 and 3 are generally between 25 and $75\ \mu\text{m}$. Based on these retrieval results, the cirrus under study was relatively warm and was composed of small ice crystals. The cirrus clouds for Tracks 1 and 3 were optically thin, but they became thicker during the last two flight tracks. The reliability of the retrieved results is partially confirmed by the following validation efforts.

ARES Flt. 091695 TRACK 1

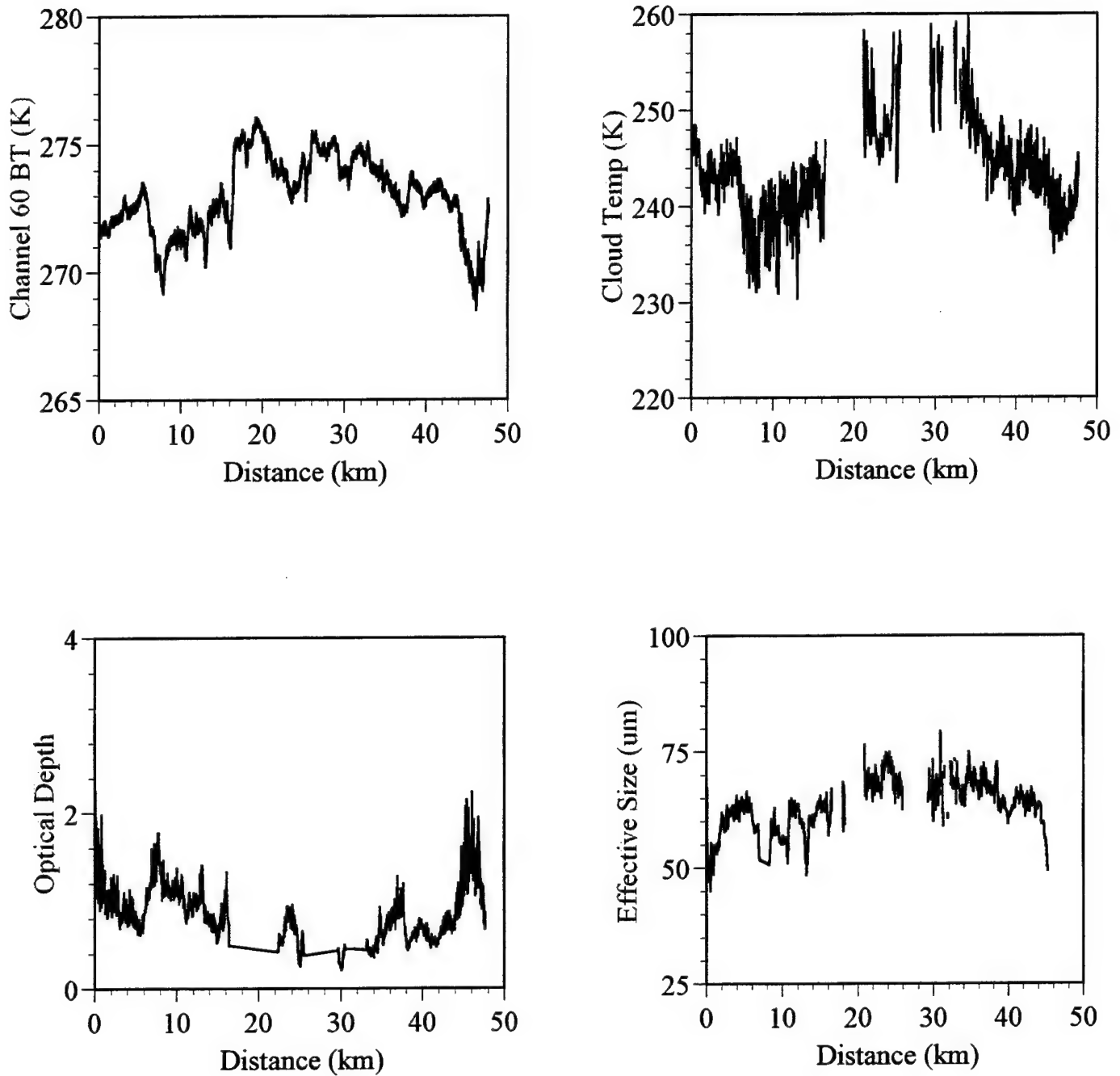


Figure 22 Array averaged channel equivalent brightness temperatures, retrieved cloud temperature, cloud optical depth, and effective size as functions of flight distance for Track 1, 9/16/95.

ARES Flt. 091695 TRACK 3

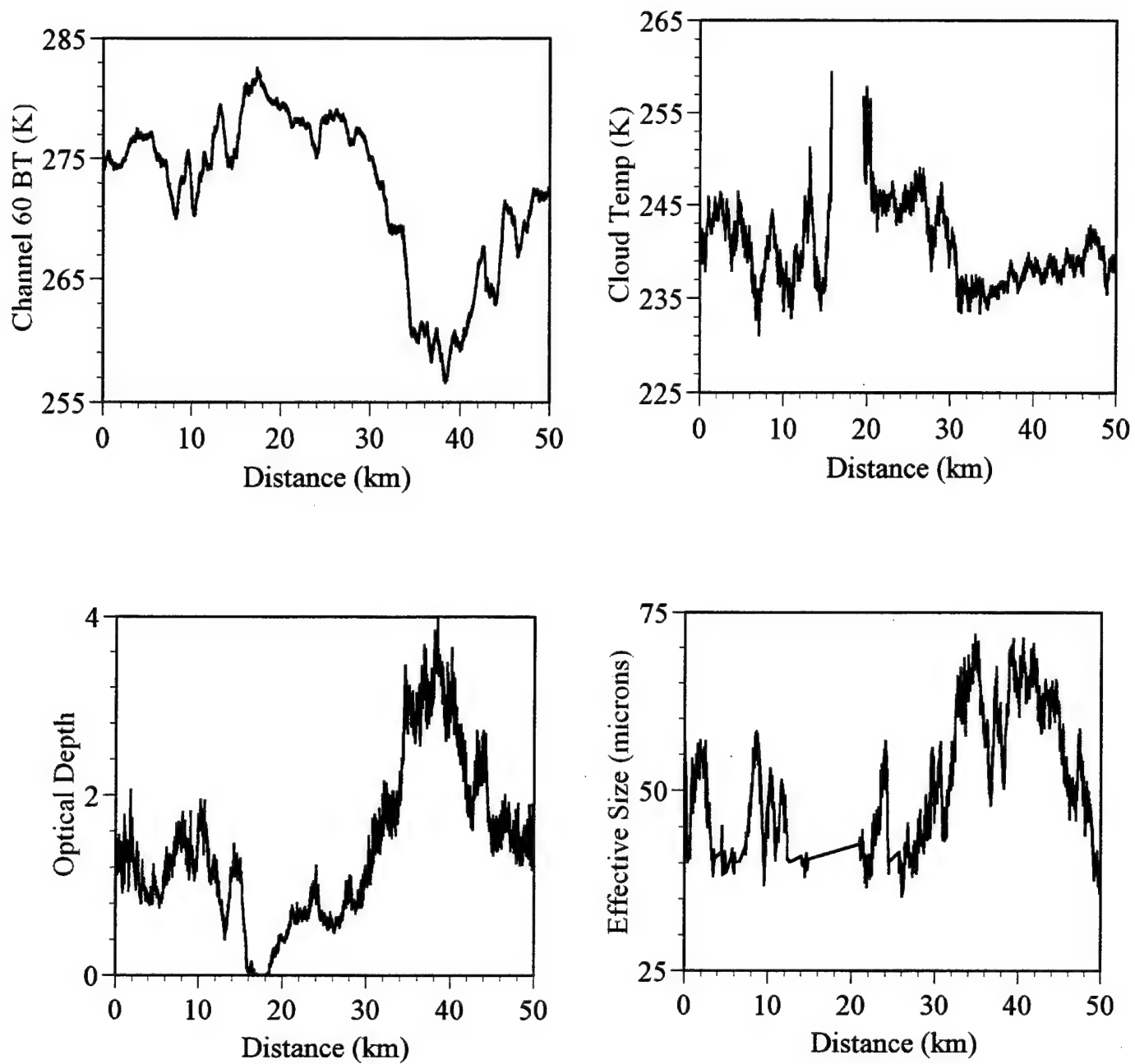


Figure 23 Same as Figure 22, except for Track 3, 9/16/95

ARES Flt. 091695 TRACK 5

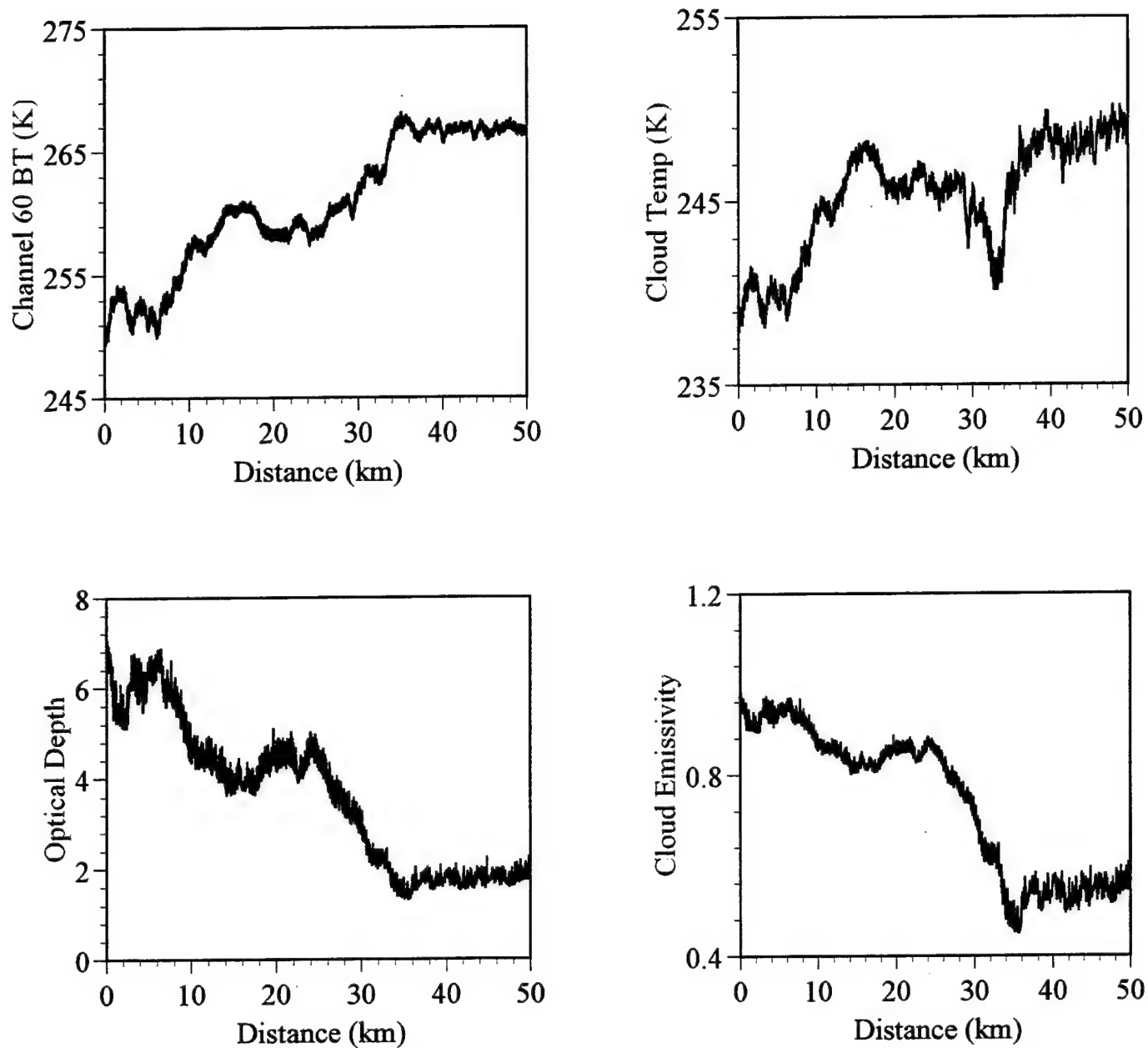


Figure 24 Same as Figure 22, except for Track 3, 9/16/95, with effective size replaced by cloud emissivity.

ARES Flt. 091695 TRACK 8

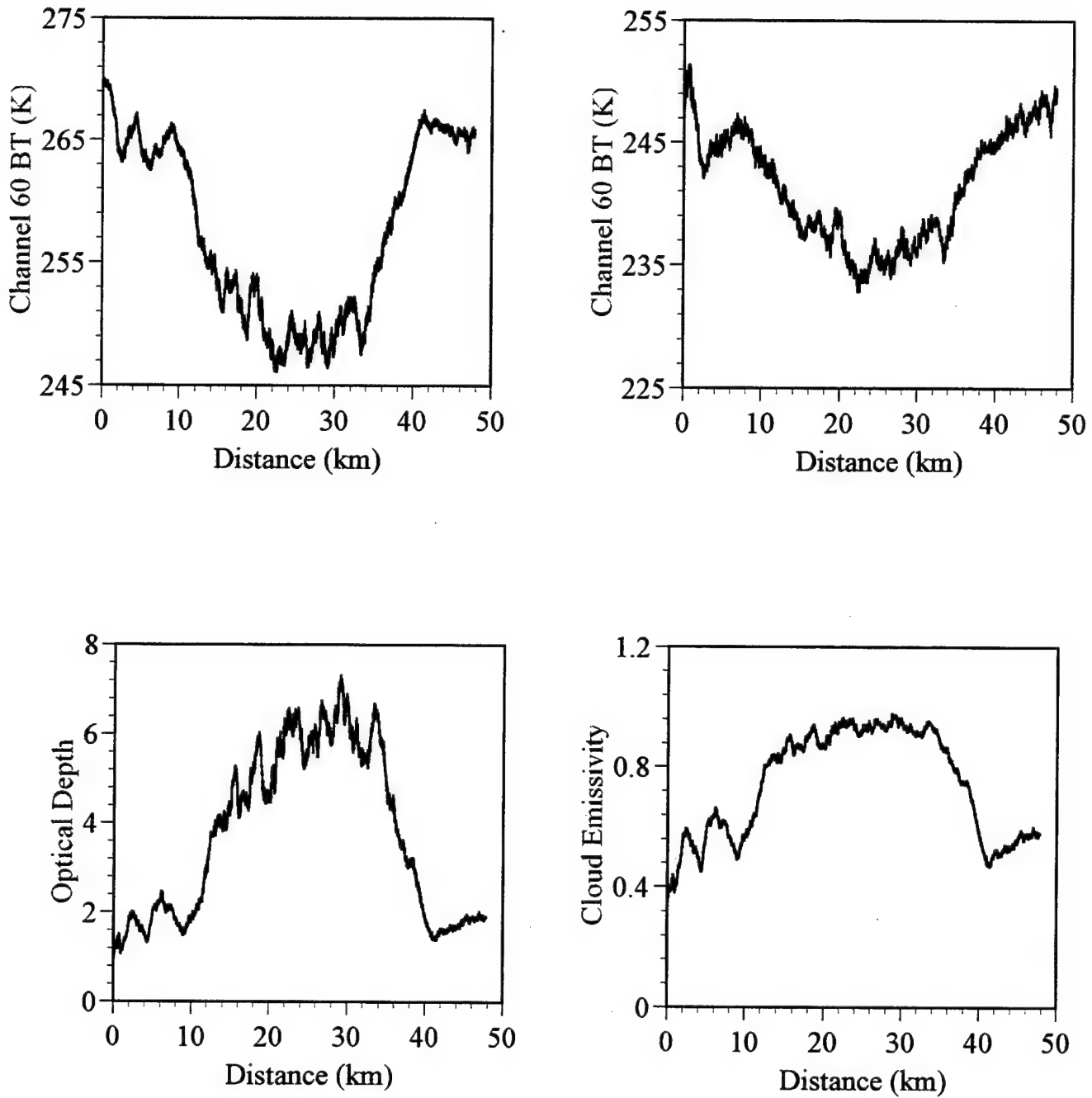


Figure 25 Same as Figure 24 except for Track 8, 9/16/95.

3.2.5 Validation of Retrieval Results

The cirrus clouds on September 16 was also remotely observed by the ground-based 8.6-mm radar which operated continuously during all four flight tracks. Each track passed the radar site once. Moreover, the same area of cirrus clouds were also sampled in-situ by cloud probes on board HARP, which flew simultaneously below ARES in the vicinity of the ground-observation site. Because of the coincidence and collocation of the ARES, radar, and cloud probes operations, we can validate the ARES retrieved cirrus cloud temperatures/heights, optical depths and mean effective sizes using the radar and cloud probe measurements. These validation efforts are described in the following.

To validate the retrieved cirrus cloud temperature/height, we use the time series of cloud boundary (cloud top and base) altitudes derived from the 8.6-mm radar measurement, together with the upper tropospheric temperature measurement by HARP. Figure 26(a) shows the atmospheric temperature profile between 5 and 11 km. These temperature values were obtained between 2029 and 2341 UTC. Within the altitude range, the temperature varies between -5° and -55°C . Figure 26(b) shows the cloud boundary altitudes derived from the 8.6-mm radar measurements between 2000 and 2400 UTC. Within this time period, the 8.6-mm radar observed continuous presence of a single layer of cirrus cloud. Between 2000 and 2100 UTC, the observed cloud top and base were located at 8 and 6 km, respectively. After 2100 UTC, the cloud-top altitude fluctuates between 8 and 10 km, while the cloud base altitudes largely remains at 6 km, except for the period between 2130 and 2230 UTC. We convert the retrieved cloud temperatures into cloud altitudes using the HARP-derived sounding. (There was no surface sounding launched around the flight time of the WB-57F.) For Tracks 1 and 3, when WB-57F flew over the radar site, the area happened to be clear, although the radar recorded very thin cirrus. Thus, comparison of retrieved cloud altitudes with the radar data was not available. For Tracks 5 and 8, the retrieved cloud temperatures over the radar site are -33° and -40°C , which correspond to 8.2 and 9.2 km, respectively. Both altitudes are within the radar-derived cloud boundaries but near the cloud top at the particular WB-57F overpass time.

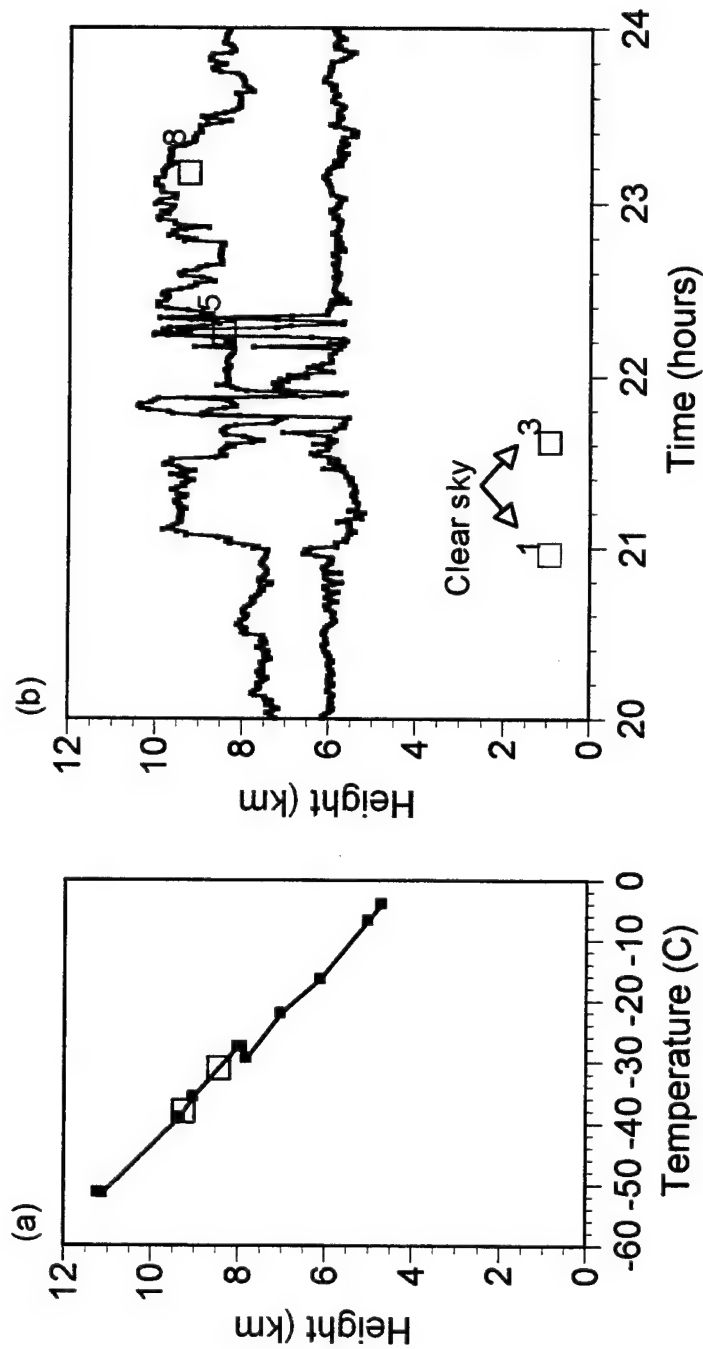


Figure 26 (a) Partial sounding of the middle and upper troposphere obtained using HARP flight above Hanscom AFB (squares correspond to retrieved cloud temperature). (b) Comparison of cloud top heights (obtained from radar/lidar measurements) and retrieved cloud temperatures. Retrieved temperatures are displayed for Tracks 1, 3, 5, and 8 (in chronological order).

To verify the retrieved cirrus cloud optical depths and ice crystal mean effective sizes, we need to use the in-situ ice crystal size distributions obtained by the optical probes on board HARP. Between 2030 and 2040 UTC (case 1), and between 2147 and 2157 UTC (case 2), HARP flew a race track pattern which was within 30 km from Hanscom Air Force Base (Figure 27), and are approximately collocated and coincident with the Tracks 1 and 3 of the ARES flights. For both cases, the flight altitude was at about 8 km, corresponding to the radar-detected cirrus cloud altitude. Ice crystal size distributions sampled by the 2D-C probe on board HARP for both cases have been shown in Figure 6. From scattering and absorption calculations, visible extinction coefficients of 0.54 and 0.57 km^{-1} were obtained for cases 1 and 2, respectively. Moreover, based on the cloud boundary altitudes derived from the 8.6-mm radar measurements, the averaged cirrus cloud thicknesses during the two periods were about 1.75 and 2 km for cases 1 and 2, respectively. Because the vertical profile of the 2D-C median volume ice crystal diameter obtained during the ascending run of HARP indicates that ice crystal sizes vary by no more than $20 \text{ }\mu\text{m}$ between 6.5 and 8 km, it appears reasonable to use the computed extinction coefficients based on single-level aircraft measurements to represent the vertically averaged cirrus cloud extinction coefficients. The computed optical depths based on the preceding approximation are 0.94 and 1.14 for cases 1 and 2, respectively. The mean retrieved optical depths are 0.89 and 1.42 for Tracks 1 and 3 of the ARES flight, respectively. The retrieved mean optical depth for Track 1 agrees relatively well with that from the 2D-C probe. However, for Track 3, the difference between the two optical depths is on the order of 0.3. There are two reasons for such discrepancy. First, estimate of the optical depth from the 2D-C probe is based on the assumed composite ice crystal size distribution at a single flight level within the cirrus cloud. Second, the variation range of the retrieved optical depth for Track 3 is much larger than that for Track 1.

Finally, we use the computed mean effective ice crystal size based on single-level aircraft measurements to represent the vertically averaged cirrus cloud mean effective size and utilize a cirrus cloud model composed of 50% bullet rosettes, 30% hollow columns, and 20% plates. For each shape, a different

HARP Flight Track and Altitude

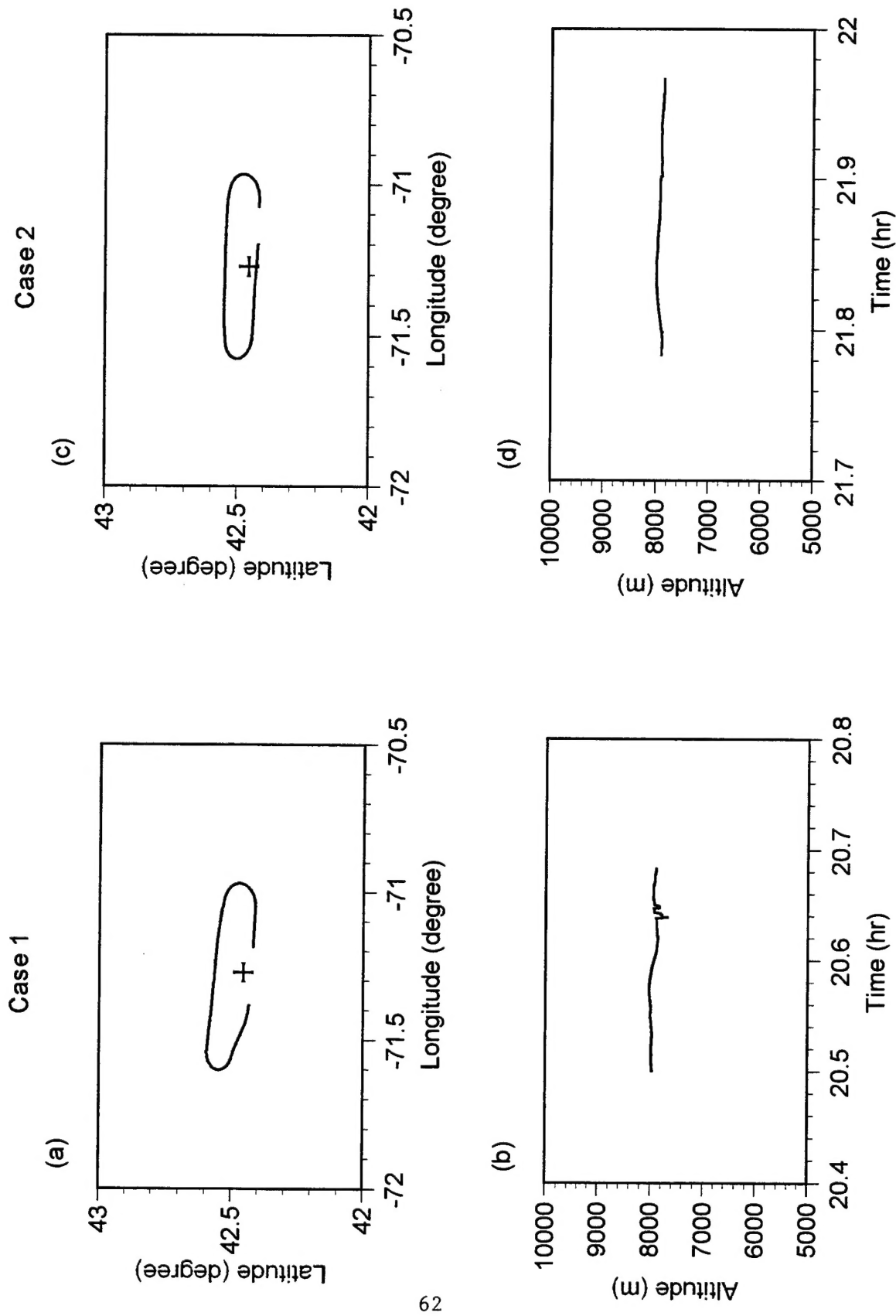


Figure 27 HARP flight track and altitude for cases 1 and 2 on September 16, 1995.

relationship between the maximum dimension (L) and width (W) is employed: for plates, $W = 2.02, L = 0.449$; for hollow columns, $W = 11.3, L = 0.414$ for $L > 200 \mu\text{m}$, $W = 8.479 + 1.002 L / 0.00234$ for $L < 200 \mu\text{m}$; and for bullet rosettes, $W = 2.3103 L / 0.63$. The mean effective sizes for the two size distributions are based on the average of the mean effective size for each shape weighted by the percentage distribution. They are $57.2 \mu\text{m}$ for case 1 and $55.2 \mu\text{m}$ for case 2. The retrieved mean effective sizes are $64.2 \mu\text{m}$ for Track 1 and $53.3 \mu\text{m}$ for Track 3. Both compare reasonably well with the values derived from the 2D-C probe.

4. SUMMARY

The single-scattering properties, including phase function, single-scattering albedo, and extinction coefficient for representative ice crystal size distributions in the spectral range $2\text{--}6.4 \mu\text{m}$ have been calculated using the unified theory for light scattering by ice crystals developed by our research group. We have investigated the range of ice crystal bounding parameters, including the refractive indices for ice in the ARES spectral interval and the ice crystal size and shape for midlatitude cirrus cloud systems. The calculations have been carried out for three representative cirrus cloud ice crystal size distributions corresponding to typical cold, intermediate and warm cirrus clouds in the midlatitudes. We have also investigated the effects of incorporating small ice crystals on the phase function, single-scattering albedo, and extinction coefficient.

Further, we have developed a remote sensing algorithm and the associated computer coding (see Appendix) for the retrieval of cirrus cloud temperature (height), optical depth, and ice crystal size based on the radiative properties of cirrus clouds. The ARES $5.1\text{--}5.3$ and $3.7 \mu\text{m}$ channels were used for this purpose. This scheme has been applied to the ARES data collected on September 16, 1995, over the Hanscom AFB area. The retrieved cloud temperatures compare reasonably well with the collocated and coincident values determined from the ground-based 8.6-mm radar. The retrieved optical depth and mean effective size also match the values determined from in-situ microphysical measurements.

REFERENCES

- Fu, Q., and K. N. Liou, 1993: Parameterization of the radiative properties of cirrus clouds, *J. Atmos. Sci.*, 50, 2008-2025.
- Gayet, J-F., G. Febvre, G. Brogniez, H. Chepfer, W. Renger, and P. Wendling, 1996: Microphysical and optical properties of cirrus and contrails: cloud field study on 13 October 1989, *J. Atmos. Sci.*, 53, 126-138.
- Heymsfield, A. J., and C. M. R. Platt, 1984: A parameterization of the particle size spectrum of ice clouds in terms of the ambient temperature and the ice water content, *J. Atmos. Sci.*, 41, 846-855.
- Heymsfield, A. J., and L. M. Miloshevich, 1993: Homogeneous ice nucleation and supercooled liquid water in orographic wave clouds, *J. Atmos. Sci.*, 50, 2335-2353.
- Heymsfield, A. J., and G. M. McFarquhar, 1996: High albedos of cirrus in the tropical pacific warm pool: microphysical interpretations from CEPEX and from Kwajalein, Marshall Islands, *J. Atmos. Sci.*, 53, 2424-2451.
- Liou, K. N., 1992: Radiative and cloud processes in the atmosphere: Theory, observation, and modeling. Oxford University Press, New York, 487 pp.
- Liou, K. N., and Y. Takano, 1994: Light scattering by nonspherical particles: Remote sensing and climatic implications, *Atmos. Res.*, 31, 271-298.
- Liou, K. N., S. C. Ou, Y. Takano, F. P. J. Valero, and T. P. Ackerman, 1990: Remote sounding of the tropical cirrus cloud temperature and optical depth using 6.5 and 10.5 μm radiometers during STEP, *J. Appl. Meteor.*, 29, 716-726.
- McFarquhar, G. M., and A. J. Heymsfield, 1996: Microphysical characteristics of three cirrus anvils sampled during the Central Equatorial Pacific Experiment (CEPEX), *J. Atmos. Sci.*, 53, 2401-2423.
- Ou, S. C., K. N. Liou, W. M. Gooch, and Y. Takano, 1993: Remote sensing of cirrus cloud parameters using AVHRR 3.7- and 10.9- μm channels, *Appl. Opt.*, 32, 2171-2180.
- Ou, S. C., K. N. Liou, Y. Takano, N.X. Rao, Q. Fu, A.J. Heymsfield, L.M. Miloshevich, B. Baum, and S.A. Kinne, 1995: Remote sounding of cirrus cloud optical depths and ice crystal sizes from AVHRR data: verification using FIRE II IFO Measurements, *J. Atmos. Sci.*, 52, 4143-4158.
- Platt, C. M. R., J. D. Spinhirne, and W. D. Hart, 1989: Optical and microphysical properties of a cold cirrus cloud : evidence for regions of small ice particles, *J. Geophys. Res.*, 94, 11151-11164.
- Rao, N. X., S. C. Ou, and K. N. Liou, 1995: Removal of the solar component in AVHRR 3.7- μm radiances for the retrieval of cirrus cloud parameters, *J. Appl. Meteor.*, 34, 482-499.
- Takano, Y., and K. N. Liou, 1989: Radiative transfer in cirrus clouds, *J. Atmos. Sci.*, 46, 3-36.

- Takano, Y., and K. N. Liou, 1995: Radiative transfer in cirrus clouds. III: Light scattering by irregular ice crystals, *J. Atmos. Sci.*, 52, 818-837.
- Yang, P., and K. N. Liou, 1995: Light scattering by hexagonal ice crystals: comparison of finite-difference time domain and geometric optics models, *J. Opt. Soc. Am. A.*, 12, 162-176.
- Yang, P., and K. N. Liou, 1996a: A geometric-optics/integral-equation method for light scattering by nonspherical ice crystals, *Appl. Opt.*, 35, 6568-6584.
- Yang, P., and K. N. Liou, 1996b: Finite-difference time domain method for light scattering by small ice crystals in three-dimensional space, *J. Opt. Soc. Am. A.*, 13, 2072-2085.